Universidade de Aveiro
2023

João Ferreira Alves Pereira

Numerical study of fatigue crack growth in metallic materials

Estudo numérico da propagação de fendas por fadiga em materiais metálicos

Universidade de Aveiro
2023

João Ferreira Alves Pereira

Numerical study of fatigue crack growth in metallic materials

Estudo numérico da propagação de fendas por fadiga em materiais metálicos

Dissertação apresentada à Universidade de Aveiro para cumprimento dos requisitos necessários à obtenção do grau de Mestre em Engenharia Mecânica, realizada sob orientação científica do Doutor Pedro André Dias Prates, Professor Auxiliar do Departamento de Engenharia Mecânica da Universidade de Aveiro.

This work was supported by projects UIDB/00481/2020, UIDP/00481/2020, LA/P/0104/2020 and 2022.05783.PTDC - Portuguese Foundation for Science and Technology (FCT); and CENTRO-01-0145 FEDER-022083 - Regional Operational Programme of Centro (Centro2020), trough Portugal 2020 and the European Regional Development Fund.

O júri / The jury

Presidente / President

Prof. Doutor Joaquim Alexandre Mendes de Pinho da Cruz
Professor Auxiliar da Universidade de Aveiro

Vogais / Committee

Prof. Doutor Fernando Jorge Ventura Antunes
Professor Associado Com Agregação da *Universidade de Coimbra - Faculdade de Ciências e Tecnologia*

Prof. Doutor Pedro André Dias Prates
Professor Auxiliar da Universidade de Aveiro

Acknowledgements

Firstly, I would like to thank my advisor, Professor Pedro Prates, for his availability and support throughout this work. Without his encouragement and guidance, the completion of this work would not have been possible.

I also express my deep gratitude to my family for all the support during this journey, especially to my brother for the advice of someone who has recently gone through the same experience.

Lastly, from the bottom of my heart, I thank the friends that Aveiro brought into my life, who have always stood by my side through good and bad times. I conclude my academic journey not only with the title of Master in Mechanical Engineering but also with friendships for life.

The best is yet to come.

Keywords Fatigue Crack Growth, Crack Closure, Open Load, Aluminium Alloy, Plastic Crack Tip Opening Displacement (CTODp), Numerical Simulation

Abstract Fatigue is the most common failure mode in mechanical components when they are subjected to cyclic loads during their service life. This phenomenon can lead to unexpected and catastrophic failures, even in components that appear to be in good condition. In the context of crack propagation analysis, the relationship between fatigue crack growth rate and the range of the stress intensity factor ($\mathrm{d}a/\mathrm{d}N$–ΔK) is frequently used. However, this approach has limitations regarding the parameter ΔK, as it only quantifies the elastic component at the crack tip. Considering this limitation and since crack propagation is associated with nonlinear and irreversible phenomena at the crack tip, a parameter capable of quantifying the level of plastic deformation, called CTOD (Crack Tip Opening Displacement), was used.
In this dissertation, the objective is to study the fatigue crack growth (FCG) in CT specimens using a numerical simulation software based on finite element analysis (Abaqus). Firstly, the study focused on the aluminium alloy AA2024-T351, where the influence of parameters such as specimen's thickness and size of finite elements in the plane and along the crack front on CTOD and Popen were analysed. Two-dimensional specimens were also created considering plane stress and plane strain states, which were used for comparison with three-dimensional models. Additionally, a comparison of the plastically deformed zones and the crack profile was made among some of the numerical models. Subsequently, a study was conducted on a titanium alloy, aiming to compare the plastic component of ΔCTOD with results obtained from previously conducted experimental tests. It was found that the element size in the plane has some influence on CTOD, especially at the surface, and in P_{open} as it approaches the mid-thickness of the models. In turn, the element size in thickness only influences the P_{open} results for zones near the mid-thickness, possibly due to a lower mesh refinement in that area. Another parameter to consider is the thickness of the models, which has shown significant influence on the P_{open} curves. Regarding case study 2, it was observed that the number of load/unload cycles per propagation greatly influences the results of both CTOD and plastic ΔCTOD, and the discrepancy with respect to the provided experimental results may be due to the assumption of a constant crack propagation rate in the numerical simulations, which is not observed experimentally.

Palavras-chave

Propagação de Fendas por Fadiga, Fecho de Fenda, Força de Abertura de Fenda, Liga de Alumínio, Deslocamento Plástico da Abertura de Frente de Fenda (CTODp), Simulação Numérica

Resumo

A fadiga é o modo de falha mais comum em componentes mecânicos quando estes são submetidos a cargas cíclicas durante o seu tempo de serviço. Este fenómeno pode levar a falhas inesperadas e catastróficas, mesmo em componentes que parecem estar em boas condições. No âmbito da análise de propagação de fendas, é utilizada, recorrentemente, a relação entre a velocidade de propagação de fendas por fadiga e a gama do fator de intensidade de tensões ($\mathrm{d}a/\mathrm{d}N$–ΔK), no entanto esta abordagem apresenta limitações quanto ao parâmetro ΔK uma vez que este apenas quantifica a solicitação elástica na extremidade de fenda. Tendo em conta esta limitação, e uma vez que a propagação de fendas está associada a fenómenos não lineares e irreversíveis na extremidade da fenda, utilizou-se um parâmetro que fosse capaz de quantificar o nível de deformação plástica, denominado CTOD (deslocamento de abertura de extremidade de fenda).

Na presente dissertação pretende-se estudar a propagação de fendas por fadiga (PFF) em provetes CT, recorrendo a um software de simulação numérica de elementos finitos (Abaqus). Primeiramente debruçou-se o estudo na liga de alumínio AA2024-T351, onde se analisou a influência de alguns parâmetros como a espessura do provete e o tamanho dos elementos finitos no plano e ao longo da frente de fenda, no CTOD e P_{open}. Foram ainda criados provetes bidimensionais nos quais se considerou estado plano de tensão e estado plano de deformação, que também serviram para comparar com os modelos tridimensionais. Para além do referido, realizou-se uma comparação das zonas deformadas plasticamente e do perfil da fenda entre alguns dos modelos numéricos. De seguida procedeu-se ao estudo de uma liga de titânio para a qual se pretendia comparar a variação da componente plástica do CTOD com os resultados fornecidos provenientes de ensaios experimentais previamente realizados. Verificou-se que o tamanho de elemento no plano tem alguma influência no CTOD principalmente à superfície, e em P_{open} à medida que se aproxima da meia espessura dos modelos. Por sua vez, o tamanho de elemento em espessura tem apenas influência nos resultados de P_{open} para zonas perto da meia espessura, podendo ser causado por um menor refinamento da malha nessa zona. Outro parâmetro a ter em conta é a espessura dos modelos que demonstrou ter grande influência nas curvas de P_{open}. Relativamente ao caso de estudo 2, verificou-se que o número de ciclos de carga/descarga por propagação influencia muito os resultados tanto de CTOD como de ΔCTOD plástico e a discrepância relativamente aos resultados experimentais fornecidos poderá dever-se à consideração de uma velocidade de propagação da fenda constante nas simulações numéricas, o que experimentalmente não se verifica.

Contents

List of Tables

Intentionally blank page.

List of Figures

Intentionally blank page.

List of Symbols and Acronyms

List of Symbols

A – set of Voce and Armstrong & Frederick parameters that minimises $F(A)$
a – Crack length
a_0 – Initial crack length
B - Specimen thickness
c, m – Constants of the Paris-Erdogan law
C, n – Material parameters of the Voce isotropic law
C_X – Parameter of the Armstrong & Frederick kinematic law
C_Y – Parameter of the Voce isotropic law
$\mathrm{d}a/\mathrm{d}N$ - Fatigue crack growth rate
E – Young's modulus
f - Function defining the yielding condition
$F(A)$ – Cost function
G– Geometric parameter
K - Stress intensity factor
K_{IC} - Fracture toughness
K_{eff} – Effective stress intensity factor
K_{max} – Maximum stress intensity factor
K_{min} – Minimum stress intensity factor
K_{open} – K value where the crack opens
M - Number of experimental points
N - Number of cycles
P_{max} - Maximum load in a loading cycle
P_{min} - Minimum load in a loading cycle
$\mathrm{P}_{\mathrm{open}}$ - Crack opening load
R – Stress ratio
r_{pc} – Radius of inverse plastic zone
X – Deviatoric back-stress tensor
X_{Sat} - Kinematic saturation stress
Y_0 - Yield stress
Y_{Sat} - Isotropic saturation stress
W - Specimen width
Δa – Crack advance
$\Delta\mathrm{CTOD}$ - Crack tip opening displacement range
$\Delta\mathrm{CTOD}_{\mathrm{p}}$ - Plastic crack tip opening displacement range
ΔK - Stress intensity factor range
ΔK_{eff} - Effective stress intensity factor range

ΔK_{th} – Fatigue threshold
$\Delta\varepsilon_p$ - Accumulated plastic strain
$\Delta\epsilon_{\text{p},yy}$ - Plastic deformation range along y direction
$\bar{\varepsilon}^p$ - Equivalent plastic strain
$\dot{\bar{\varepsilon}}^p$ - Equivalent plastic strain rate
$\sigma^{\text{Exp}}(A)$ - Experimentally measured values of true stress
$\sigma^{\text{Fit}}(A)$ - Fitted measured values of true stress
σ' - Deviatoric Cauchy stress tensor
$\bar{\sigma}$- Equivalent stress σ – Nominal stress
σ_{max} – Maximum stress
σ_{min} – Minimum stress
σ_{z} - Z direction stress component
σ_0 – Yield stress
ν - Poisson's ratio

Acronyms

2D - Two-Dimensional
3D - Three-Dimensional
AA – Aluminum Association
ASTM – American Society for Testing and Materials
BC - Boundary Conditions
CJP – Christopher James Patterson (model)
CT - Compact Tension
CTL - Crack Tip Location
CTOD - Crack Tip Opening Displacement
DIC – Digital Image Correlation
DP - Plane Strain State
FCG – Fatigue Crack Growth
FE – Finite element
FEM - Finite Element Method
GRG2 – Generalised Reduced Gradient
LEFM – Linear Elastic Fracture Mechanics
OICC - Oxide Induced Crack Closure
PICC – Plasticity Induced Crack Closure
PEEQ - Equivalent Plastic Strain
RICC - Roughness Induced Crack Closure
TP - Plane Stress State
TPS - Total Plastic Strain

Part I

Introduction

Chapter 1

Introduction

1.1 Framework

The prediction of unstable fracture or the growth of pre-existing cracks is the most fundamental issue in fracture mechanics. Dynamic loads are the most common in machine elements and can induce fatigue failure when applied to a component. Fatigue is a failure mode responsible for 80% to 90% of failures in service parts subjected to cyclic loads [1]. This complex physical phenomenon is affected by several factors, such as the component's geometry, the intensity, type, and duration of dynamic loads, the material properties, and the environmental conditions (humidity, temperature, corrosive environment). The integrity of mechanical structures can be verified through the control of crack propagation. In this way, by using computational finite element models, it is possible to predict the service life of components and preserve the safety of structures, thus ensuring human protection. So, the accurate prediction of fatigue crack growth (FCG) is indispensable for making the right operation/repair/replacement of machine components decisions and to draw up reliable inspection plans, to avoid the occurrence of failures and equipment malfunction. Most engineering problems can be solved using numerical simulation software. These provide approximate solutions to complex problems, with less execution time and component inspection, and also reduced costs compared to conventional methods like hand calculations, analytical solutions and experimental testing.

Fatigue properties are obtained usually resorting to standardized specimens. Nevertheless, the determination of parameters such as the stress intensity factor and the plastic Crack Tip Opening Displacement (CTOD) through an analytical path presents great difficulties, making it advantageous to use this type of software. Simulation with 2D models has been more recurrent in fatigue crack propagation studies in metallic specimens, in which simplifications such as plane stress state or plane strain state are considered. 2D models are computationally less demanding than 3D models and are beneficial when the out-of-plane behaviour is negligible. However, the two-dimensional models have limitations in the fracture mechanics and fatigue studies because they are unable to analyse what happens along the crack front. For that reason, 2D models cannot take into account different crack front shapes or study the influence of the thickness of the specimen in the numerical analysis. In this way, three-dimensional studies are considered more realistic and accurate than two-dimensional studies, as they allow a more rigorous analysis of aspects such as the effects of specimen thickness on crack

growth.

All structural and machine elements subjected to cyclic loads should be designed considering the material's service life [2]. The service life is often determined through da/dN–ΔK curves, where da/dN and ΔK respectively represent the crack propagation rate and the range of stress intensity factor. However, the use of stress intensity factor has some limitations in predicting the behaviour of FCG (Fatigue Crack Growth) as it is unable to quantify the plastic deformation occurring at the crack tip. Therefore, an alternative has emerged to use nonlinear parameters such as Crack Tip Opening Displacement (CTOD), based on the assumptions that crack propagation is closely related to plastic deformation at its tip and that this deformation can be quantified by CTOD.

The present proposal aims to study numerically the FCG in metallic materials based on the results of finite element simulation of mechanical tests on standardized specimens. In the first stage, a 2D numerical analysis of fatigue crack propagation is planned (under plane strain and plane stress conditions). Subsequently, the development of 3D numerical models is expected, taking into account different thickness values with a variable number of elements along the crack front.

1.2 Objectives

The main objective of this work is the numerical study of fatigue crack growth in metallic materials, more specifically on AA2024-T351 aluminium alloy. Specific objectives include:

- Numerical modeling and simulation of crack propagation in a CT (compact tension) specimen, initially in 2D and later through 3D numerical models;
- Study of the relationship between CTOD (Crack Tip Opening Displacement) and the crack propagation rate (da/dN);
- Study of the influence of the in-plane element size, the crack front element size and the model's thickness on the CTOD and P_{open} (crack opening load);
- Comparison of the plastic zones and crack profile between 2D and 3D models.

Another objective of this work is the numerical modelling and simulation of a crack propagation in a new CT specimen for a titanium alloy (2D and 3D models), for which it is intended to determine the plastic crack tip opening displacement range (plastic ΔCTOD) along the crack and then compare the values obtained from the experimental results.

1.3 Layout of the dissertation

This dissertation is divided into five chapters. The numbering and presentation of each chapter are performed as follows:

- Chapter 1, Introduction: introduction to the subject under study with presentation of the framework, objectives and the structure of the thesis;

- Chapter 2, Literature review: description of the main concepts of fatigue theory, as well as the fundamentals of the finite element method and a brief summary of the most relevant studies to this work;
- Chapter 3, Case studies: description of the different case studies, the finite element software (Abaqus) and the methodology to be followed for creating the numerical models. Some notions of plasticity theory and hardening laws are presented. Information regarding the geometry and material of the specimens, as well as applied loads, among other aspects, and finally a summary of all the simulations carried out is presented;
- Chapter 4, Results and Discussion: presentation and analysis of the obtained results, namely CTOD and crack opening load graphs, plastically deformed zones, crack profiles, etc;
- Chapter 5, Conclusions and Recommendations for future research: the main conclusions obtained in this work are presented and some proposals are suggested for future works.

Intentionally blank page.

Part II

Materials and methods

Chapter 2

Literature Review

2.1 Fatigue phenomenon

Fatigue is a type of failure that occurs in parts that are repeatedly subjected to cyclic loads. This type of failure is responsible for a large percentage (between 80% and 90%) of all failures in service parts [1]. It is very important for engineers to study fatigue in order to develop better products. According to ASTM [3], fatigue is a process in which a material experiences gradual and localized plastic deformation (changes in shape) when it is exposed to cyclic stresses and strains at regions where there is a high stress concentration. This can eventually lead to the formation of cracks or complete fracture if the material experiences enough stress and strain cycles.

The fatigue process (Figure 2.1) can be divided into three main phases: crack initiation, crack propagation, and final fracture. Under uniaxial loads (where the load is applied in one direction), crack initiation often occurs at the surface of the part or at regions of high stress concentration, such as notches. The crack starts to form and grow microscopically when there are slip lines with a high density of dislocations that are oriented at a 45-degree angle to the loading direction. Slow crack growth occurs due to the presence of microstructural barriers. The crack then begins to propagate when sliding planes are created next to the crack tip, causing displacement in a direction normal to the applied load. The crack growth rate increases gradually while the loading is maintained. Finally, fracture occurs when the crack becomes unstable and propagates rapidly until the remaining material can no longer withstand the stresses or strains, causing sudden fracture [4].

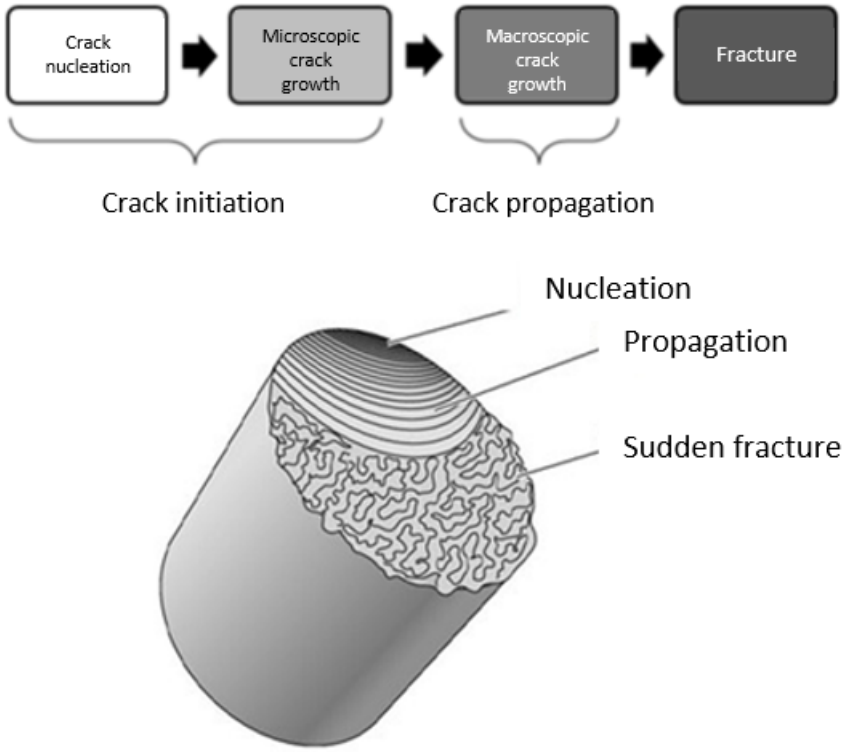

Figure 2.1: Stages of fatigue failure. (Adapted from [5])

2.2 LEFM concepts

In 1958, Irwin [6] started studying Linear Elastic Fracture Mechanics (LEFM) with the purpose of describing the fracture behaviour. Although the use of LEFM to fatigue crack propagation is well established, it is assumed that the material is homogeneous, isotropic and behaves linearly elastic, i.e., the plastic deformation is neglected and the damage at the crack tip is assumed to be controlled by the elastic field [7, 8]. Irwin showed that all components have cracks and that the stress at the front of each crack can be quantified by the stress intensity factor (K), which is supposed to control the fatigue crack growth (FCG). The Equation 2.1 for the stress intensity factor depends on the applied nominal stress (σ), the crack deformation, the crack length (a), and the component's geometry factor, G.

$$K = G\sigma\sqrt{\pi a} \tag{2.1}$$

In cyclic loading, the stress intensity range, ΔK, is given by Equation 2.2:

$$\Delta K = K_{\max} - K_{\min}, \tag{2.2}$$

where $K_{\max}$ and $K_{\min}$ are the maximum and minimum stress intensity factors, respectively.

The crack growth rate under constant amplitude cyclic loading conditions can be characterised by the relation between the crack length a, and the number of cycles N. The slope of the resulting curve is the value of the fatigue propagation rate $\mathrm{d}a/\mathrm{d}N$, which represents the change in the length of the fatigue crack per load cycle [8].

Figure 2.2 shows a typical fatigue crack growth rate curve, i.e. $\mathrm{d}a/\mathrm{d}N$-ΔK curves on a bi- logarithmic scale, where three distinct regimes stand out. Regime I also denominated "Threshold region", represents the region where FCG tends to zero for the fatigue threshold ΔK_{th}. In other words, there is no crack propagation for values of stress intensity factor below that threshold. ΔK_{th} can be determined experimentally from a load-shedding procedure, where ΔK is gradually reduced until the crack growth rate reaches a very small value [9]. Regime II or Paris regime corresponds to a region where there is a linear relation between $\mathrm{d}a/\mathrm{d}N$ and ΔK, in logarithmic scales, described by Paris and Erdogan law (Equation 2.3).

$$\frac{da}{dN} = c(\Delta K)^m \tag{2.3}$$

where $\mathrm{d}a/\mathrm{d}N$ is the crack growth per cycle, ΔK is the stress intensity factor range, and c and m are material constants obtained experimentally. These constants are dependent of factors like the material, stress ratio and environmental conditions [10]. During this regime the crack propagates steadily. Lastly, Regime III or high-growth rate regime consists of an unstable crack propagation zone. When the maximum stress intensity factor value K_{max} approaches the value of fracture toughness of the material K_{IC}, there is a sudden increase in FCG rate until the final fracture. This regime does not always happen, as it is the case of materials with high ductility [4]. The mean stress, microstructure and thickness have large influence in this regime while environment has little [11]. The mean stress, which is represented as the relation between minimum and maximum stress (Equation 2.4), has a large influence in this regime (Regime III) as well as the microstructure and thickness [11]. In general, increasing R will increase the fatigue crack growth rate [12].

$$R = \frac{\sigma_{\mathrm{min}}}{\sigma_{\mathrm{max}}} = \frac{K_{\mathrm{min}}}{K_{\mathrm{max}}} \tag{2.4}$$

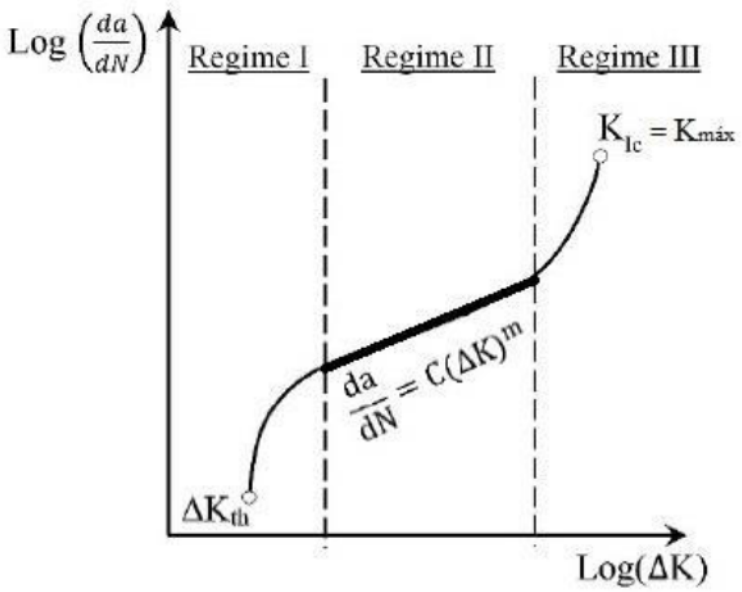

Figure 2.2: da/dN versus ΔK curve on log-log scale.

2.3 Issues regarding LEFM

As mentioned before, ΔK is the parameter that controls FCG at the crack tip in LEFM theory and its use has some advantages, such as the ease in obtaining K numerically and the existence of many viable solutions in the literature for different cracked geometries configurations. For this reason, the LEFM approach has been widely used in structural design and in components subjected to cyclic loads, where it is assumed that the crack tip damage is controlled by the elastic stress field [7]. However, linear elastic fracture mechanics is valid only as long as nonlinear material deformation is confined to a small region surrounding the crack tip, and FCG is related to nonlinear and irreversible phenomena at the crack tip, like the plastic deformation. In many materials, it is virtually impossible to characterize the fracture behaviour with this approach, and an alternative is required [9].

Despite its usefulness, LEFM has faced numerous criticisms. For instance, it fails to account for the impact of stress ratio and load history on da/dN-ΔK relations, exhibits peculiar behaviour when dealing with short cracks [13], and suffers from dimensional issues as evidenced by equation 2.3 where the units of $(\Delta K)^m$ and da/dN are [MPa$\sqrt{m}$] and [m/cycle], respectively, which causes constant C to have units of [$\sqrt{m}$/MPa $\cdot$ cycle], so that the equation can be coherent [14].

2.4 Some proposed solutions

Over time, several theories have been developed to address the limitations that arise from applying the LEFM theory to the fatigue crack propagation. Among these theories, the crack closure phenomenon is one of the most well-known. The importance of this phenomenon was first demonstrated by Elber [15] when he observed that a fatigue crack could be closed even in a tensile load. The author concluded that if the stresses

are lower than a crack opening stress, the crack might not propagate. Therefore, the crack closure phenomenon consists in the physical contact of the crack flanks within a certain stress range where no propagation is expected to occur. In this case, it is assumed that only the portion of the load cycle during which the crack is open contributes to its propagation [16], resulting in the effective stress intensity factor range, ΔK_{eff}, which value can be obtained by Equation 2.5.

$$\Delta K_{\text{eff}} = K_{\max} - K_{\text{open}}, \tag{2.5}$$

where K_{open} is the stress intensity factor below which the crack remains closed. Figure 2.3 represents the effective stress intensity factor range and the relevant stress intensity factors. The K_{open} value can be obtained either experimentally or numerically, but there isn't any precise methodology for it.

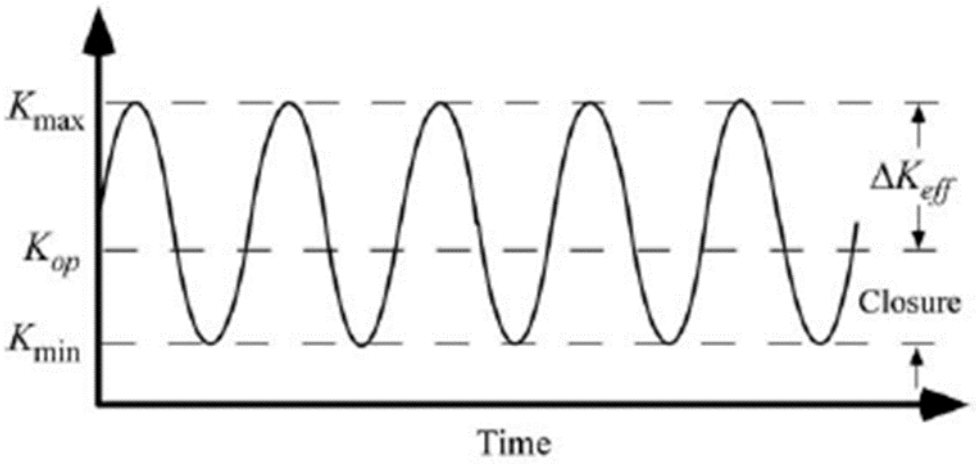

Figure 2.3: Schematic representation of the effective stress intensity factor range, ΔK_{eff} (from [9])

Regarding $\mathrm{d}a/\mathrm{d}N$-ΔK curves, in the Paris equation, ΔK should be replaced by ΔK_{eff}, as shown in Equation 2.6:

$$\frac{da}{dN} = c(\Delta K_{\text{eff}})^m \tag{2.6}$$

After Elber's initial research, several other researchers have validated the occurrence of crack closure during fatigue crack propagation. Five mechanisms of fatigue crack closure were identified by Suresh and Ritchie [17] and are shown in Figure 2.4.

Plasticity-induced crack closure (PICC), Figure 2.4(a), results from residual stresses in the plastic wake. Many investigators have studied PICC, and the conclusions were similar. For example, Budiansky and Hutchinson [18] showed that the residual stretch in the plastic wake causes the crack faces to close at a positive remote stress when applying the Dugdale-Barenblatt strip-yield model to this problem. Some authors performed studies about the effect of the stress state on PICC. For instance, Zhao et al. [19] modelled a CT specimen under both plane strain and plane stress assumptions and observed

high levels of PICC under plane stress, during crack growth under cyclic tension, while no closure was obtained under plane strain state. Roughness-induced crack closure (RICC), which is illustrated in Figure 2.4(b), is influenced by the microstructure. Crack deflections due to microstructural heterogeneity can lead to mixed mode conditions on the microscopic level. Mode II displacements can cause mismatch between upper and lower crack faces, which results in contact of crack faces at a positive load [9]. Oxide-induced crack closure (OICC), Figure 2.4(c), is normally associated with an aggressive environment. Crack closure can also be provoked by a viscous fluid, as shown in Figure 2.4(d). Alike the oxide mechanism, the fluid acts as a wedge between crack faces. A stress-induced martensitic transformation at the tip of the growing crack can result in a process zone wake, as Figure 2.4(e) illustrates [9]. Despite the crack closure concept being helpful in understanding how variables such as load history and microstructure affect FCG rate, it brought new issues and remains not consensual in the scientific community. With that in mind, some researchers proposed new extra parameters such as the T-stress, which quantifies the effect of specimen's geometry on crack closure [20]. The Christopher-James-Patterson crack tip field model (CJP model) describes the stress field around the crack tip using four different parameters was also proposed [2]. The methodologies mentioned earlier rely on ΔK, therefore there continue to be limitations when it comes to analyse what occurs at the crack tip. To address this issue, nonlinear parameters have been suggested as a replacement for ΔK.

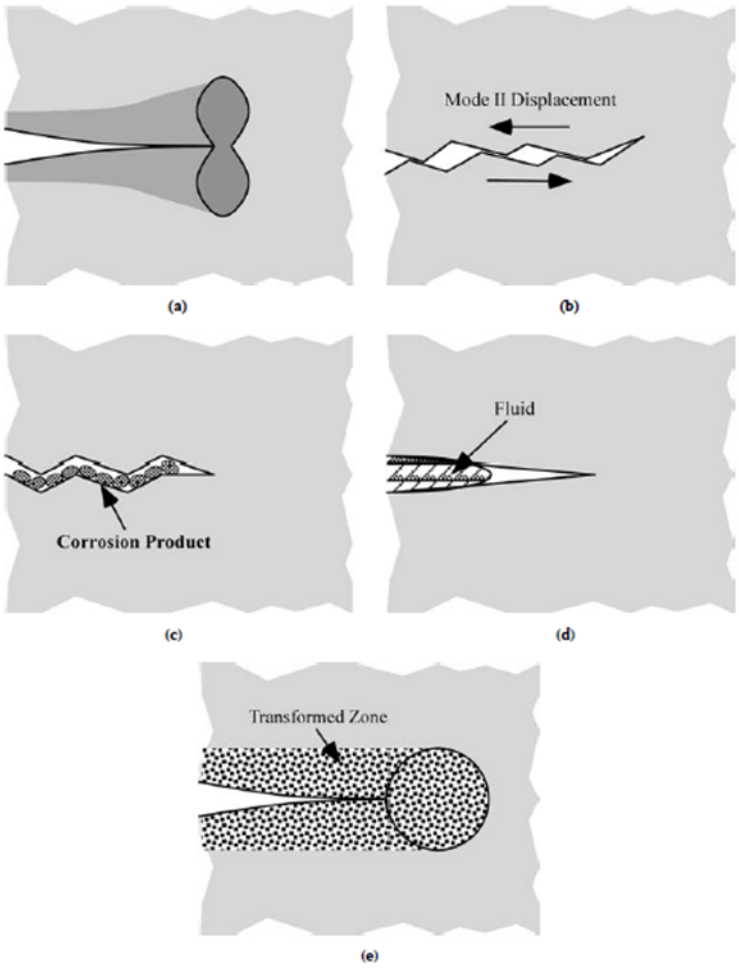

Figure 2.4: Fatigue crack closure mechanisms in metals: (a) plasticity-induced closure; (b) roughness-induced closure; (c) oxide-induced closure; (d) closure induced by a viscous fluid; (e) transformation-induced closure (from [17])

.

2.5 Elasto-plastic fracture mechanics

Elastic-plastic fracture mechanics is applied to materials that exhibit time-independent, nonlinear behaviour (i.e. plastic deformation) [9].

Under cyclic loading, considering tensile loading (Mode I), it is possible to identify three distinct regions at the crack tip [21]. These regions are represented in Figure 2.5 and can be characterized as follows:

- Region I: Cyclic plastic zone where a hysteresis loop occurs, whose shape depends on the stress ratio and ΔK value. The most relevant non-linear parameters at the crack tip are the plastic deformation range $\Delta\epsilon_{\mathrm{p},yy}$, the inverse plastic zone radius (r_{pc}), the total plastic dissipation by cycle and the crack tip opening displacement (CTOD);
- Region II: Monotonous plastic zone in which plastic deformation is reached during

loading and after that an elastic charge-discharge occurs;

- Region III: Elastic zone located at the most distant zone of the crack tip where there is only elastic deformation. This means that the material recovers its original shape when the applied load is removed.

The size of the plastic zone is dependent on the stress level at the crack tip. Additionally, the stress state of the material also affects the size of the plastic zone. In plane stress, the plastic zone is larger than in a plane strain state. The reason for this is that in plane stress conditions, the z direction stress component, σ_z, is zero, while in plane strain conditions it is positive (traction), which restricts the plastic flow [4].

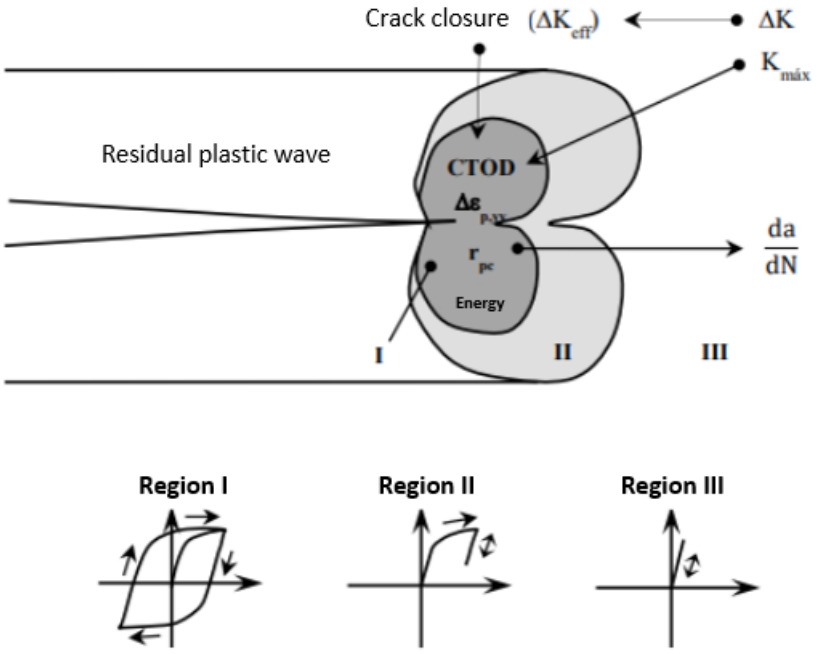

Figure 2.5: Diagram of the crack tip zones, parameters and stress-strain curves (Adapted from [22])

.

2.5.1 Crack Tip Opening Displacement, CTOD

In 1961, Wells proposed the concept of CTOD to characterize the fracture behaviour of ductile materials after trying to measure the fracture toughness value in several structural steels and verifying that these materials were too ductile to be characterized by LEFM [23]. Wells observed in test specimens that before fracture, plastic deformation caused the crack tip to round, and that the rounding degree increased proportionally with the tenacity of the material. The CTOD consists in the physical distance between the two surfaces of a fatigue crack near the crack tip. CTOD measurements can be obtained by two procedures, as shown in Figure 2.6. The first is the displacement normal to the crack plane relative to the original position of the crack tip. The second

measures the displacement at the intersection of a 90^{o} vertex with the crack faces and was proposed by Rice [24]. When referring to measures relatively distant from the crack tip, the term COD (Crack Opening Displacement) is used instead.

The determination of the CTOD can be done experimentally or numerically. The most relevant experimental technique is the Digital Image Correlation (DIC). DIC is an optical full-field measurement technique that allows 2D strain fields measurements in a specimen. However, it cannot differentiate between elastic and plastic strain components. DIC has gained popularity in analysing strain fields near the crack tip [25], as it has allowed to extract fracture mechanics information like closure stresses [26, 27], plastic zone sizes [28], crack opening displacements (COD) and effective stress intensity factors at the crack-tip, K_{eff} [28–31]. However, the experimental CTOD determination requires caution, as a wrong estimate can lead to unstable propagation and consequent failure of structures or components. On the other hand, an underestimation leads to an excessive limitation of the defects size, leading to unnecessary maintenance services [10]. To overcome this problem, it is recommended that the CTOD measurement is performed numerically through numerical simulation, using the finite element method, rather than experimentally. Furthermore, this parameter is obtained on the first node behind the crack tip.

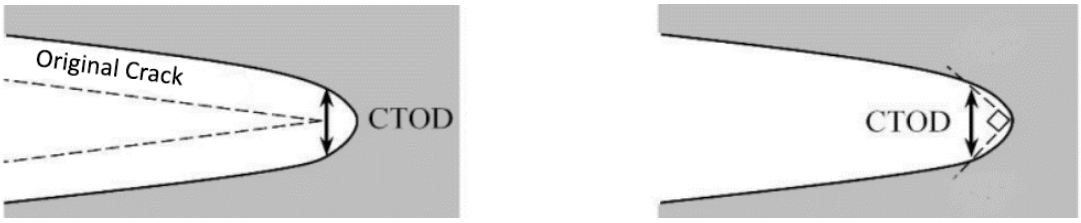

(a) (b)

Figure 2.6: Definitions of CTOD: (a) CTOD equal to the displacement normal to the plane of the crack relative to the position of the tip; (b) CTOD equal to the displacement at the intersection of a 90^{o} vertex with the faces of the crack (from [14])

.

2.6 Work already done based on CTOD

Many studies of crack propagation due to fatigue have recently been developed where the plastic crack tip opening displacement range ($\Delta CTOD_p$) replaces the stress intensity factor range (ΔK). With this kind of approach, it is assumed that fatigue crack propagation is related to nonlinear and irreversible phenomena at the crack tip, like the plastic deformation, and the $\Delta CTOD_p$ is capable of quantifying the plastic deformation level. Most of those studies based on CTOD were developed by research groups and the most relevant for this work are referred below:

- Effect of elasto-plastic properties on fatigue crack growth [4, 32];
- Analysis of the fatigue crack propagation in the stainless steel 304L based on CTOD [10];

- Fatigue crack growth in bi-materials, the AA6082-T6 alloy and the AA7050-T6 alloy [14];
- Study of fatigue crack propagation in aluminum alloy 7050 and 2050–T8 [33];
- Study of the crack propagation in aluminum alloy 6082–T6 [34];
- Study of the effect of numerical model parameters on the predicted value for plastic CTOD [35];
- Fatigue crack propagation analysis in 2024-T351 aluminium alloy using nonlinear parameters [36].

Although there are many different numerical studies related to the use of CTOD as shown above, most of these are applied either to bi-dimensional finite element models, considering plane stress or plane strain, or to very small thickness specimen models (with one finite element along the thickness) in which what happens along the crack front isn't taken into account. Three-dimensional studies are considered more realistic and accurate than two-dimensional studies, as they allow a more rigorous analysis of aspects such as the effects of specimen thickness and crack shape on crack propagation.

With that in mind some researchers performed three-dimensional analyses based on the CTOD as well, and the most relevant are:

- Numerical modelling of fatigue crack closure and its implication on crack front curvature using $\Delta CTOD_p$ [37];
- Crack shapes and crack driving force distributions for naturally growing fatigue cracks [38];
- A methodology for simulating plasticity induced crack closure and crack shape evolution based on elastic–plastic fracture parameters [39];
- A numerical analysis of CTOD in constant amplitude fatigue crack growth [40].

Some of the aforementioned approaches are summarized in Table 2.1, where the most relevant parameters of the numerical models used by each author are identified.

Table 2.1: Summary of numerical parameters of 3D finite element models for FCG analysis.

	Branco et al. [41]	**Camas et al. [8, 42]**	**Guardin et al. [43, 44]**	**Hou [45]**	**Escalero et al. [39]**	**Oplt et al. [37]**	**Antunes et al. [40]**	**Present Study**
Geometry	MT specimen	CT specimen	CT specimen	MT specimen	CT specimen	CT specimen	MT specimen	CT specimen
Kmax [MPa$\sqrt{m}$]	6.97	25	13.33	16.76	11.94	15	[2.01, 20.80]	16.82
Material	AA6016-T4	AA2024-T351	304L steel	Not specified	S275 steel	EA4T steel	AA6016 -T4 AA6082 -T6	AA2024-T351 Titanium Grade 2
FE integration scheme	Selective reduced	Not defined	Selective reduced	Not defined	Selective reduced	Selective reduced	Selective reduced	Selective reduced
In plane elements size µm	8	15.1 41.2	50 100	20	8.56	19.2	8	8 16
Number of elements in half thickness	5 B/2 = 0.5 mm	30; 40 B/2 = 1.5 mm	20 B/2 = 5 mm	25 B/2 = 1 mm	25 B/2 = 1.2 mm	20 B/2 = 5 mm	1 B/2 = 0.1 mm	[1 to 60] B/2 = [0.05 to 3] mm
Contact: Maximum penetration	Not defined	5e-5 mm	Not defined	Closure isn't detected through contact	5e-5 mm	Penetration factor of 0.1	Not defined	Not defined
Loading cycles between propagations	2	1 (8 after the last release)	15 (30 for the first four releases) 5	1	1	1 2	2 (4 for the first release)	2

2.6.1 Crack propagation criteria

Overall, there are two principal crack propagation criteria used for numerical crack propagation. The first one consists of the nodes release after a given number of loading cycles and is the most employed procedure for this type of analysis [4, 14, 36, 40, 43, 44]. Although some authors considered the node liberation at maximum load, the literature recommends that the release should occur at minimum load to avoid convergence problems that could arise by propagating the crack at maximum load. In opposition to the crack growth criterion previously mentioned, at which crack propagation occurs after a specific number of load cycles, there is another crack growth criterion adopted by a few authors, based on the accumulated plastic strain, $\Delta\varepsilon_p$. This criterion is called Total Plastic Strain (TPS) and assumes that the damage accumulation controls FCG [46]. The crack tip node is released when its $\Delta\varepsilon_p$ value, which is supposed to be a material property, reaches a critical one [47]. This method is more realistic than the first one, which assumes a constant crack growth rate, nevertheless it is harder to employ. After each load/unload cycle, it is necessary to assess the equivalent plastic strain (PEEQ) value. If PEEQ reaches the critical value, the node is released. Otherwise, cycles are continued to be applied until the criterion is met, and so on.

2.7 Finite element method

The Finite Element Method (FEM) is a versatile mathematical tool widely used in various engineering applications, with a multidisciplinary character. This tool allows the modelling of a wide range of physical phenomena for which there isn't an exact solution that can be expressed analytically, including static and dynamic situations, enabling approaches to different areas such as Solid Mechanics, Fluid Dynamics, or Thermodynamics [48].

FEM plays a significant role in Fracture Mechanics by predicting the fatigue life of components with complex geometries [49]. Analytical methods become impractical in such cases due to the complexity of the stress distribution around the crack tip. In contrast, experimental fatigue tests are not only time-consuming but also expensive, making FEM an excellent alternative for determining the most essential parameters of Fracture Mechanics.

FEM starts with the division of the analysed geometry into small parts for which it is possible to know or obtain a mathematical description of their behaviour. In other words, one complex problem (geometry) is subdivided into various simpler problems (i.e. elements). This process of structured analysis of the parts rather than the whole is called discretization (Figure 2.7). This subdivision allows the computer to perform the task more efficiently. Each finite element and the mathematical laws that govern its behaviour contribute to the knowledge and analysis of the global problem. The transition from analysing each finite element as an individual entity to analysing the whole is called grouping or assemblage [50]. In this method an infinite number of unknown variables is replaced by a finite number of elements with well-defined behaviour and properties. These elementary subdivisions can take different shapes, such as quadrilaterals, triangles, among others and are connected by nodes, where the continuity of displacement fields is reinforced (Figure 2.8). Thus, finite-sized elements are obtained, hence the name of the method [12]. The set of elements and nodes is called mesh. The mesh plays a

fundamental role in a problem analysis, particularly in terms of its refinement (density of elements), which can make the results more or less accurate. The accuracy obtained generally increases directly with the number of elements used [51], which means that a fine mesh is expected to have more accurate results than a coarse mesh. However, a larger number of elements requires more computational effort and sometimes it becomes unbearable. One way to make the analysis more efficient without losing the necessary precision is to refine the critical zones of the component where stress concentration is predictable. The goal of this procedure is to obtain the intended results as accurate as possible, minimizing the simulation time and computational effort. To achieve this, it is necessary to create an appropriate mesh and choose a suitable element type in order to obtain good convergence results.

There are different types of integration in a finite element simulation. This method requires the integration of a large number of functions and, in order to simplify the resolution of problems related to finite elements, the simulation software uses techniques such as:

- Complete Integration - employs the full integration scheme to evaluate the integrals within each element. This means that the integrals are evaluated using a sufficient number of integration points, such as the Gaussian quadrature with a high degree of precision. Complete integration ensures high accuracy, particularly when dealing with nonlinear or complex phenomena. However, it can be computationally expensive and require higher simulation time since the number of integration points increases with the order of accuracy desired. The volumetric locking can be caused by this type of integration. This means that the elements assume an incompressible behaviour and become underformed because their stiffness matrix tends to infinity;

- Reduced Integration - aims to reduce the computational effort by reducing the number of integration points within each element. Instead of using the full integration process, such as employing Gaussian quadrature with numerous points, only a set of integration points is employed. Generally, reduced integration employs a single integration point for each element.This approach reduces the computational cost but may lead to less accurate results, especially for elements with highly distorted geometries. Hourglassing is associated with this type of integration. This phenomenon refers to a non-physical deformation pattern where elements exhibit excessive and unnatural hourglass-like shape distortions. It is a consequence of the under-constraint nature of the finite element method and the inability of certain element types to accurately capture all deformation modes. Hourglass modes are not representative of the actual physical behaviour of the system;

- Incompatible Modes Integration – consists on enhancing by incompatible modes the lower-order quadrilateral continuum elements to improve their bending behaviour. In addition to the displacement degrees of freedom, incompatible deformation modes are added internal to the elements. The primary effect of these degrees of freedom is to eliminate the shear stresses that are observed in regular displacement elements if they are loaded in bending. Furthermore, these degrees of freedom eliminate artificial stiffening due to Poisson's effect in bending. In regular displacement elements the linear variation of the axial stress due to bending is

accompanied by a linear variation of the stress perpendicular to the bending direction, which leads to incorrect stresses and an overestimation of the stiffness. The incompatible modes prevent such a stress from occurring. This technique is usually the one with the closest results to the analytical ones. Its main disadvantage is the high computational weight it requires to carry out the simulations [52].

Generally, a numerical simulation comprises three different stages: the pre-processing phase, the analysis phase, and the post-processing phase.

- The pre-processing phase consists of building the geometric model and defining the loading conditions the component is subjected to. This step involves defining the material properties, the type of finite elements, and the mesh to be used. Restrictions can also be defined regarding the degrees of freedom of the model and the presence or absence of contact between components for example, in order to simplify the analysis. These restrictions are referred to as boundary conditions.

- During the Analysis phase, all calculations are performed. Firstly, all the information contained in the input data file created in the pre-processing phase is checked. The solution convergence is monitored during the simulation to ensure stability and accuracy. If no detectable errors are found, the analysis is fully executed, and the output files are created containing all the information and results required by the user.

- Lastly, the post-processing phase is in charge of presenting all the information contained in the output files resorting to plots, graphs, animations, or other graphical representations to gain insights into the system behaviour. Some quantitative analyses are performed on the results like calculating averages, maximums, etc. In the end, the simulation can be validated by comparing the results with experimental data or theoretical predictions.

Overall, FEM is a very powerful tool with a wide range of engineering applications. Nevertheless it produces a lot of information that needs to be interpreted correctly, otherwise it can lead to future problems. In the right hands, these finite elements models can predict the useful life of components and preserve the safety of structures, ensuring human protection.

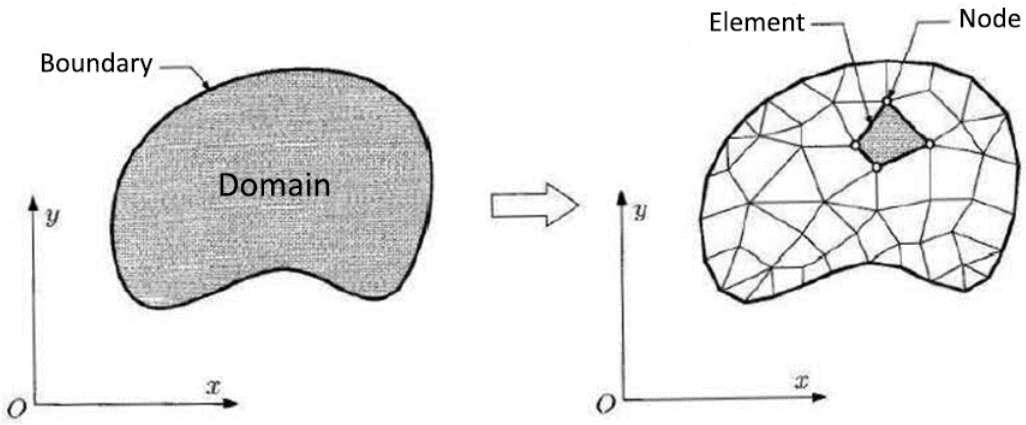

Figure 2.7: Schematic representation of the spatial discretization process of a finite element domain (from [50])

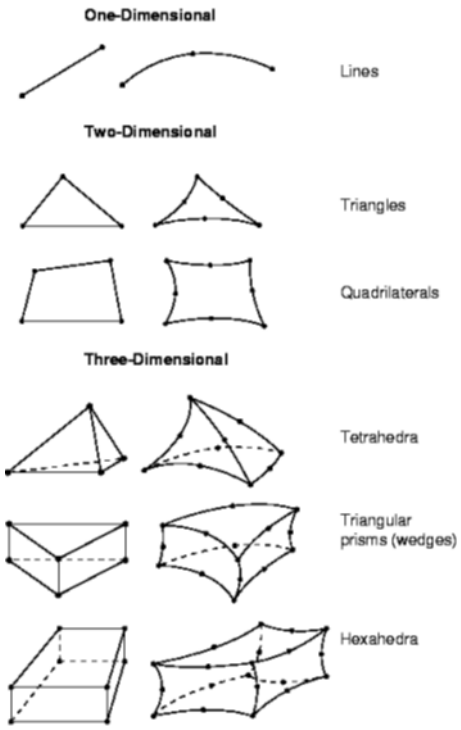

Figure 2.8: Types of finite elements (from [53])

Intentionally blank page.

Chapter 3

Case Studies

In this dissertation, two different case studies were conducted. The first one consisted of modelling a Compact-Tension (C(T)) specimen of an aluminium alloy. Several models were created, varying the thickness, the number of elements along the crack front, and the size of elements in the propagation zone to study the influence of these parameters on the values of CTOD and P_{open}. In the second case study, the C(T) specimen has a different geometry compared to the previous one, and it is made of a titanium alloy. The objective is to compare the numerically obtained values of the plastic CTOD with those provided by an experimental test, considering the same conditions.

Overall, the geometry of a C(T) specimen can be described by Figure 3.1, where B corresponds to the specimen thickness, W is the specimen width and a is the crack size. These dimensions are presented later in Section 3.1 for each case study, along with the properties of its constituent materials.

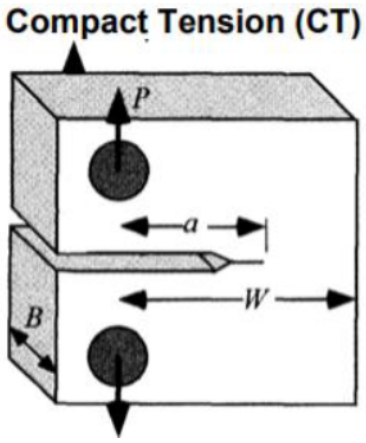

Figure 3.1: CT specimen (from [9])

3.1 Numerical modelling

3.1.1 Finite element software

All numerical simulations were performed using the finite element program Abaqus, 2017 version. This commercial software, which was marketed by SIMULIA, a brand of

Dassault Systemes S.A, was the chosen program for this dissertation due to its wide use for finite element analysis of computational models and reliable results obtained in fracture mechanics studies. This tool provides a broad range of analysis capabilities, including linear and nonlinear analysis, static and dynamic analysis, implicit and explicit analysis, and many others, offering robustness and accuracy. Additionally, it handles numerous element types, including 1D, 2D, and 3D elements, as well as distinguished elements for specific applications. Abaqus provides an intuitive and easy-to-use interface, making it simple to change material properties, boundary conditions and contact interactions so that it is possible to evaluate different conditions without having to create a whole different model. Other great capability of this software is the presence of a scripting interface (Python-based) that allows users to automate repetitive tasks and customize simulations.

As previously mentioned, a complete analysis in any finite element software, such as Abaqus, comprises three distinct stages: pre-processing, analysis and post-processing.

The model to be analysed must have information about the geometry, element's section properties, material properties, loads and boundary conditions, mesh, type of analysis, and type of data requested as output. These components are described in detail in the consulted literature [53–55]. This information is included in the pre-processing phase. When the model is complete, Abaqus/CAE (Complete Abaqus Environment, divided into modules) creates an input file with all the information about the model. Then, the Abaqus/Standard or Abaqus/Explicit modules (depending on the type of time integration) read the generated input file, perform the analysis, and return the information to Abaqus/CAE to allow monitoring the work progress, generating a file with the output data. Finally, the analysis outcomes can be checked through the visualization module by accessing and interpreting the output files.

The Abaqus/CAE interface is divided into modules, where each module defines a logical aspect of the modelling process. The model is being designed as you move from module to module. The methodology adopted to obtain the numerical models on Abaqus is divided in the following steps:

1. **Geometry generation**: In the *Part* module the component's type is defined, whether it is deformable or rigid, 2D or 3D, solid or shell, etc. After that the part geometry is sketched;

2. **Material definition**: In the *Property* module, the material's properties are defined (i.e. the elastic and plastic behaviour of the material). The created material is then assigned to a section that has specific information about the part's section;

3. **Global definition of the model**: In the *Assembly* module, the assembly of all constituent parts of the model is performed To do so, it is necessary to create the respective instances for each individual component and then grouping them together through their positioning in space, referring to a single global axes system;

4. **Definition of the analysis type**: In the *Step* module, the parameters that control and influence the finite element analysis are defined. There are two main types of analysis, the Static Implicit and the Dynamic Explicit. In a general way, the implicit method is suitable for static and quasi-static analyses, since the effects of inertia, mass, velocity and acceleration are not considered. Iterations are based

on the Newton-Raphson method and the time increment is not limited allowing simulations with relatively large time increments. In contrast, the explicit method is used for dynamic situations. In this type of analysis, the time factor plays a very important role since the calculation of the acceleration field is obtained from temporal increments, which must be very small in order to maintain stability and ensure convergence to the real solution. After the creation of the necessary steps, it is possible to select the type of results to be presented at the end of the simulation in the *Field Output Request* and *History Output Request* submenus;

5. **Definition of the interactions**: The interactions between parts are created in the *Interactions* module. It is possible to define contact and friction parameters, like friction coefficients and specify the contact behaviour as surface-to-surface, edge-to-surface, etc;

6. **Definition of the boundary conditions**: In the *Load* module there are two submenus: *BC* and *Load*. In the first one the boundary conditions are created. These boundary conditions aim to limit the motion of the model under analysis, directly influencing the degrees of freedom, which are characterized by translation and/or rotation. In the second submenu refered, the loads are created and applied to the components;

7. **Mesh generation**: The *Mesh* module is where the finite element mesh is created. This module includes the selection of the element type and formulation.The size and number of elements are also defined by changing the seeds parameters.The mesh has to be adapted to the geometric model, and higher refinement is recommended only in regions considered critical so that the calculations are as accurate as possible and the computational effort is optimized;

8. **Analysis submission and simulation**: In order to submit our problem for analysis, it is necessary to select the *Create Job* option and then *Submit*, in the *Job* module;

9. **Visualization of the results**: Lastly, when the job is completed, the program ended the analysis and is ready to present the obtained results. From the main menu, selecting the *Plot* option and the *Undeformed shape* suboptions and *Deformed shape* allows the visualization of the initial and deformed configurations of the part, before and after applying the load, respectively. Plots and specific values can also be extracted and exported to Excel files.

3.1.2 Geometry and dimensions of the CT specimens

As mentioned before, the numerical tests were performed with C(T) specimens and its dimensions are presented in Figure 3.2 (a) and (b).

The first model has a width, W, of 50 mm, an initial crack length, a_0, of 24 mm, therefore a_0/W is 0.48. The thickness of the specimen was varied during this work, starting with plane stress and plane strain 2D models and then proceeding to 3D models with different thickness values, which are going to be specified later. The second C(T) model has a width, W, of 20 mm, an initial crack length, a_0, of 7.48 mm, so a_0/W is 0.374. Initially 2D specimens were modelled considering plane strain and plane stress

states, as well as the first model, and then a 3D model with 1 mm of thickness. The geometry and size of the specimens are in accordance with ASTM E647 standard [3].

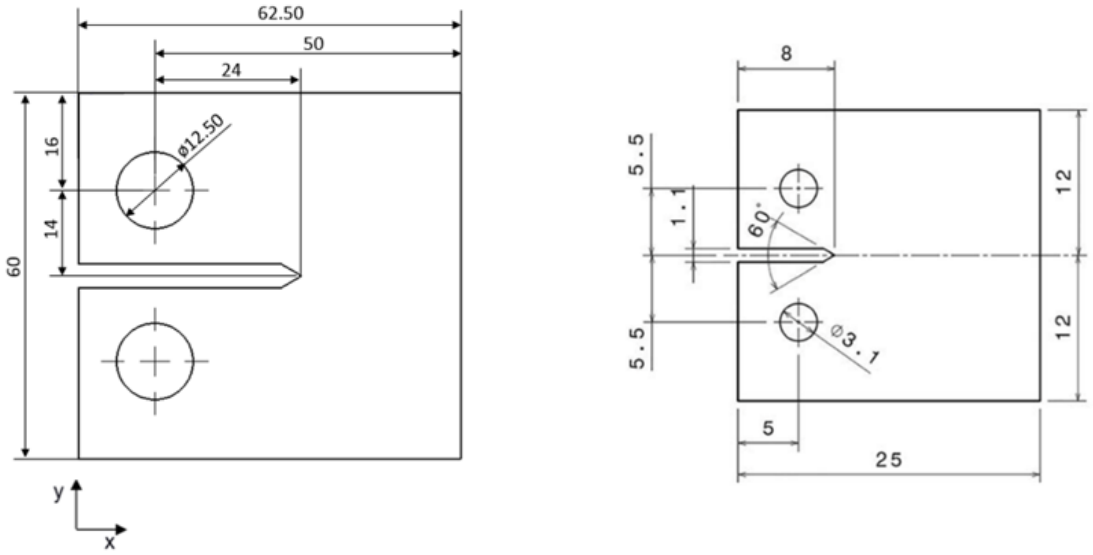

(a) (b)

Figure 3.2: (a) Geometry of the aluminium alloy specimen; (b) Geometry of the titanium alloy specimen.

3.1.3 Material modelling

Plasticity theory

Figure 3.3 shows a typical stress-strain curve for a metal obtained by a uniaxial tensile test. For stress values lower than the yield stress, point A, the material has a linear elastic behaviour described by Hooke's law, which means there is a linear relation between stress and strain. This regime is characterized by a reversible deformation behaviour after removing the applied load. When the elastic limit (yield point) is exceeded, the material undergoes plastic deformation.

If the specimen is unloaded at point B, it will return along the path BC, parallel to the original elastic limit, showing elastic recovery, but with different mechanical properties from the initial ones. The strain that remains after unloading is called plastic deformation, which is permanent and irreversible. If the material is reloaded, the stress-strain curve will retrace the unloading path CB until it reaches the plastic state again. Further increasing the stress will cause the curve to follow BD. This increase in stress to carry out plastic deformation is known as hardening. The perfectly plastic line represents an idealized plastic deformation behaviour in which the material keeps deforming without any additional stress required. However, most materials exhibit strain hardening, where the stress required for further plastic deformation increases with strain.

The distinction between the elastic and plastic behaviour of a material can be described by the representation of the yield surface (plasticity surface). This surface cor-

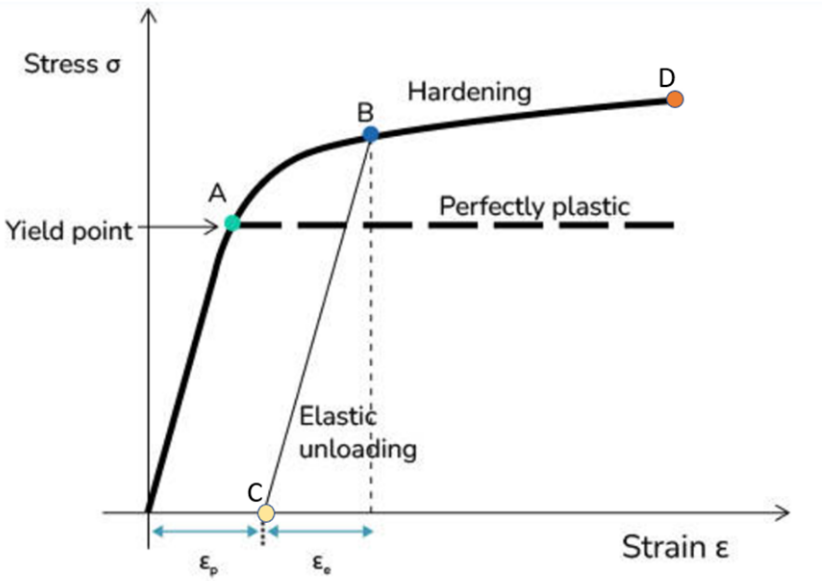

Figure 3.3: Typical stress-strain curve obtained from a uniaxial tensile test (Adapted from [56])

.

responds to all stress states at which plastic deformation begins. Thus, all stress states within the surface are in the elastic regime, contrary to those situated on the surface, which are in the plastic regime. Its representation can be made in the space of Cauchy's principal stresses (σ_1, σ_2, and σ_3), as shown in Figure 3.4. The shape of the yield surface varies according to the adopted yield criterion, being Tresca criterion (hexagonal surface) and von Mises criterion (elliptical surface) the most well-known isotropic yield criteria. The von Mises yield criterion is the most widely used and considers that plastic deformation begins when the critical value of elastic strain energy is reached. This criterion can be expressed by the Equation 3.1:

$$(\sigma_1 - \sigma_2)^2 + (\sigma_1 - \sigma_3)^2 + (\sigma_2 - \sigma_3)^2 = 2\sigma_0^2 \tag{3.1}$$

The axis of the geometric representations of both yield criteria coincides with the diagonal defined by the points that respect the condition $\sigma_1 = \sigma_2 = \sigma_3$. These points located represent purely hydrostatic states of stress, which do not have any influence on the yielding. The deviatoric plane, which is characterized by $\sigma_1 + \sigma_2 + \sigma_3 = 0$, is perpendicular to the surface axis and contains the origin of the coordinates.

Crystallographic and phenomenological constitutive models describe and predict the elastic-plastic behaviour of metal materials. The first, represent the microscopic theory of plasticity and assumes that the material is constituted by one or multiple crystals forming a crystalline structure. On the other hand, the second represents a macroscopic perspective on plasticity, assuming that the material is homogeneous and is only valid at temperatures for which thermal phenomena may be neglected. This theory can predict the distribution of stresses and strains in polycrystalline metals, not only in situations

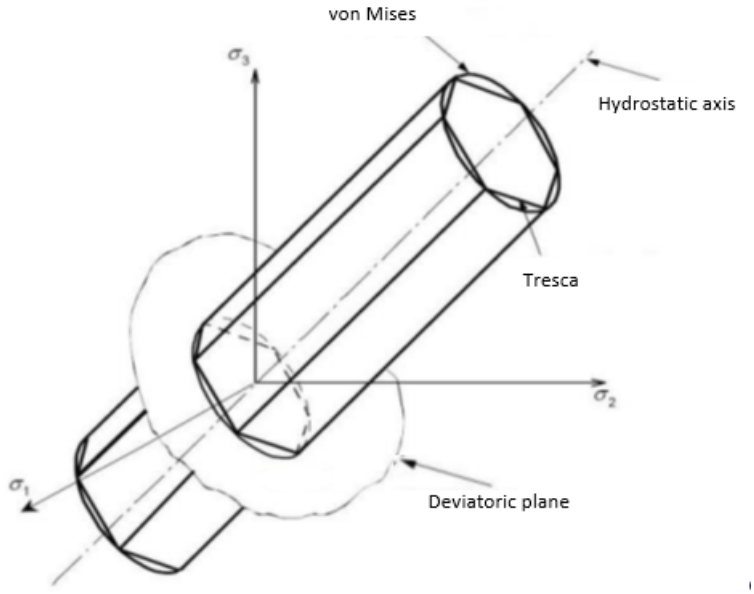

Figure 3.4: Geometric representation of Tresca and von Mises yield criteria in Cauchy's principal stress space (Adapted from [57])

where the elastic and plastic strains are comparable in magnitude, but also in situations where the plastic strains are large enough for the elastic strains to be disregarded [58].

Phenomenological constitutive models usually include:

- Yield criteria, to define the limit of the elastic behaviour/onset of plastic deformation (yield surface);
- Hardening laws, to describe how the yield surface evolves during plastic deformation;
- Plastic flow rule, which provides a relationship between the stress state and the plastic deformation increment.

Yield criteria

The yield criteria can be described by the following function, Equation 3.2:

$$f(\sigma' - X, \bar{\varepsilon}^p, \alpha, \beta) = \bar{\sigma}(\sigma' - X, \alpha) - Y(\bar{\varepsilon}^p, \beta), \tag{3.2}$$

where $\bar{\sigma}(\sigma' - X, \alpha)$ is the equivalent stress, which is given by a yield criterion and $Y(\bar{\varepsilon}^p, \beta)$ represents the evolution of the yield stress during deformation, according to the hardening law employed. The equivalent stress $\bar{\sigma}(\sigma' - X, \alpha, \beta) = \bar{\sigma}$ has as variables, σ', the deviatoric Cauchy stress tensor and X, the deviatoric back-stress tensor. The portion $Y(\bar{\varepsilon}^p) = Y$ represents the flow stress and depends on the equivalent plastic strain, $\bar{\varepsilon}^p$. Lastly, α and β represent the material parameters of the constitutive model [59].

The yield surface can be expressed by Equation 3.3:

$$f = \bar{\sigma} - Y = 0 \iff \bar{\sigma} = Y \tag{3.3}$$

If the stress state of the material is located inside the yield surface, i.e., the relation $\bar{\sigma} < Y$ is verified, there is only elastic deformation. On the other hand, plastic regime occurs when the increment of the plastic strain tensor is normal to the yield surface for a stress state where $\bar{\sigma} = Y$.

Hardening Laws

Plastic deformation causes metals and their alloys to become hardened, resulting in an increase of the required stress to induce further plastic deformation. Strain hardening laws describe the evolution of the yield surface throughout plastic deformation. There are essentially two types of hardening laws, isotropic and kinematic.

The isotropic hardening model assumes that the yield surface increase in size during continued plastic deformation without a change in its centre position and initial shape (homothetic expansion), as represented in Figure 3.5. This model was proposed by Odquist [60]. Although its simplicity, it has some limitations when trying to reproduce the material strain path because the yield surface is uniquely defined by the final plastic state of stress [61]. Some metallic materials present stress saturation at large deformations. The Voce law [62] takes this phenomenon into account and can be written as follows:

$$Y = Y_0 + (Y_{\text{Sat}} - Y_0)[1 - \exp(-C_Y \bar{\varepsilon}^p)], \tag{3.4}$$

where Y_0 is the yield stress, Y_{Sat} is the isotropic saturation stress, C_Y is a parameter of the Voce law that determines the rate at which the isotropic hardening reaches saturation, meaning a material with higher value of C_Y reaches its saturation stress faster, and $\bar{\varepsilon}^p$ is the equivalent plastic strain. Note that the values of Y_0, Y_{Sat}, and C_Y need to be determined experimentally for a specific material. The Swift law can also be used to characterize the isotropic hardening and is described by [63]:

$$Y = C \left[\left(\frac{Y_0}{C} \right)^{\frac{1}{n}} + \bar{\varepsilon}^p \right]^n, \tag{3.5}$$

where Y_0, C, $\bar{\varepsilon}^p$ and n are the material parameters.

The Bauschinger effect arises when the plastic surface undergoes some changes in shape beyond isotropic expansion due to a reduction of the yield stress in compression after a tensile load, or *vice versa*. In this case, an isotropic hardening law isn't enough to characterize the material hardening behaviour [64]. The kinematic hardening model consists of a rigid translation of the yield surface, without a change in shape and size, as represented in Figure 3.6. Contrary to the isotropic hardening, this model considers the Bauschinger effect and can predict the development of anisotropy. Because of that, the kinematic hardening model is recommended for describing plastic deformation under strain path changes.

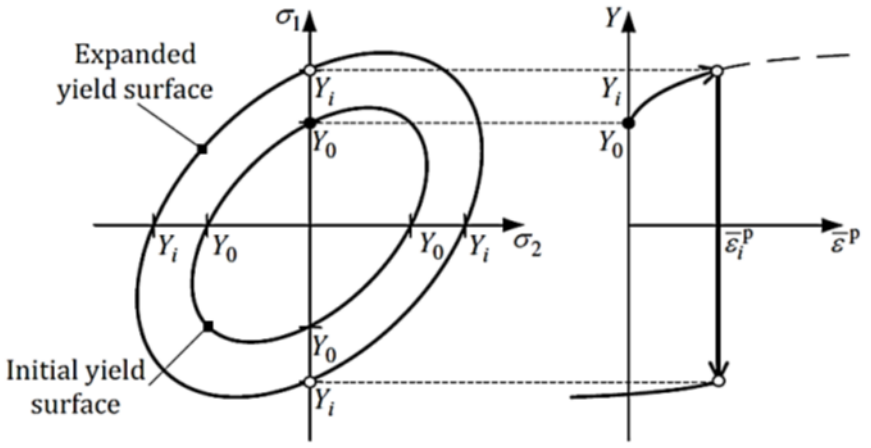

Figure 3.5: Representation of the evolution of the yield surface in isotropic hardening, on the left and, on the right side the corresponding stress *vs* plastic strain curve (Adapted from [59])

A non-linear kinematic model was proposed by Armstrong & Frederick [65], which can be characterized by the following expression:

$$\dot{X} = C_X \left[\frac{X_{\text{Sat}}(\sigma' - X)}{\bar{\sigma}} - X \right] \dot{\bar{\varepsilon}}^p, \tag{3.6}$$

where C_X is a parameter with a similar meaning to C_Y in Equation 3.5, but regarding kinematic saturation stress; X_{Sat} is the kinematic saturation stress, $\bar{\sigma}$ is the equivalent stress and $\dot{\bar{\varepsilon}}^p$ is the equivalent plastic strain rate.

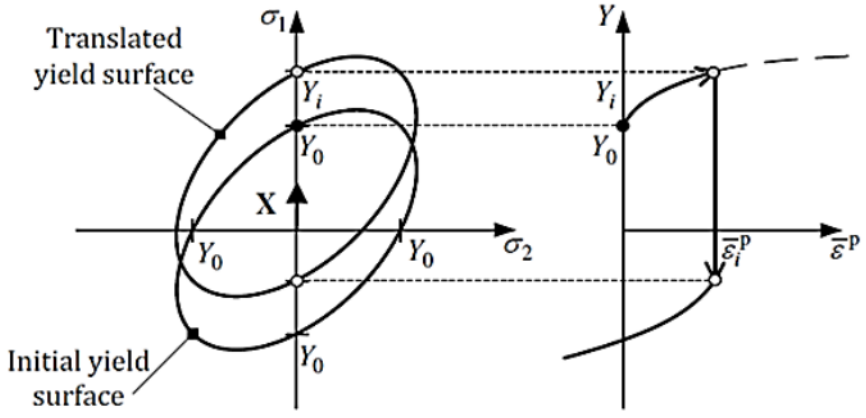

Figure 3.6: Representation of the evolution of the yield surface in kinematic hardening, on the left and, on the right side the corresponding stress *vs* plastic strain curve (Adapted from [59])

Materials studied

Two materials were considered: an AA2024-T351 aluminium alloy and Grade 2 Titanium, one for each case study.

The AA2024-T351 is an aluminium alloy belonging to 2000 series. Like other 2000 series alloys, 2024 is primarily alloyed with copper. It also contains manganese and magnesium and can sometimes contain smaller amounts of other elements such as silicon, iron, chromium, zinc and/or titanium. The "T351" designation refers to the heat treatment process applied to the alloy. T351 involves solution heat treatment followed by artificial aging. This treatment enhances the alloy's strength and hardness while maintaining its overall toughness. This material has a low environmental impact, low density, high cyclic fatigue resistance, high strength, good workability, and fair machinability. Even though possesses good corrosion resistance, especially in atmospheric environments, it is susceptible to stress corrosion cracking, so its exposure to certain environments, such as marine or high-chloride environments, should be prevented. This means that these types of alloys are ranked favourably when both fatigue behaviour and environmental impact are considered. In fact, this material is the most used aluminium alloy in the aircraft industry and is primarily found in wing and fuselage structures that are frequently under tension [66]. Apart from aerospace industry, this aluminium alloy is also widely used in the production of automotive components and structural parts requiring high strength-to-weight ratios.

On the other hand, Titanium Grade 2 is commercially pure (99% minimum titanium). Each grade has slight variations in chemical composition that affect mechanical properties. Grade 2 has outstanding corrosion resistance in highly oxidizing and mildly reducing environments, including chlorides, and useful strength (similar to austenitic stainless steels) at low density. It has also good weldability and is easily formable. For these reasons, Grade 2 is the most used grade of titanium being well suited to applications in the marine, chemical processing, and desalination industries. This alloy is widely used in many industrial components like reaction and pressure vessels, tubing or piping systems, heat exchangers, etc [67–69].

Identification of elasto-plastic constants of the materials

Borges et al. [36] did an optimization procedure to identify the material parameters that best describe the plastic behaviour of the studied aluminium alloy. These parameters were obtained by minimising the following least-squares objective function, $F(A)$:

$$F(A) = \sum_{i=1}^{M} \left(\frac{\sigma^{\mathrm{Fit}}(A) - \sigma^{\mathrm{Exp}}}{\sigma^{\mathrm{Exp}}} \right)_i^2, \tag{3.7}$$

where $\sigma^{\mathrm{Fit}}(A)$ and σ^{Exp} are the fitted and the experimentally measured values of true stress, respectively. A is the set of material parameters that minimises $F(A)$ and M is the total number of experimental points. The minimization of $F(A)$ was performed through the use of the Generalised Reduced Gradient (GRG2), which is a nonlinear optimisation algorithm [70] included in the Microsoft Excel Solver tool.

The titanium grade properties were obtained from the experimental tests carried out by the author of [71]. Table 3.1 shows the material parameters that describe the elastic and plastic behaviour for both materials. The elastic behaviour is assumed isotropic and described by Hooke's law. On the other hand, the plastic behaviour is described by the von Mises yield criterion coupled with Armstrong & Frederick kinematic hardening law. In fact, the titanium alloy under consideration exhibits a perfectly plastic behaviour with nonlinear kinematic hardening [71].

Table 3.1: Material parameters.

Material	**Hooke's Law Parameters**		**Isotropic Hardening (Swift)**			**Kinematic Hardening (Armstrong-Frederick**	
	E [GPa]	ν [-]	Y_0 [MPa]	C [MPa]	n [-]	C_X [-]	X_{Sat} [MPa]
AA2024-T351 [36]	73	0.33	288.96	389.00	0.056	138.80	111.84
Titanium Grade 2 [71]	105	0.37	344.25	-	-	139.51	173.48

3.1.4 Boundary conditions and Load

At the beginning of this study, 2D numerical simulations were analysed considering plane stress and plane strain states. Then 3D simulations were performed on models with different thickness values.

Since the C(T) specimen has two planes of symmetry, in order to reduce the associated numerical weight and simulation time without having impact on the results, only 1/4 of the specimen was modelled on 3D models and 1/2 on 2D models, considering adequate boundary conditions. Figures 3.7 (a) and 3.8 (a) represent the boundary conditions applied in the 2D models (TP-Plane stress state and DP-Plane strain state), for case study 1 and case study 2, respectively. Regarding the 3D models, as the thickness value isn't negligible, only 1/4 of the specimen was modelled so it was necessary to impose restrictions to deformation perpendicular to the main face of the specimen. Therefore, in addition to the Figures 3.7 (a) and 3.8 (a), Figures 3.7 (b) and 3.8 (b) show a lateral view of the specimens with the referred symmetry conditions. For 2D models, a fixed support was applied at the last node on the right end side of Figure 3.7 (a) and Figure 3.8 (a). For 3D models, fixed supports were applied at the last row of nodes along the thickness direction of the sample.

By nature, crack faces get prematurely into contact during the unloading phase. In order to take into account the physical contact between the crack flanks (crack closure phenomenon) a rigid surface aligned with the crack symmetry plane was modelled. A frictionless contact behaviour was established between the fracture-plane solid elements and the rigid surface. The surface is fixed and doesn't allow the specimen to deform below it.

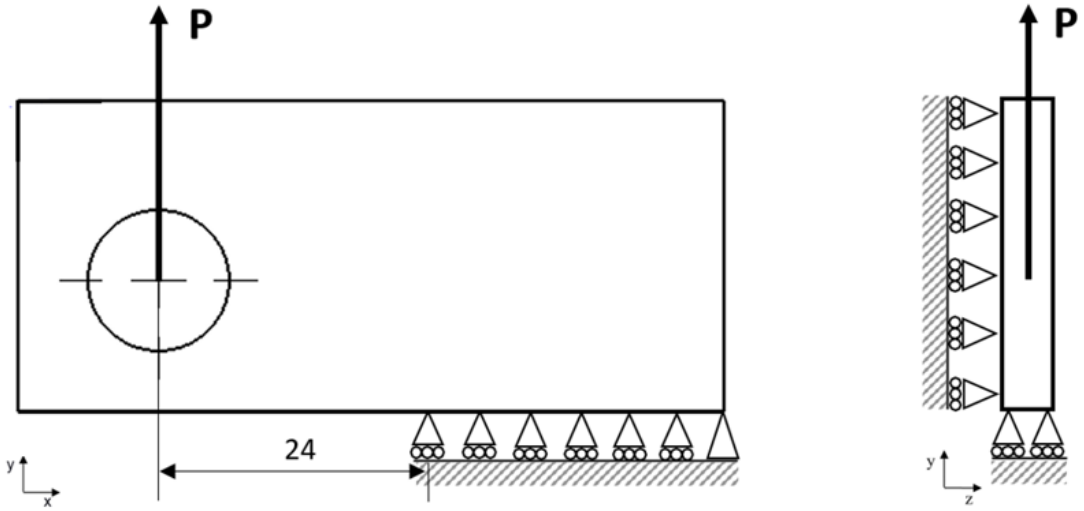

(a) (b)

Figure 3.7: Load and boundary conditions of the Case study 1 model. (a) 3D in plane, TP and DP; (b) Lateral view of the 3D model.

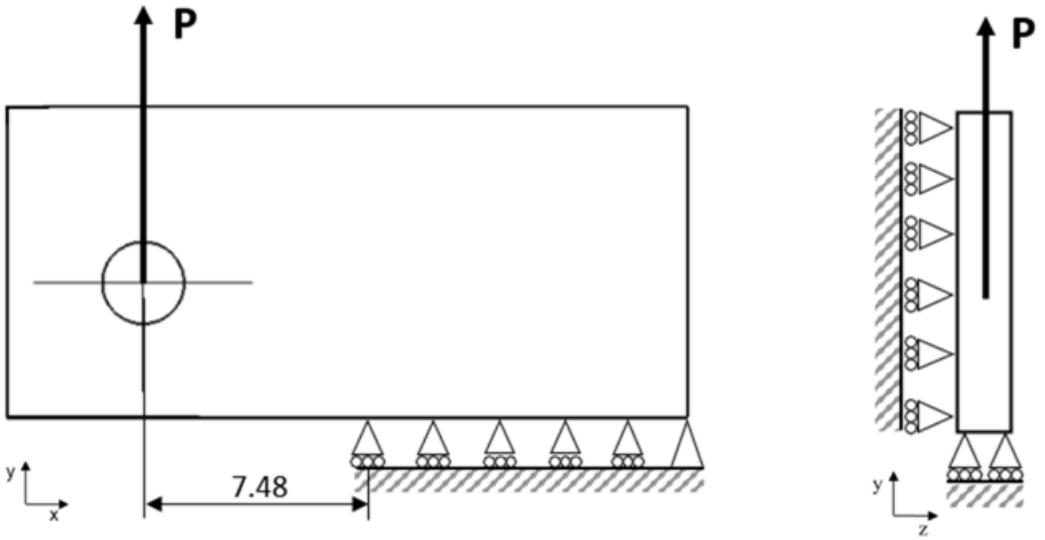

(a) (b)

Figure 3.8: Load and boundary conditions of the Case study 2 model. (a) 3D in plane, TP and DP; (b) Lateral view of the 3D model.

The numerical model corresponding to case study 2 was slightly different from the experimental one regarding the crack propagation starting location. This is because, experimentally, the propagation started at 3 mm from the origin (point x=0, y=0) and reached 8 mm in the x direction, which would be computationally impractical with the type of simulations performed. Considering a refined crack propagation zone with 8-micron square elements, simulating a propagation of 5 mm would require a very high

number of crack increments (released nodes) to achieve the intended crack length. This means that a huge computational effort and time would be necessary. Therefore, a crack growth up to 8 mm was still simulated but starting with an initial crack length of 7.48 mm.

The specimens were subjected to a cyclic load of constant amplitude (Figure 3.9) applied at the hole. In the particular case of the AA2024-T351, the maximum and minimum load values were initially 41.67 and 4.167 N, respectively which correspond to a $K_{\max}$, $K_{\min}$ and ΔK equal to 16.82, 1.682 and 15.14 MPa.$m^{0.5}$, respectively, according to Equation 3.8. Since the $K_{\max}$ and $K_{\min}$ values were kept constant for all models, as well as the load ratio, R=0.1, the $P_{\max}$ and $P_{\min}$ varied according to the thickness of the model to be analysed. The load values were then calculated through the equation below:

$$K_I = \frac{P}{B\sqrt{W}} f\left(\frac{a}{W}\right) \tag{3.8}$$

$$f\left(\frac{a}{W}\right) = \frac{2+\frac{a}{W}}{\left(1-\frac{a}{W}\right)^{\frac{3}{2}}}\left[0.886 + 4.64\left(\frac{a}{W}\right) - 13.32\left(\frac{a}{W}\right)^2 + 14.72\left(\frac{a}{W}\right)^3 - 5.6\left(\frac{a}{W}\right)^4\right] \tag{3.9}$$

where K_{I} is the stress intensity factor, B is the specimen thickness and $f(\frac{a}{W})$ represents a dimensionless function that depends on the crack size (a) and the specimen width (W). The load values (P) are then obtained maintaining everything constant and only replacing the thickness value accordingly to the model in question. Table 3.2 resumes the load values adopted for the aluminium numerical models.

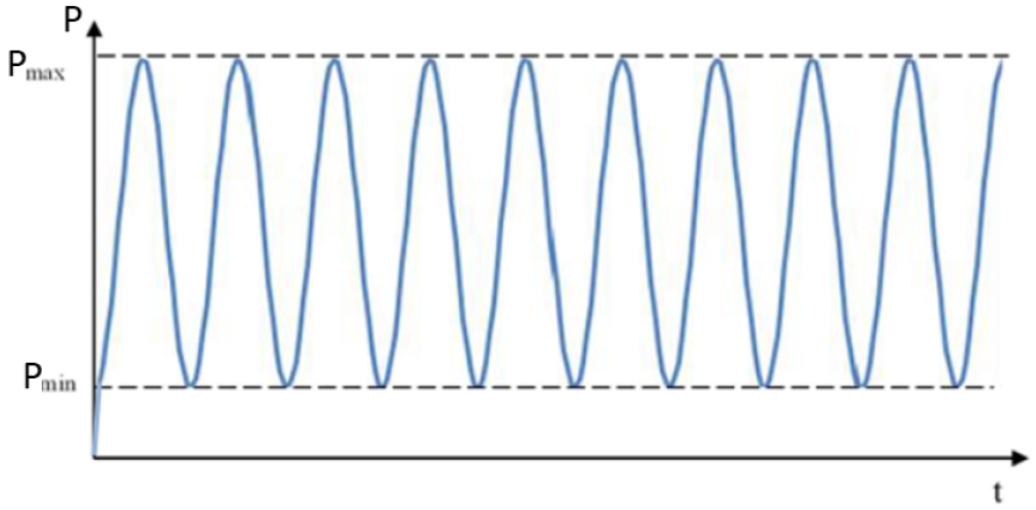

Figure 3.9: Representation of the cyclic load applied (Adapted from [4])

Table 3.2: Thickness and load parameters adopted in the Case study 1 analysis.

B [mm]	$\mathbf{P_{min}}$ **[N]**	$\mathbf{P_{max}}$ **[N]**
0.1	4.167	41.67
0.5	20.835	208.35
1	41.67	416.7
3	125.01	1250.1
6	250.02	2500.2

Although the bidimensional models have no thickness, when assigning a section to the part during the pre-processing phase, were considered 0.1 mm plane stress/strain sections. To these models correspond a maximum and minimum load values of 41.67 and 4.167 N, respectively.

For the Titanium Grade 2 specimen, the initial idea was to simulate only 1 mm thickness models, since it was the thickness of the experimental specimen, in which at first were considered plane stress and plane strain states. Assuming once again R=0.1, the maximum and minimum load values were 750 and 75 N, respectively.

3.1.5 Finite element mesh

The finite element mesh, illustrated in Figure 3.10, was divided in two principal regions: (i) a refined crack growth region with quadrilateral elements of either 8x8 µm^2 or 16x16 µm^2, to ensure greater accuracy in the results, and a coarser mesh in the remaining volume of the specimen, to reduce the computational cost. The type of elements used are related to the dimension of the problem. On the 2D models, CPE4R elements were used for plane strain situations, that consist of 4-node bilinear plane strain quadrilaterals with reduced integration and hourglass control, and CPS4R elements for plane stress cases, corresponding to 4-node bilinear plane stress quadrilaterals with reduced integration and hourglass control as well. In 3D models, C3D8R elements were used which correspond to 8-node linear bricks with reduced integration and hourglass control. The total number of elements varied with the different models, since there were models with different thicknesses, and the elements size at the refined zone also affected the global mesh. It was considered a bias ratio of 5 along the thickness so that the elements get smaller towards the surface area. The figures below show an example of a mesh on the main surface created for three-dimensional models, highlighting the crack propagation zone, where Figure 3.10 (b) corresponds to a zone with 16x16 µm^2 elements while Figure 3.10(c) corresponds to 8x8 µm^2 elements. The first node released is marked with a red dot.

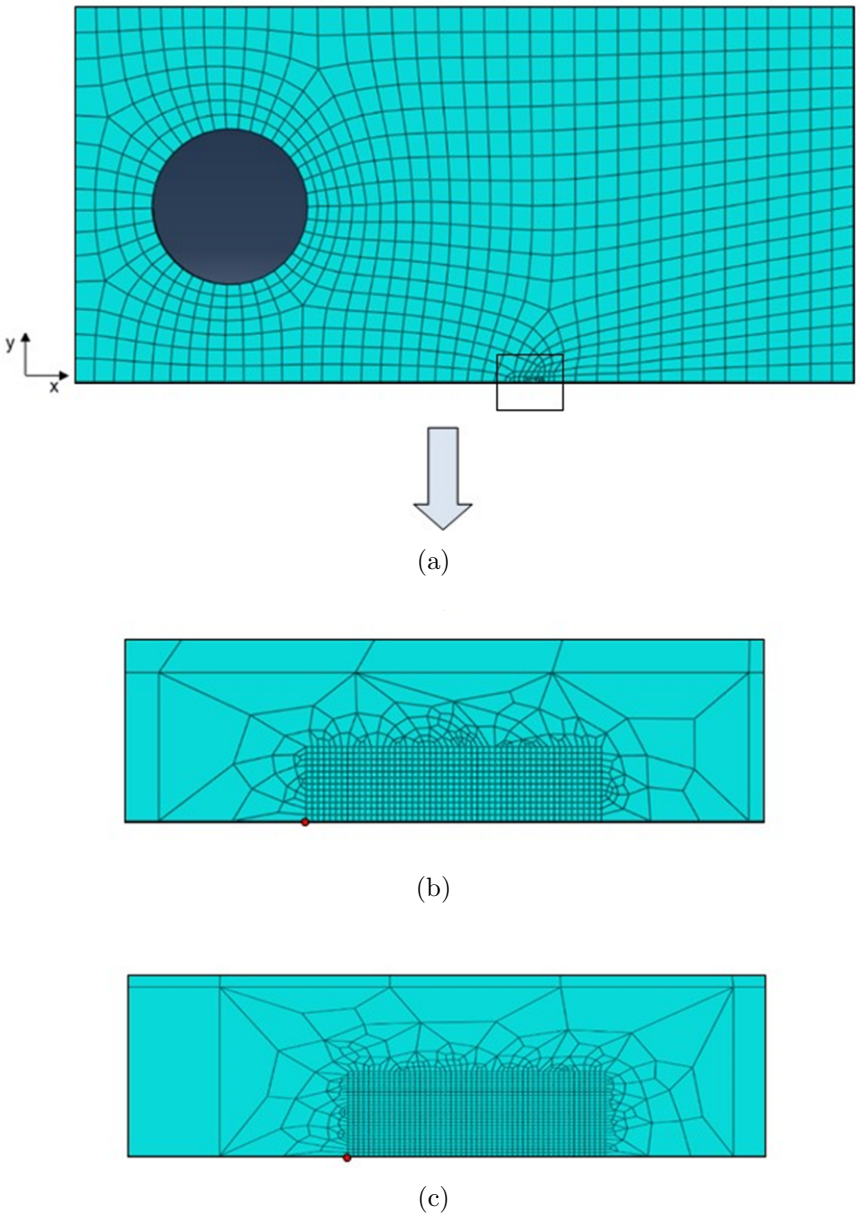

(a)

(b)

(c)

Figure 3.10: (a) Mesh of the of C(T) specimen model in the plane; (b) Details of the refined zone for 16 µm elements; (c) Details of the refined zone for 8 µm elements.

3.1.6 Crack propagation

Most studies conducted recently by other authors used a higher number of load cycles and a larger crack propagation compared to the present study. For instance, Borges et al. [36], under the same conditions, analysed 160 crack propagations with node release occurring every five load cycles for 2D models. However, since one of the main objectives of this work is to understand what happens in thickness (using 3D models), as the thickness value increased, the number of elements in the model increased drastically, making them computationally very heavy. For these reasons, it was decided

to reduce the size of the refined zone (where node release occurs) and consequently decrease the number of crack propagations and load cycles. So, in the present study, crack propagation was simulated by successive debonding at minimum load of all crack front nodes. Between each crack increment, which corresponds to the size of one finite element in the refined region (8 µm or 16 µm), two load cycles were applied.

For each simulation, 100 load cycles were performed, corresponding to a total crack propagation of Δa=49×16=784 µm for 16 µm elements size at the refined zone. 49 corresponds to the number of propagation analysed and comes from half of the load cycles minus 1, since the node release occurs every two cycles and the last propagation was not considered. Then the 8 µm elements mesh was compared with the 16 µm mesh for the same crack propagation, considering an intermediate propagation since the simulation time increased substantially with the reduction of the elements size. So, the analysed propagation corresponds to Δa=48×8=384 µm and Δa=24×16=384 µm for 8 µm and 16 µm, respectively, where 48 and 24 are the number of propagations for each case. The CTOD was measured at the first node behind the crack tip, i.e. at a distance of 8 µm or 16 µm from the crack tip, as represented in Figure 3.11.

For the application of 100 load cycles, 200 steps were created in the software for each finite element model, where every two load cycles, a set of nodes was released, requiring the updating of the boundary conditions of these nodes to no longer restrict their movement, and so on. Since this procedure would become repetitive and exhaustive, Python scripts were created to automate the creation of steps and new boundary conditions during those load cycles to simulate the crack propagation. These scripts can be consulted in Appendix B.

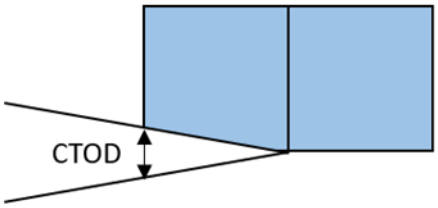

Figure 3.11: CTOD measurement point.

3.2 Numerical simulations performed

Table 3.3 resumes every numerical simulation performed on the aluminium specimen, case study 1, while Table 3.4 refers to the titanium specimen model simulations, case study 2. Parameters like the stress intensity factor, K_{I}, the load ratio, R, and the initial crack length, a_0, were equal for every simulation for each case study. On the other hand, the thickness value of the specimen, the number of elements along the crack front, the elements size in the refined crack propagation zone and the load value were modified according to the table below. At first, the crack propagation zone was larger but as the thickness and number of elements increased on the 3D models, it was decided to reduce the refined zone just to the essential size, enough to analyse the defined number of prop-

agations. For case study 2, only the dimensional component was changed, between 3D and 2D (both plane stress and plane strain states), with the main goal of comparing the obtained results with the experimental under the same conditions. In case study 2, the total number of elements are very similar on the 3D models because some areas of the specimens, that don't have influence on this study, were less refined to reduce the simulation time.

Table 3.3: Variables for all case study 1 models.

	Thickness (mm)	Number of elements through thickness	Elements size at the crack propagation zone (µm)	Crack propagation zone size (mm x mm)	Total number of elements	Maximum load, R=0.1 (N)
3D	0.1	2	16	0.8 x 0.2	1420	41.67
	0.5	10	16	0.8 x 0.2	7065	208.35
	1	20	8	0.4 x 0.2	21570	416.7
	1	20	16	0.8 x 0.2	15030	416.7
	1	60	16	0.8 x 0.2	43590	416.7
	3	60	8	0.4 x 0.2	64710	1250.1
	3	60	16	0.8 x 0.2	43590	1250.1
	6	120	16	0.8 x 0.2	87180	2500.2
2D	0.1 - DP	-	8	1.28 x 0.8	19060	41.67
	0.1 - TP	-	8	1.28 x 0.8	19060	41.67
	0.1 - DP	-	16	1.28 x 0.8	5916	41.67
	0.1 - TP	-	16	1.28 x 0.8	5916	41.67

Table 3.4: Variables for all case study 2 models.

	Thickness (mm)	Number of elements through thickness	Elements size at the crack propagation zone (µm)	Crack propagation zone size (mm x mm)	Total number of elements	Maximum load, R=0.1 (N)
3D	1	20	8	0.52 x 0.2	23380	750
	0.6	20	8	0.52 x 0.2	23580	450
	0.2	20	8	0.52 x 0.2	23130	150
2D	1 DP/TP	-	8	0.52 x 0.2	2578	750

Chapter 4

Results and Discussion

This chapter presents the obtained results like CTOD and crack opening load graphs, plastically deformed zones, crack profiles, etc, for case study 1. For case study 2, a comparison between the numerical and provided experimental results, in terms of CTOD and plastic ΔCTOD curves, is presented.

4.1 Case study 1

4.1.1 CTOD *vs* force

This subchapter will focus on the CTOD results obtained along the crack front as a function of the applied load for the aluminium specimens. All the curves presented correspond to the 2^{nd} loading/unloading cycle, with two cycles applied for each crack propagation. The load was normalized for all cases in this subchapter, as numerical models with different thicknesses imply different load values. Therefore, all values were normalized by the maximum load applied to the respective model. In turn, CTOD was measured at the node immediately behind the crack tip, i.e. at the node located at a distance of 8 µm or 16 µm, depending on the finite element mesh used. The values represented in the graphs of this subchapter correspond to half of the CTOD (CTOD/2) since due to the symmetry conditions considered (upper half of the specimen) the software only provides values corresponding to half of the vertical displacement.

Figure 4.1 presents the curves that relate the vertical displacement, CTOD, with the applied load concerning the specimen with a thickness of 3 mm, 60 elements along the crack front, and 16 µm elements along the crack propagation region in the plane. The aim of this figure is to compare the CTOD at the specimen's surface with the CTOD from the simulation in plane stress state, and the CTOD at half the specimen's thickness with the CTOD from the simulation in plane strain state, as well as the four obtained curves among themselves. It's worth noting that the curves in each graph were obtained for equal crack length: The curves in Figure 4.1(a) correspond to a crack propagation of Δa=384 µm (24 propagations), while Figure 4.1(b) corresponds to a crack propagation of Δa=784 µm (49 propagations).

For 24 crack propagations, the DP curve initially coincides with the "half thickness" curve. However, for higher load values, the curves start to deviate, with higher CTOD values being reached at half thickness. On the other hand, when comparing the TP curve with the one relative to the specimen's surface, significant differences are observed.

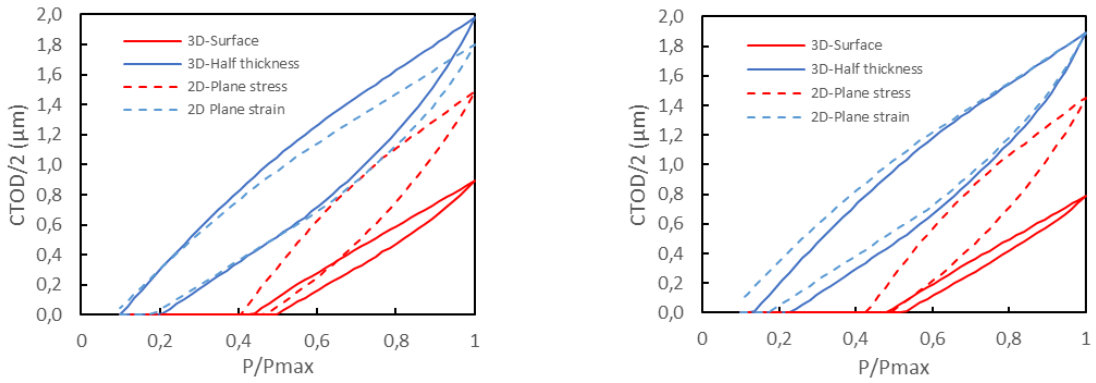

Figure 4.1: CTOD vs force along the crack front: (a) Δa=384 µm; (b) Δa=784 µm.

The TP curve shows almost entirely much higher CTOD values. Now, analysing the curves corresponding to 49 crack propagations, it can be noticed that the DP and "half thickness" curves approach each other for higher load values, coinciding at the maximum load. Once again, there is a considerable separation between the TP and "surface" curves. In general, in the plane stress state, the CTOD values are lower than in the plane strain state, which may be a consequence of the crack closure phenomenon, that occurs mainly in plane stress state. On the other hand, the crack closure is much lower (or null) for a plane strain state because there is no deformation along the thickness direction. Consequently, the CTOD reaches higher values in DP considerations. For the same reason, it is also evident that the crack opens more at half thickness (like the DP simulations) since the CTOD values are much higher compared to the surface. The force required to open the crack is greater at the surface which means that, for a given force, the crack will first open in thickness.

Another important factor to highlight is that for a higher number of propagations, the crack required higher force values to open. In fact, when a crack advances, the material ahead of the crack tip undergoes deformation. This deformation absorbs some energy, which must be supplied by the applied load to continue crack propagation. The further the crack advances, the more deformation is required, leading to an increase in the crack opening load. In the plane stress state and at the surface, the crack needed a load between 40% to 60% of the maximum load to open, remaining closed for relatively low loads. In contrast, in DP and at half thickness, the crack opens more easily with values around 20% of the maximum load.

Influence of the in-plane element size

In order to study the influence of the in-plane element size, a similar procedure to the previous one was carried out, but in addition to the use of elements with 16 µm, meshes with elements of 8 µm were also used in the refined zone. The curves were obtained for equal crack lengths, in this case, for Δa=384 µm, which corresponds to 24 propagations for 16-micron elements and 48 propagations for 8-micron elements.

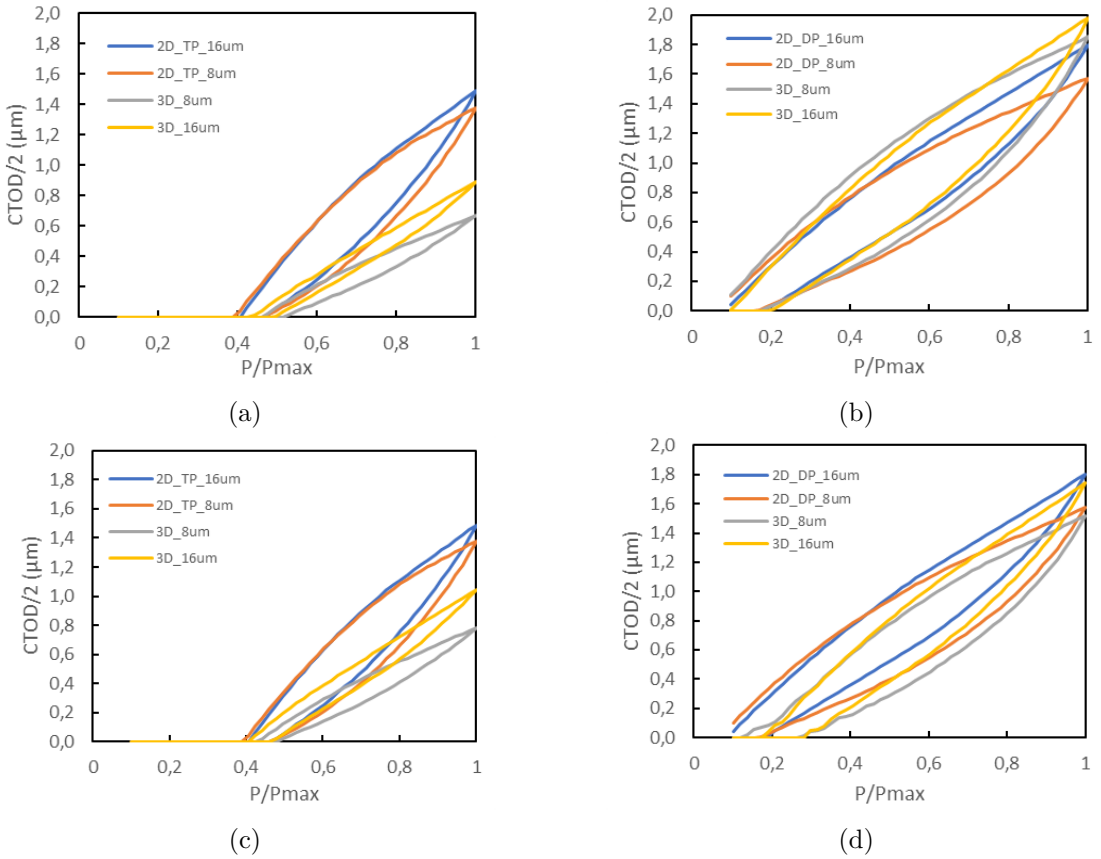

Figure 4.2: CTOD vs force for models with different elements size on the plane: (a) 3 mm model, at the surface; (b) 3 mm model, at half-thickness; (c) 1 mm model, at the surface; (d) 1 mm model, at half-thickness.

Figure 4.2 (a) shows the curves related to the 3 mm thick model, where the CTOD values at the specimen's surface are compared for two different element sizes, along with the plane stress state curves for the same meshes. When looking separately at the plane stress (TP) curves, it can be concluded that the element size has little influence on the results because the curves are close to each other. However, in the 3D curves at the surface, the differences are more considerable. When comparing the TP and 3D curves at the surface for the same mesh, a significant difference is observed, with the plane stress state curves always showing higher CTOD values.

Moving on to Figure 4.2 (b), it pertains to the same model, but the analysis focuses on the mid-thickness of the specimen, comparing it with the plane strain approach for both specified meshes. The difference between the plane strain (DP) curves for the two meshes is practically the same as the difference between the plane stress (TP) curves at the surface. Thus, the element size on the plane remains little influential in the results obtained for the two-dimensional models. As for the curves related to the 3D models, there is a slightly smaller difference compared to the curves at the surface, making the influence of the element size almost negligible. Comparing the 2D and 3D curves, the differences are much smaller in the mid-thickness compared to the surface. In the mid-thickness, the results tend to approach the plane strain (DP) curves, as expected,

whereas at the surface, it was expected that the results would be even closer to the plane stress (TP) curves.

Then, in Figures 4.2 (c) and (d), the same approach was carried out, but instead of using a 3 mm thick model, a model with the same characteristics but with 1 mm thickness was used. Once again, the element size has little influence on the results for 2D approaches, both in TP and DP. Also the DP curves obtained for both 1 mm and 3 mm thick models are similar when comparing Figures 4.2 (d) and (b). Regarding the 3D curves, in the 3 mm model, there is a more considerable difference at the surface when compared to half-thickness, where the curves are closer together.

In the 1 mm specimen at the surface, as shown in figure 4.2 (c), comparing the 2D and 3D curves for both meshes, the differences remain significant, although slightly reduced compared to the 3 mm model. At half-thickness, as shown in figure 4.2 (d), the difference between the 3D curves is a bit smaller compared to those on the surface, figure 4.2 (c), but still slightly larger than the 3 mm model at half-thickness. In this latter case, for the same meshes, the DP and 3D curves are very close at half-thickness, with the difference between them being almost negligible. The simulations regarding the DP and 3D specimens at half thickness show that it was needed a lower load value to open the crack when comparing to the TP simulation and 3D models at the surface that needed more than twice the amount of the applied load. This means that the crack firstly opens at half thickness of the specimen.

Influence of the element size in thickness

The numerical model with 1 mm thickness and a mesh with elements of 16 µm in the refined area of the plane was the chosen one for studying the influence of the element size in thickness. From this model, a similar one was generated, but instead of having 20 finite elements throughout its full thickness, it contains 60 elements to enable a comparison between the obtained CTOD results, changing only the number of elements and, consequently, their size along the crack front.

The curves in Figure 4.3 (a) and (b) were obtained for the same crack length, in this case, for Δa=384 µm, corresponding to 24 crack propagations, for measurements taken at the specimen's surface and at half-thickness, respectively. On the other hand, the curves in Figure 4.3 (c) and (d) are related to a crack propagation of Δa=784 µm, that is, 49 increments, at the surface and at half-thickness, respectively. The CTOD curves obtained at the surface are compared with the curve achieved through the 2D model under plane stress conditions, while the curves at half-thickness of the specimen were plotted with those corresponding to the plane strain condition.

For 24 crack increments, at the surface there is no influence of the element size in the thickness since the curves for 10 and 30 elements at half-thickness are overlapping. However, when comparing with the TP curve, notable differences are observed, with the CTOD values being significantly higher in the latter case, going towards what was seen previously. Continuing the analysis at the same crack propagation but focusing on what happens at half-thickness, besides the 3D model curves remaining almost coincident, there is also an approximation of these curves to the DP curve. In this case, although a higher force value is needed to open the crack in the 3D models, the maximum CTOD values are similar.

For 49 crack increments, the influence of the element size in the thickness increased as

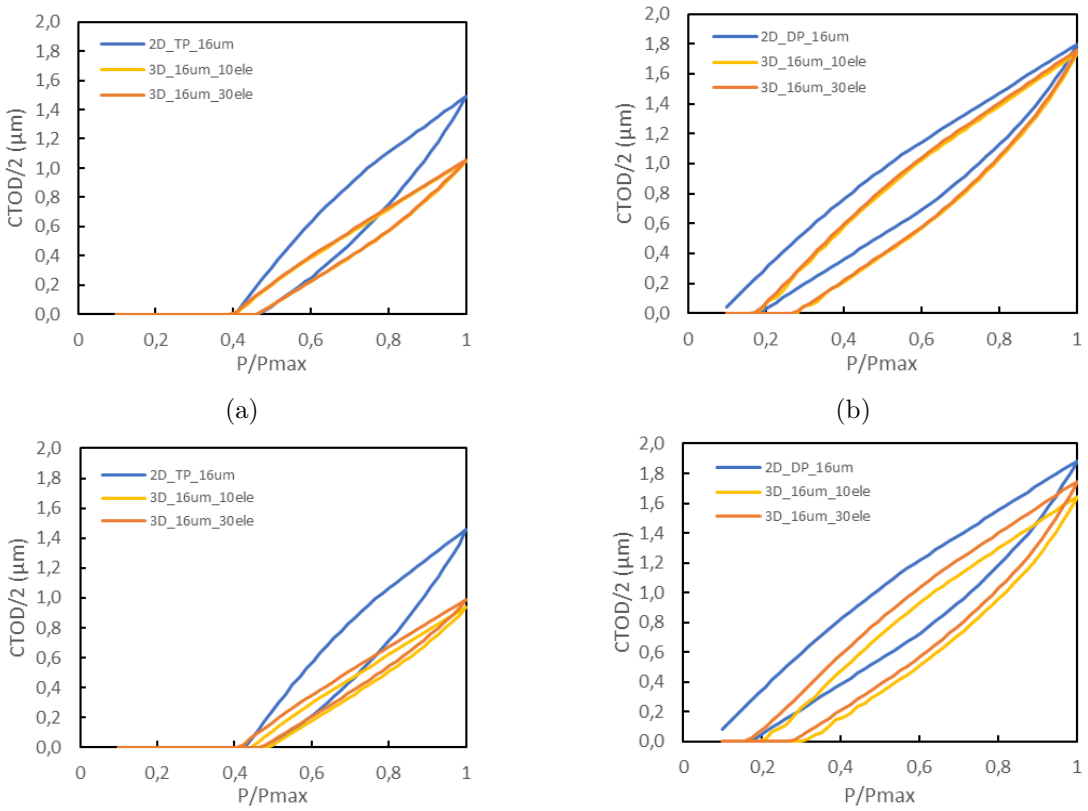

Figure 4.3: CTOD vs force for the 1 mm model with different elements size along the thickness: (a) Δa=384 µm, at the surface; (b) Δa=384 µm, at half-thickness; (c) Δa=784 µm, at the surface; (d) Δa=784 µm, at half-thickness.

both at the surface and at half-thickness the 3D curves no longer coincide and slightly deviate, also increasing the discrepancy with the 2D curves. In general, for a larger number of crack increments, the crack required higher force values to open, and the CTOD values slightly decreased.

4.1.2 P_{open} along the crack front

This section presents the results of P_{open} (crack opening load) along the crack front for the different numerical models, to evaluate the force required to open the crack. To keep the graphs consistent, the crack opening force was divided by the maximum applied load on the specimen for each model, while the distance of the node, for which the crack opening force was calculated, from the surface was divided by the corresponding value of the half-thickness of the respective numerical model.

The values of P_{open} were obtained using a macro from an Excel file [72]. This macro requires the CTOD vs. Force curve for each node under analysis as input and calculates important parameters such as the crack opening load, P_{open}. To evaluate this parameter through the thickness, its value was obtained for various nodes along the crack front. For models with larger thicknesses, such as 3 mm and 6 mm, nodes were considered

at intervals of 2 and 4, respectively, since the procedure had to be performed node by node individually, and in these cases, it was not necessary to use all nodes due to computational efficiency considerations.

Influence of the specimen's thickness

First of all, the influence of the specimen's thickness on P_{open} along the crack front was studied. For this purpose, five 3D models with different thicknesses and two 2D models were used. The two-dimensional models considered a plane stress state and a plane strain state. In these two-dimensional models, the value of the opening load is assumed to be constant along the crack front.

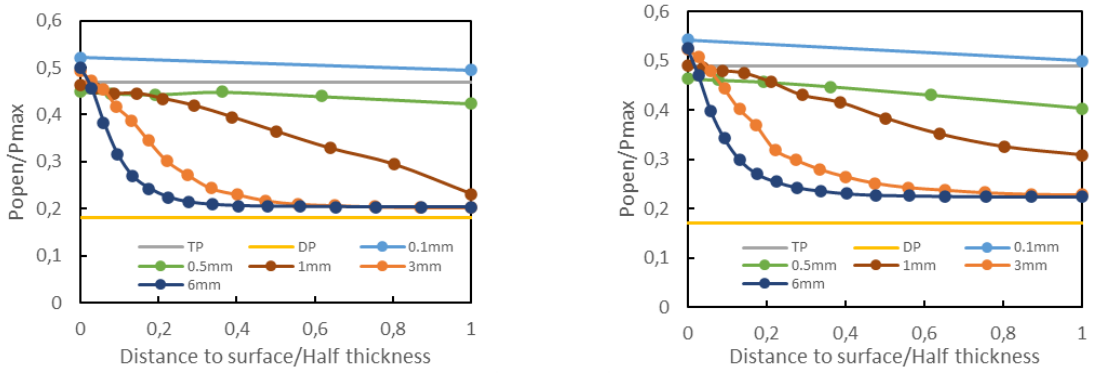

Figure 4.4: P_{open} along the crack front for models with different thicknesses: (a) Δa=384 µm; (b) Δa=784 µm.

In Figure 4.4, the graphs presented show the relationship between P_{open} and the distance to the specimen's surface for models with varying thickness. It is worth noting that all numerical models evaluated in this figure have a mesh with elements of 16 µm in the refined zone on the plane, along the crack propagation region. Figure 4.4 (a) and (b) refer to propagation 24 and 49, respectively. The only difference between (a) and (b) is the crack advance, Δa. It was expected that the TP and DP lines would represent the upper and lower limits of the graphs, respectively, because TP is generally assumed for small thickness models while DP for large thicknesses. However, the line representing the model with the smallest thickness (0.1 mm) reaches higher values than the TP line for both propagations. Additionally, several curves at the surface exceed the value of P_{open} obtained through the simulation in plane stress. Despite the aforementioned, the curves tend to approach the DP line along the thickness, while at the surface, the values are around the TP line, as anticipated. Thus, the crack requires values near 50% of the maximum load to open at the surface, and this value decreases as we move towards the interior of the specimen until only 20% to 30% of the total load is needed to open the crack at half the thickness, in the case of thicker numerical models. This behaviour can be observed for both crack advances (Δa=384 µm; Δa=784 µm), as the curves follow the same pattern, differing slightly only in the obtained values. As the thickness increases, the curve tend to converge more quickly to values close to the DP line. On the other hand, as the models' thickness decreases, the curves approach the TP line, where the

P_{open} values tend to form straight lines.

After analysing Figure 4.4, it was concluded that although the results are acceptable and generally consistent with expectations, the type of integration could have an influence, especially on models with smaller thickness. Considering the numerical model with 0.1 mm, it contains only one element in its thickness. When using reduced integration, there is only one integration point to represent the behaviour of the entire element, which is at the centre of the element. This can lead to less accurate results since the geometry of the hexahedral element should be very slender (one dimension is much larger than the others) and what happens in the center of the element isn't exactly the same as in the rest of the element. To address this, it was decided to conduct the same study but this time using full integration in all numerical models and the procedure was repeated with this modification.

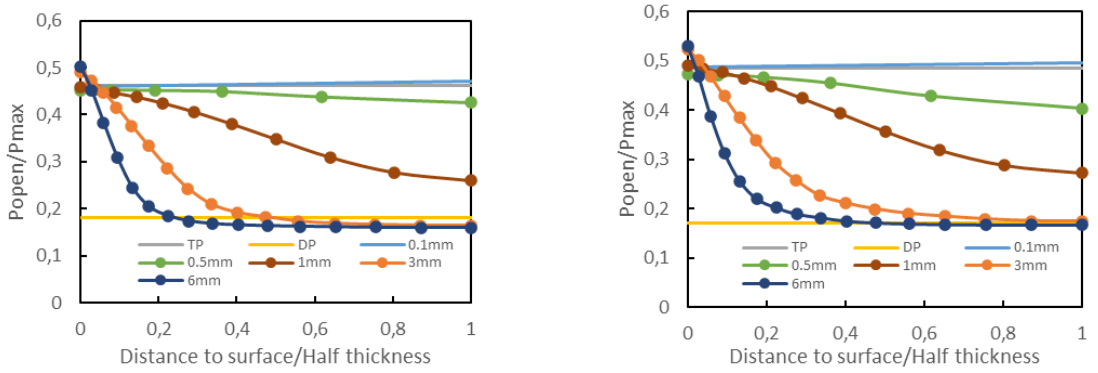

Figure 4.5: P_{open} along the crack front for models with different thicknesses, considering full integration: (a) Δa=384 µm; (b) Δa=784 µm.

Therefore, the graphs presented in Figure 4.5 show the relationship between P_{open} and the distance to the specimen's surface for all models with different thicknesses, using a mesh composed by elements of 16 µm in the refined zone on the plane. Figure 4.5 (a) and (b) refer to propagation 24 and 49, respectively. Compared to the reduced integration, as shown in Figure 4.4, it is evident that the line corresponding to the 0.1 mm model has lowered and is now coinciding with the TP line. As for the other curves, at the surface, there are still values very close to the TP line, with some even exceeding it, particularly the ones for the 3 mm and 6 mm thickness. Once again, the curves tend to approach the DP line along the thickness, and this convergence happens more quickly with the increase of the specimen thickness. While in reduced integration, the DP line served as the lower limit of the graph, in full integration, the curves for the 3 mm and 6 mm models reach slightly lower values in propagation 24 and coincide with the DP line in propagation 49. It is important to note that it was decided to focus the analysis in the reduced integration models. All graphs and images presented hereafter were obtained from those models.

Influence of the in-plane element size

Next, it was important to understand whether the in-plane element size had influence on the opening of the crack. In contrast to Figure 4.4, where the analysis was only conducted for models with 16 µm elements in the refined region of crack propagation, now models with 8 µm elements in the mentioned zone are also considered. Therefore, the graphs presented in Figure 4.6 show the obtained results for a numerical model with 3 mm thickness, and the analysis was focused on a propagation of Δa=384 µm, which corresponds to 24 increments of 16 µm elements and 48 increments of 8 µm elements.

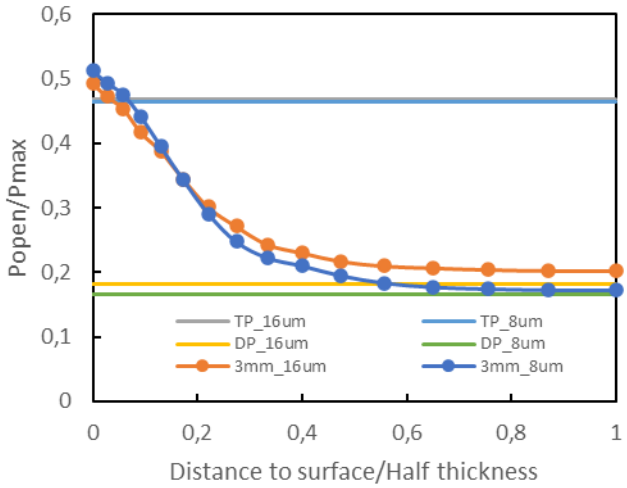

Figure 4.6: Influence of the size of the element in the plane on the P_{open} along the crack front.

The differences between P_{open} for 8 and 16-micron elements in the plane are basically negligible in the two-dimensional cases. Regarding the results of the 3D models, in regions close to the surface, the P_{open} values are similar to the TP, and as the analysis goes deeper into the thickness, the P_{open} values tend towards the DP. Now, comparing the curves related to the 3 mm thick models, it is possible to conclude that the size of the element in the plane does have some influence, even though the curves are almost overlapping initially, they start to deviate as the analysis progresses through the thickness. When comparing 2D *vs* 3D (16 µm) with 2D *vs* 3D (8 µm), it is clear that the 3D curve approaches the DP much better in the 8 µm case. However, close to the surface, this no longer happens.

Influence of the element size in thickness

In addition to the size of the element in the plane, another parameter that may influence the crack opening load is the size of the element in the thickness direction. To perform this analysis, two very similar numerical models with 1 mm thickness were used, where the only variable was the number of elements in the thickness direction and, consequently, their size.

Figure 4.7 represents, for the same in-plane element size (16 µm) and the same number of propagations (24), the relationship between P_{open} and the distance to the

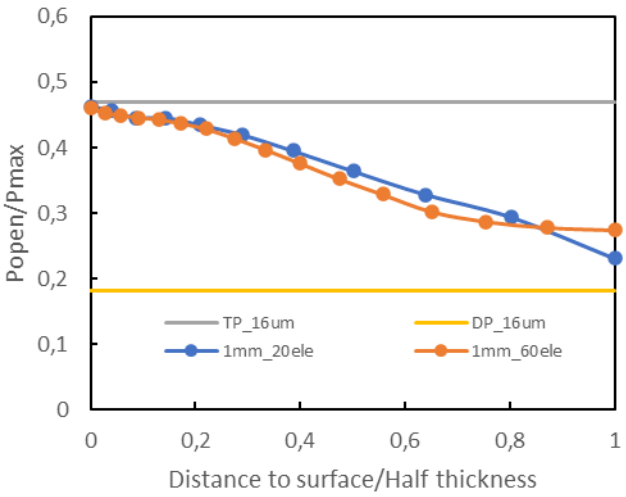

Figure 4.7: Influence of the size of the element in thickness on the P_{open} along the crack front.

surface of two 3D models. One contains 20 elements along a total thickness of 1 mm, while the other consists of 60 elements along the same 1 mm thickness. In addition to the comparison between these two 3D models, the figure includes values for the 2D models of plane stress and plane strain for the same propagation and in-plane element size as the previous ones.

As predicted, the curves related to the 3D models have the upper and lower limits represented by the TP and DP lines, respectively, approaching the plane stress state at the surface and the plane strain state at half-thickness of the specimen.

It is possible to conclude that tripling the number of elements in thickness only has some influence on zones near the half-thickness. At the surface and close to it, the curves are practically coincident. One possible reason for these results may be related to the bias ratio of 5 used in the construction of the mesh in all numerical models. This consists of higher refinement in regions near the specimen's surface and the elements increase in size along the thickness.

4.1.3 Plastic zones

FCG is related to nonlinear and irreversible phenomena at the crack tip, such as plastic deformation. Therefore, in this subchapter the critical zones of the specimen are presented, where there was crack propagation and consequently plastic deformation.

Figure 4.8 represents the plastically deformed zones, which are constituted by 8 µm elements, corresponding to a propagation of Δa=384 µm. Figure 4.8 (a) and (b) correspond to the plane stress state and plane strain state, respectively. On the other hand, Figure 4.8 (c) and (d) correspond to the 3D numerical model with a thickness of 1 mm, at the surface and half-thickness of the specimen, respectively. Figures 4.8 (e) and (f) represent the model with 3 mm thickness at the surface and half-thickness, respectively. Finally, Figure 4.8 (g) and (h) correspond to the plastically deformed zones at the crack front for the 1 mm and 3 mm thick specimens, respectively. In the Annex A, you can find the figures related to the models containing 16-micron elements in the crack

propagation zone, corresponding to 24 propagations, which is equivalent to Δa=384 µm.

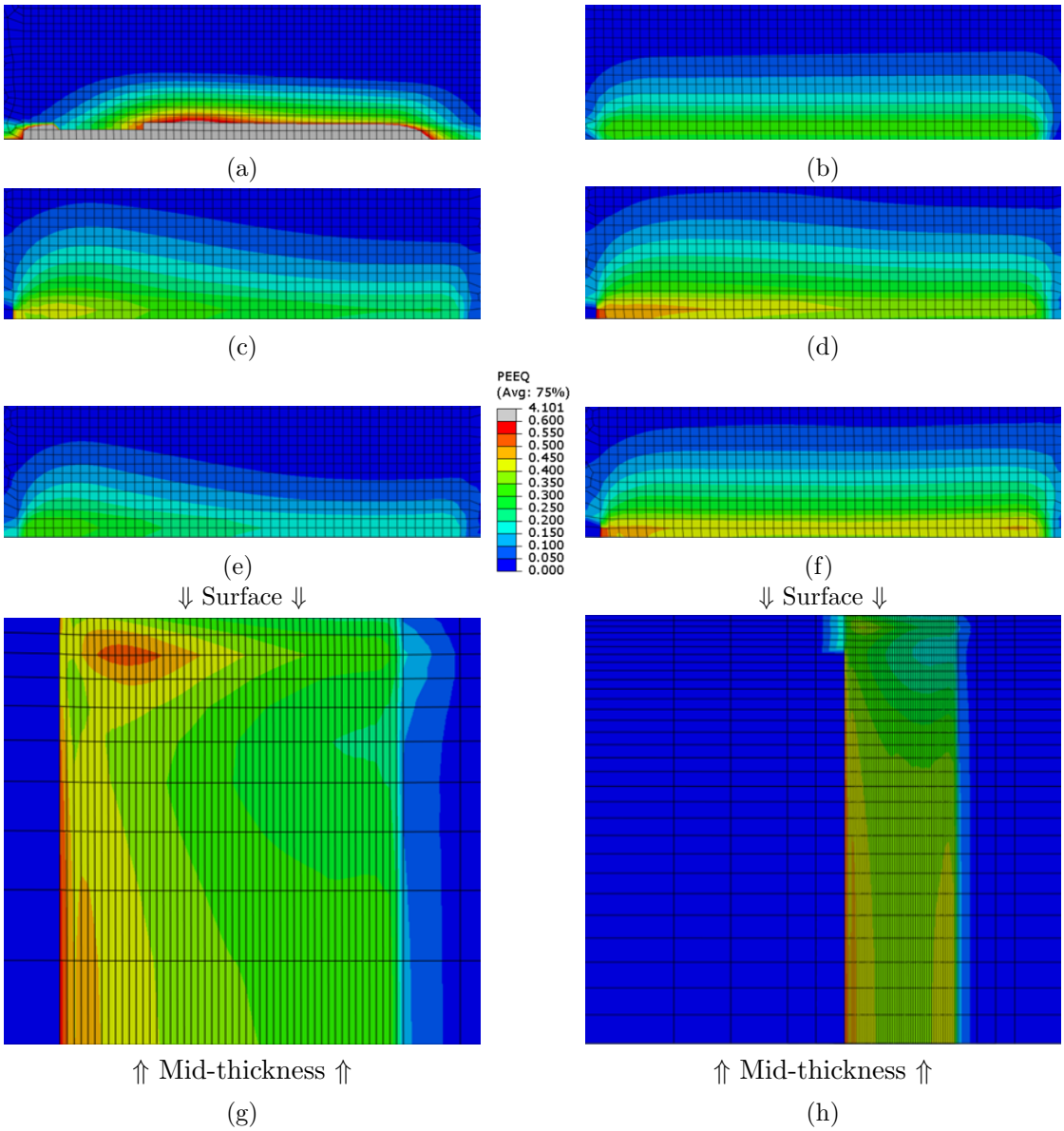

Figure 4.8: Plastic zones at minimum load for: (a) Plane stress state; (b) Plane strain state; (c) 1 mm model at the surface; (d) 1 mm model at mid-thickness; (e) 3 mm model at the surface; (f) 3 mm model at mid-thickness; (g) 1 mm model along the crack front; (h) 3 mm model along the crack front.

In general, the size of the plastic zone is similar in the plane strain state compared to the plane stress state. However, the plastic strain values reached in TP were much higher than in DP and all other models at the surface, for a significant portion of the deformed zone. While the maximum value of PEEQ (equivalent plastic strain) was around 0.4 in DP, it exceeded 4 in TP, making it ten times higher. A scale with a maximum limit of 0.6 was used, and only the TP model surpassed this value by a significant margin. The elements that exceeded this limit are represented in grey in Figure 4.8 (a). Plane

strain state is associated with a triaxial stress state, in which the occurrence of plastic deformation is relatively small when compared to a plane stress state.

Comparing Figure 4.8 (c) and (e), it can be concluded that the plastic zone at the surface is larger in the 1 mm thick numerical model than in the 3 mm thick one, suggesting that the thinner the model's thickness, the larger the plastic zone at the surface. As for the PEEQ values, the difference between them is very low, with only a slightly higher value being reached in the 1 mm thick specimen in the initial propagation zone. At half-thickness, in Figure 4.8 (d) and (f), once again, the differences in plastic strain values are practically negligible, and the plastically deformed zones are also very similar, although slightly larger in the 1 mm thick model. When comparing the plastic deformation at the surface with that at half-thickness for the same model, i.e., Figure 4.8 (c) with (d) and Figure 4.8 (e) with (f), it is observed in both models that the plastically deformed zone is relatively larger at half-thickness, along with higher values of plastic strain achieved in that zone. Along the crack front, in Figure 4.8 (g) and (h), the pattern of plastic deformation is very similar between both models. In the 1 mm thick specimen, slightly higher values of plastic strain are reached in the initial propagation zones at the surface, as previously observed in Figure 4.8 (c) and (e). Furthermore, the PEEQ gradient along the thickness is greater in the 1 mm thick model.

4.1.4 Crack profile

In order to evaluate the crack closure, this section presents the crack profiles obtained at minimum load for a propagation of Δa=384 µm. To do so, the Y-coordinate of the nodes along the crack was obtained, as well as their X-coordinate. The vertical displacement of the nodes (U2) corresponds to their Y-coordinate, since they were located on the Y=0 plane initially. In Figure 4.9, the crack profiles are shown at the surface and half-thickness of the 3D models, as well as the crack profile in the 2D models. Figure 4.9 (a) and (b) correspond to specimens with thicknesses of 1 mm and 3 mm, respectively, while Figure 4.9 (c) presents the crack profile for both plane stress state and plane strain state. These figures are representative of numerical models with 8-micron elements in the crack propagation zone. For the 1 mm specimen, the crack is completely closed at the surface, and at half thickness, it has a small opening only in the initial and final propagation zones, [36.5, 36.6] and [36.8, 36.9], respectively . As for the 3 mm specimen, the crack profile is similar: at the surface, the closure is total; however, at half thickness it opened up more along the entire propagation zone. The maximum vertical displacement value slightly increased and is about 16 times smaller than the size of the element in the plane, 8-micron. In plane stress state, as on the surface of 3D models, total crack closure occurs. This phenomenon can be observed on the CTOD curves of the 8-micron elements models in Figure 4.2 (a) and (c). The increase in plastic deformation in the plane stress state promotes a growth in crack closure induced by plastic deformation, as evidenced by Figure 4.9 (c). On the other hand, under a plane strain state there is no crack closure, and this is where a maximum crack opening is reached, approximately 0.8 microns.

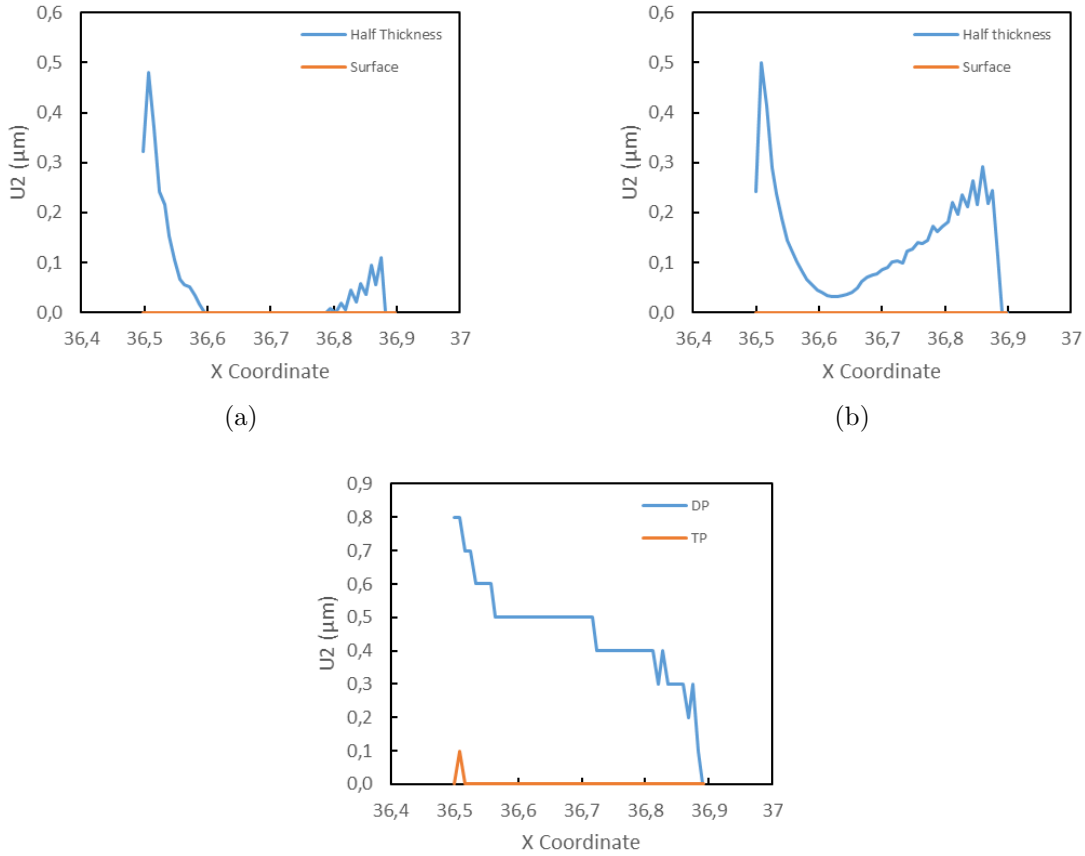

Figure 4.9: Crack profile along the refined crack propagation zone at minimum load: (a) 1 mm model; (b) 3 mm model; (c) Plane stress state (TP), and plane strain state (DP).

4.1.5 Influence of the crack propagation rate on the CTOD

In this section, initially, the influence of the in-plane element size on CTOD is studied assuming a constant crack growth rate (16 µm per propagation). Then, the CTOD curves were compared for different crack growth rates. For this purpose, two numerical models with a thickness of 1 mm were used. The first model had 16-micron elements in the plane, and after every two loading cycles, a set of nodes was released along the crack front. This model had already been studied in a previous part of this work. The second model contains elements with 8-micron in-plane size. After every two loading cycles, the two consecutive sets of nodes that are immediately behind the crack tip are simultaneously released along the crack front. In this way, both specified models exhibit the same crack growth rate, corresponding to 16 microns after every two loading cycles.

The objective of this approach is to compare meshes with 8-micron elements *versus* 16-micron elements for the same crack growth rate. Previously, the comparison was made between 8-micron and 16-micron elements, but with different propagation rates. By doing this, it will be possible to determine whether simulating 8-micron elements, releasing 2 sets of nodes at a time, is similar (or not) to simulating 16-micron elements,

releasing 1 set of nodes at a time, in terms of crack propagation behaviour.

In Figure 4.10 (a), the curves are shown representing the relationship between CTOD and the applied load for the conditions mentioned above, considering both the surface and mid-thickness of the 1 mm specimens. In Figure 4.10 (b), the curves representing the crack opening load relative to the distance from the specimen's surface are shown for the two cases (release of one set of nodes and release of two consecutive sets of nodes behind the crack tip).

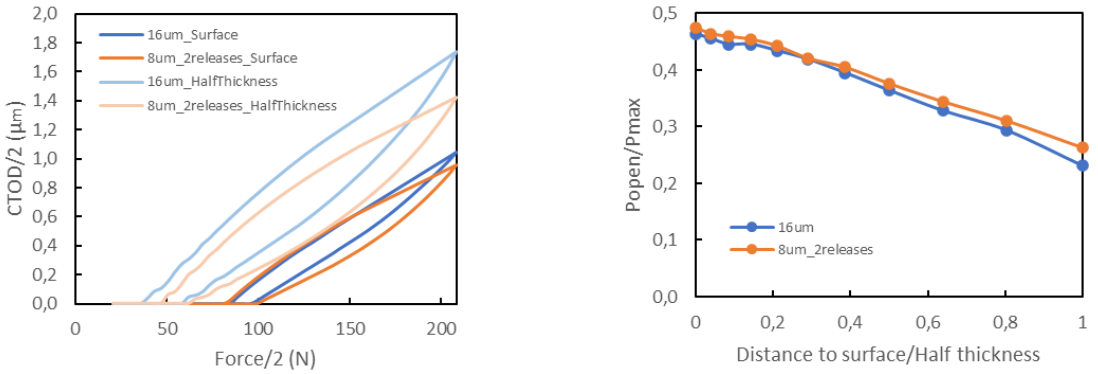

(a) (b)

Figure 4.10: Influence of the crack propagation rate: (a) CTOD *vs* force; (b) P_{open} *vs* distance to surface.

For the mesh with 8-micron elements, the CTOD was measured at the 2^{nd} node behind the crack tip to make it more comparable to the 16-micron case. This was done because the distance from the 1^{st} node to the crack tip corresponds to half of a 16-micron element. By measuring the CTOD at this specific node, the comparison between the two cases becomes more consistent despite using different element sizes.

It is noticeable that at the specimen's surface, the CTOD curves are close to each other, although the model with 16-micron elements achieves a slightly higher value. However, at mid-thickness, the curves diverge more, with the curve relative to the model with 16-micron elements always positioned above the other. The difference between the maximum CTOD values at half thickness is more than 3 times greater than the difference between the maximum CTOD values at the surface, indicating a greater discrepancy between the approaches at half thickness. Consequently, it can be concluded that there is higher sensitivity to the finite element mesh as we progress towards the interior of the specimen.

In terms of closure (P_{open}), the results are very similar. Once again, there is a closer alignment of the curves at the surface, where approximately 50% of the total load was required to open the crack. Although they are almost coincident, the curves slightly diverge as they approach the mid-thickness of the model, where the crack of the model with 8-micron elements opened later.

After conducting the previous study, another relevant aspect emerged for analysis, which concerns the position of the CTOD measurement point and its potential influence on the desired results. The same numerical models used in the previous approach were employed, with the only difference being in the CTOD measurement, which was measured at the 1^{st} node behind the crack tip in the specimen with 8-micron elements,

in this case. By doing this, a comparison can be made between measuring at 1 or 2 nodes behind the crack tip, allowing conclusions to be drawn regarding the influence of the measurement point's position on the CTOD results. This analysis will provide insights into how the location of CTOD measurement can impact the interpretation of the results obtained.

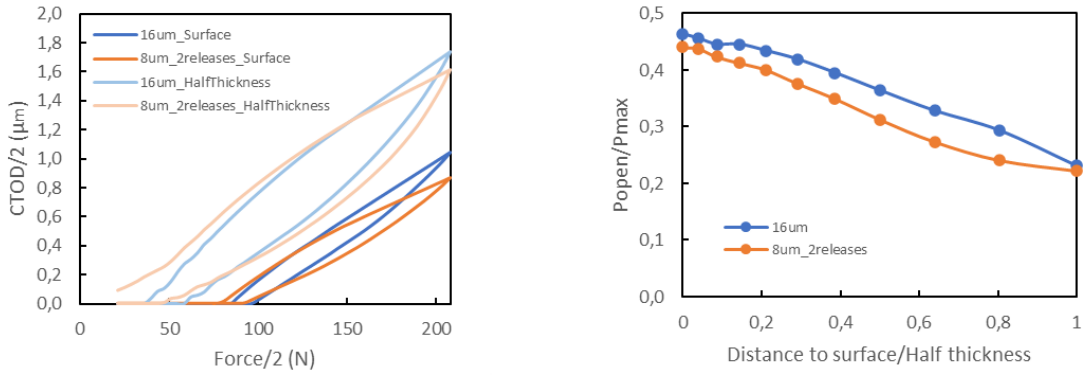

(a) (b)

Figure 4.11: Influence of the crack propagation rate considering a different CTOD measurement point: (a) CTOD *vs* force; (b) P_{open} *vs* distance to surface.

In Figure 4.11 (a), the curves are shown representing the relationship between CTOD and the applied load for the conditions mentioned above, considering once again the surface and mid-thickness of the 1 mm specimens. In Figure 4.11 (b), the curves representing the opening load of the crack relative to the distance from the specimen's surface are shown for the two situations. In this case, compared to the previous study, despite the CTOD curves reaching higher values for the model with 16-micron elements in the refined propagation zone, the difference between the maximum CTOD values increased at the surface and decreased at half thickness, resulting in an approximation of the curves.

In terms of P_{open}, the results show greater divergence between the two scenarios. The crack from the model with 16-micron elements needed higher load values to open along all the thickness. Compared to the previous approach, Figure 4.10 the curves related to CTOD measured at the surface also slightly deviate, while at half-thickness, they come closer. Therefore, we can conclude that the position of the CTOD measurement point greatly influences the results obtained at the P_{open} level.

4.2 Case study 2

This section is dedicated to the results obtained for case study 2 concerning a CT specimen of a titanium grade 2 alloy. For a specimen with a different geometry and material from the previous case study, we intend to compare the results obtained numerically, specifically CTOD *versus* load curves and plastic ΔCTOD as a function of the distance from the crack tip, with the experimental results provided by [71] under identical conditions.

Experimentally, the plastic ΔCTOD was measured at nodes located approximately 0.065 mm above (vertically) the symmetry plane because it is not possible to measure

the displacement precisely at the crack face, only in its vicinity. The first target point of study was located approximately 0.024 mm from the crack tip, and the subsequent measurement points were successively placed horizontally at the same distance from the previous one, as illustrated in Figure 4.12. In total, measurements were taken at eight points on the specimen, with the last measurement point situated approximately 0.192 mm from the crack tip.

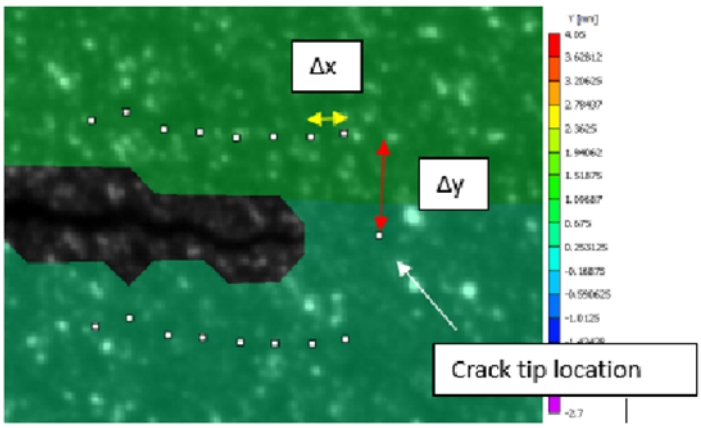

Figure 4.12: Experimental location of the crack tip and plastic ΔCTOD measurement points: Δx = 0.024 mm and Δy = 0.065 mm (from [71])

In order to closely approximate the numerical simulations to the experimental conditions, the CTOD was measured from the node located 0.024 mm horizontally and 0.064 mm vertically from the crack tip, which corresponds numerically to 8 elements of 8 microns vertically (9 nodes counted from the symmetry plane). In Figure 4.13, one of the numerical models of the specimen is represented, since all case study 2 models are equal in the plane . It contains a refined zone, marked with a black rectangle, with square elements of 8 microns side, where the crack propagation occurs. The red dots represent the nodes where the plastic ΔCTOD values were obtained, and the blue dot shows the crack tip location. A propagation rate of 1 micron per cycle was considered by the author of [71], which means, in the case of 8-micron elements, it corresponds to 8 cycles per propagation. However, experimentally, the number of cycles per propagation/propagation rate is not constant. The propagation depends on plastic deformation and, assuming plastic deformation controls FCG, only occurs when the regions surrounding the crack tip reach a critical plastic deformation value. This may require applying more or fewer load cycles compared to the numerical simulations performed. With that being said, the number of loading cycles per propagation might have a large influence on the results.

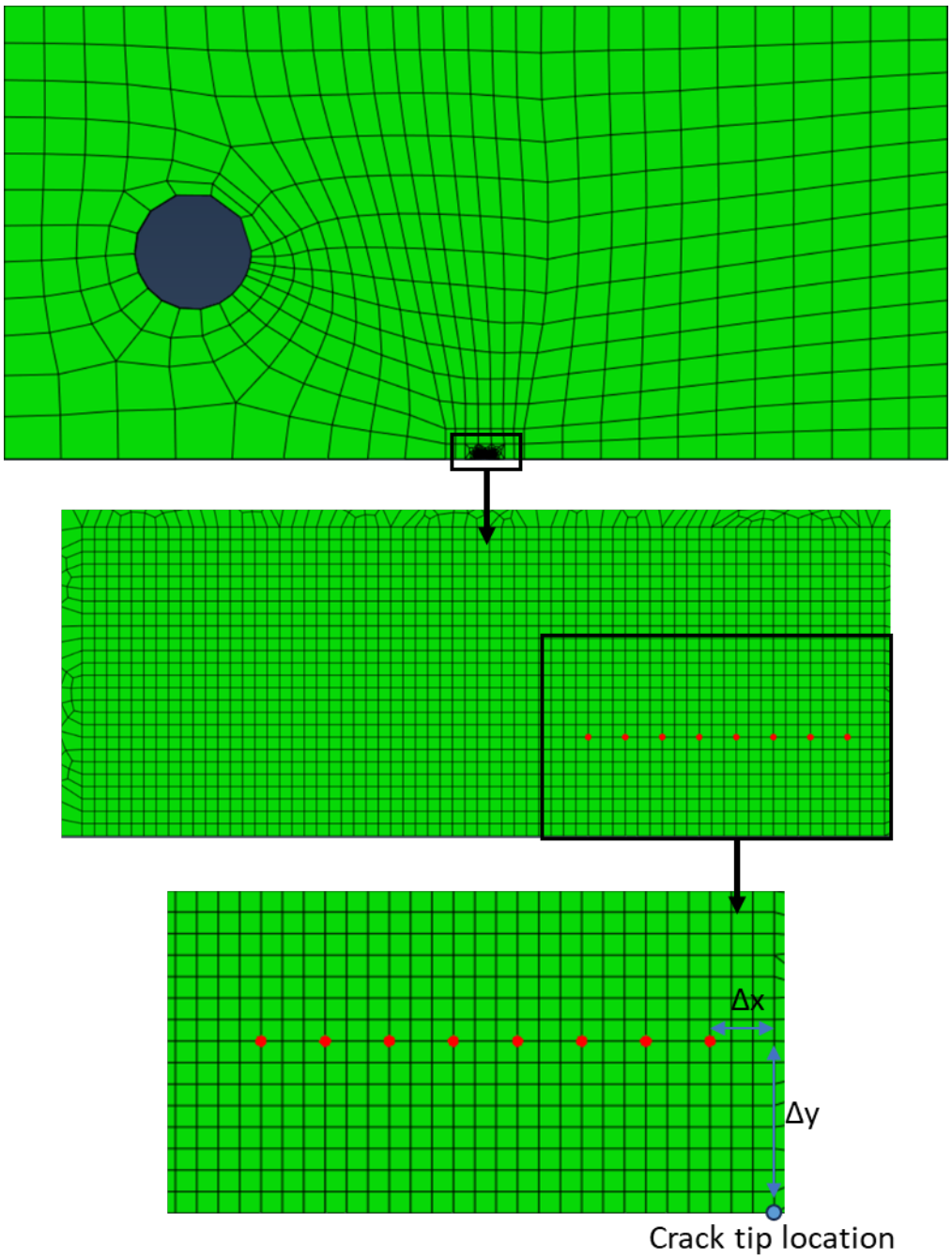

Figure 4.13: Numerical location of the crack tip and CTOD measurement points: Δx = 0.024 mm and Δy = 0.064 mm

4.2.1 Plastic ΔCTOD *vs* distance from the crack tip

In order to obtain the values of the plastic component of the CTOD, the Excel macro from [72] was used again, where the values of the CTOD and the applied load corresponding to the last load/unload cycle for the last propagation were inserted for each node studied. Figure 4.14 represents the curves of plastic ΔCTOD as a function

of the distance from the crack tip. Each curve consists of eight points where each point corresponds to a node analysed along the refined crack propagation zone. Three 3D numerical models were built, each having 0.1 mm, 0.3 mm, and 0.5 mm half thickness, all with 10 elements along the crack front. In addition to these, a 2D specimen was also modelled, where both plane strain and plane stress states were considered. However, no results were obtained when considering plane stress state since the analysis aborted early with convergence problems. It should be noted that the specimen that was used in the experimental tests by [71] had a total thickness of 1 mm and the results presented hereafter referring to "experimental" were provided by the author himself. It was decided to create models with smaller thicknesses in order to understand the influence of the thickness on the plastic ΔCTOD measurements at the surface, for the last propagation.

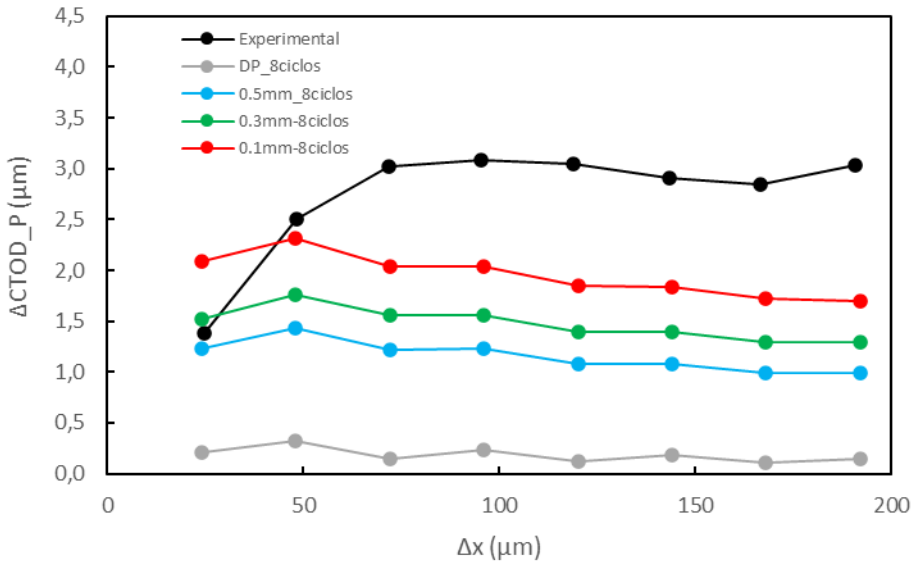

Figure 4.14: Plastic ΔCTOD *vs* distance from the crack tip for numerical models with eight load/unload cycles per propagation.

At the closest node to the crack tip, at 0.024 mm, the plastic ΔCTOD value of the 1 mm thick model is very close to the experimental value, as expected since they have the same thickness. However, the experimental plastic ΔCTOD curve shows significantly higher values compared to the numerical curves in most of the analysed nodes, increasing until approximately 0.096 mm from the crack tip and reaching a maximum plastic ΔCTOD value of around 3.1 µm. It slightly decreases only after this distance. On the other hand, the numerical curves reach their maximum value at 0.048 mm from the crack tip and then decrease as they move away from the crack tip. The DP curve represents an extreme case, being distant from all the other curves, mainly from the experimental one, and it consistently presents plastic ΔCTOD values below 0.5 µm.

A possible reason for such discrepancy of the curves may be due to the consideration of a constant propagation rate in the numerical models. In experimental conditions, crack propagation depends on plastic deformation, and the crack propagation rate is not constant. This means that more or fewer load cycles may be required compared to the numerical simulations performed. Following this, as a consequence of the results

obtained in Figure 4.14, it was decided to simulate the crack propagation for the same models, keeping all conditions the same except for the number of load/unload cycles per propagation, which was reduced to two, as in the case of study 1. To make these changes, it was necessary to adapt the Python scripts provided in the Annex B. In Abaqus, the number of steps in the models is now four times smaller.

Figure 4.15 represents the plastic ΔCTOD curves as a function of the distance from the crack tip for the latest propagation, but this time corresponding to simulations in which two load/unload cycles per propagation were considered. The remaining procedure for obtaining the values was entirely similar to that of the previous figure, Figure 4.14.

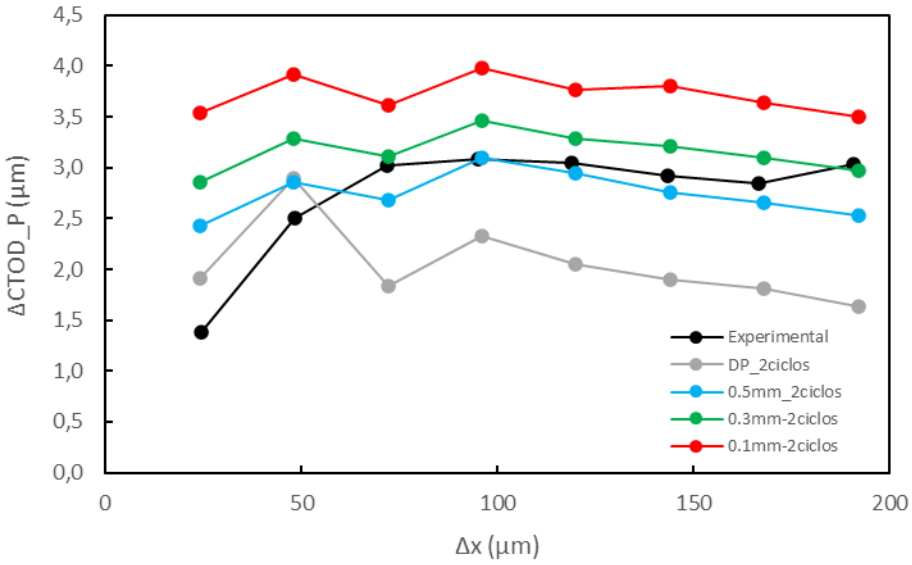

Figure 4.15: Plastic ΔCTOD at the surface *vs* distance from the crack tip for numerical models with two load/unload cycles per propagation.

Contrary to the previous figure, the experimental curve is no longer isolated from the numerical ones. The reduction of the number of load cycles resulted in a significant increase in the plastic ΔCTOD values for all numerical curves. At the nearest node to the crack tip, the curve corresponding to the DP simulation is the closest to the experimental one, while for the remaining points, the curves of the 1 mm and 0.6 mm thickness models are more similar, especially the one from the 1 mm model, as expected. In general, a plane stress state has been assumed when working with thicknesses of 1 mm or less; however, it was not possible to simulate plane stress as the simulations aborted. It was expected that the results for a thickness of 1 mm would be closer to TP than DP. From the previous graph, we can also observe that as the models' thickness decreases, the plastic ΔCTOD values at the surface increase. Since DP is assumed for high thicknesses, it makes sense for the plastic ΔCTOD values obtained to be the lowest, just as it would be expected for the TP curve to reach the highest values.

4.2.2 CTOD *vs* force

In addition to the curves related to plastic ΔCTOD, the CTOD vs. force curves were plotted for each of the eight nodes under analysis in each of the numerical models

mentioned above. These curves were then compared with the corresponding curve from the respective and equidistant measured experimental point.

Figure 4.16 illustrates the comparison between the experimental and numerical CTOD curves for simulations in which eight load/unload cycles per propagation were considered. Figure 4.16 (a) represents the CTOD curves, both experimental and numerical (1 mm thickness model), for a distance of 0.024 mm from the crack tip, i.e. behind the CTL (crack tip location), while Figure 4.16 (b) represents the CTOD curves for a distance of 0.192 mm from the crack tip. On the other hand, Figure 4.16 (c) and (d) correspond to the 2D numerical model in a plane strain condition, for distances of 0.024 mm and 0.192 mm from the crack tip, respectively. In these last figures, the load was normalized by its maximum value since the models have different thicknesses, and consequently, the applied load was different. All the remaining graphs related to the other nodes, as well as for the other developed and studied models for obtaining the curves from Figure 4.14 and Figure 4.15, are available in the Annex C.

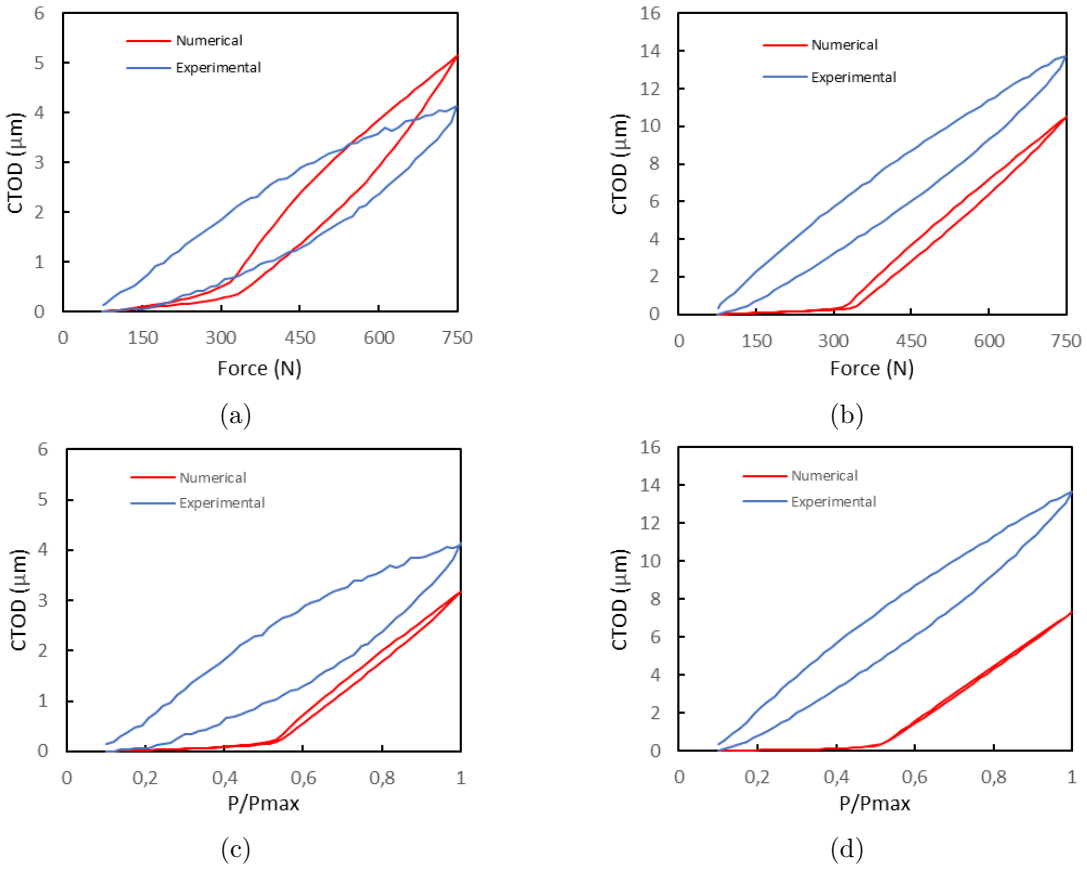

Figure 4.16: CTOD *vs* force for eight load/unload cycles per propagation: (a) 1 mm model at the surface, 0.024 mm behind the CTL; (b) 1 mm model at the surface, 0.192 mm behind the CTL; (c) Plane strain state at 0.024 mm behind the CTL; (d) Plane strain state at 0.192 mm behind the CTL.

In order to compare with the experimental results, the values of CTOD and force obtained through the simulations in Abaqus were multiplied by 2. This multiplication is necessary due to the symmetry conditions imposed. Since only half of the specimen

(or 1/4 in 3D cases) was modelled, both the vertical displacement obtained, and the applied force correspond to half of the actual values. Therefore, to maintain consistency, the comparison with the experimental results was conducted only after multiplying the numerical results by 2.

Analysing the graphs in Figure 4.16, it is evident that the numerical curves deviate significantly from the experimental ones. As shown in Figure 4.14, the values of plastic ΔCTOD are very low for both the 1 mm specimen and DP simulation. Only at the closest point to the crack tip (1^{st} point) the plastic ΔCTOD is very similar to the experimental one. This observation aligns with the CTOD curves, where a considerable discrepancy is observed between the numerical and experimental curves. Comparing the curves of the 1 mm model with the experimental one at the closest point to the crack tip, some proximity is noticed, especially for lower force values. Numerically, the crack opens later, but the maximum CTOD value surpasses the experimental value by about one micron, and the curve opening is substantial. However, for the farthest node, Figure 4.16 (b), the numerical curve exhibits very little opening, and the crack opens much later compared to the experimental curve. Regarding the curves related to the plane strain state (DP), the CTOD values are always lower, compared both to the experimental ones and to the 1 mm numerical model. The crack opens for higher force values, around 50% of the maximum applied load, whereas experimentally, the crack opens between 10% to 20% of the maximum load. In this case, the curve opening is extremely small, indicating almost non-existent plastic deformation. In general, there is an increase in the maximum CTOD for the farthest point from the crack tip in all curves. Experimentally, this increase is more than 3 times, while numerically, it is a little superior to 2 times.

For obtaining the curves shown in Figure 4.15, firstly it was necessary to obtain the CTOD vs. force curves corresponding to the simulations performed with two load/unload cycles per propagation.

Just like in the previous case, Figure 4.17 illustrates the comparison between experimental and numerical CTOD curves, where Figure 4.17 (a) represents the CTOD curves, experimental and from the numerical model with 1 mm thickness, at a distance of 0.024 mm from the crack tip, while Figure 4.17 (b) represents the CTOD curves at a distance of 0.192 mm from the crack tip. Figure 4.17 (c) and (d) refer to the two-dimensional model considering plane strain conditions, at distances of 0.024 mm and 0.192 mm from the crack tip, respectively. Once again, the graphs corresponding to the other analysed nodes for the different models are presented in the appendices. It is important to note that the only difference between Figure 4.16 and Figure 4.17 corresponds to the change in the number of load/unload cycles per propagation. In the first case, the crack required eight cycles of load/unload to advance 8 microns, while in the second case, it only needed two cycles.

Through the graphs in Figure 4.17, it is possible to notice that, concerning the graphs presented for 8 loading cycles per propagation, for the closest node to the crack tip, the numerical curves further deviate from the experimental ones, reaching significantly higher CTOD values. As for the curves related to the farthest analysis point, the numerical curves approach the experimental ones, and the CTOD values reached are similar. Looking at the curves of the 1 mm thick model, the crack opening load is relatively close to the experimental one, especially at the first analysed node, whereas for the last node, the crack opens slightly earlier experimentally.

Regarding the CTOD values, in the first case, numerical values are much higher than

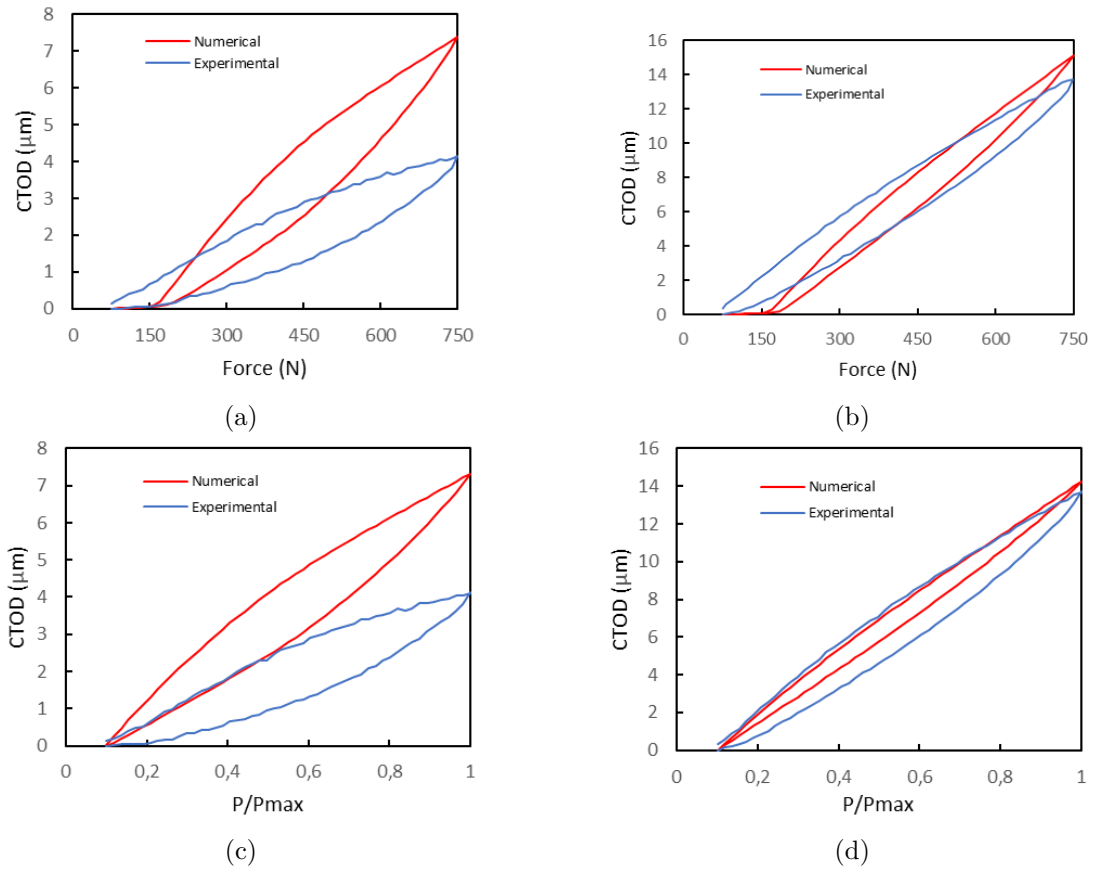

Figure 4.17: CTOD *vs* force for two load/unload cycles per propagation: (a) 1 mm model at the surface, 0.024 mm behind the CTL; (b) 1 mm model at the surface, 0.192 mm behind the CTL; (c) Plane strain state at 0.024 mm behind the CTL; (d) Plane strain state at 0.192 mm behind the CTL.

the experimental, while for the last measured node, the curves closely match, including their maximum value.

In the curves related to the plane strain state (DP), once again, there is a significant discrepancy with the experimental curves at the closest node to the edge of the crack. On the contrary, at the farthest node, there is an overall approximation of the curves, and both the crack opening load and the maximum CTOD value are extremely similar to the experimental. In this last case, the crack opens right at the minimum load.

Intentionally blank page.

Part III

Conclusion

Chapter 5

Conclusions and Recommendations for future research

Once the current dissertation is completed, it can be stated that the initially proposed objectives have been fulfilled.

Regarding Case Study 1, the following conclusions can be drawn:

- In plane stress state and at the surface of 3D models, the CTOD values are lower when comparing to plane strain state and at half-thickness of 3D models, which may be a consequence of the crack closure phenomenon that reduces the effective load range;
- The influence of the in-plane element size is almost negligible on the CTOD curves for 2D models and at half-thickness of the 3D specimens, but is more considerable at the surface. As expected, at the mid-thickness the results tend to approach the plane strain curves, whereas at the surface, it was expected that the results would be closer to the plane stress curves;
- There is no influence of the element size in thickness for 24 crack propagations both on the surface and in mid-thickness, but by increasing the number of crack increments the curves slightly deviate from each other;
- The specimen's thickness has a huge influence on the P_{open} results. As the model's thickness increases, the P_{open} curve tend to converge more quickly to values close to the DP line. On the other hand, as the models' thickness decreases, the curves approach the TP line, where the P_{open} values tend to form straight lines. The opening load is much higher at the surface and decreases significantly towards the interior of the specimen;
- The type of integration also has influence on the P_{open} curves, especially for lower thicknesses with less elements along the crack front;
- The influence of the in-plane element size on the P_{open} curves is negligible in the 2D models (TP and DP), but have some influence on 3D models. Althought

the curves are almost overlapping initially, they start to deviate as the analysis progresses through the thickness;

- The element size in thickness has no influence on P_{open} at the surface and close to it, while near the mid-thickness the P_{open} curves (regarding 20 elements and 60 elements along 1 mm thickness) separate. One possible reason can be related to the higher refinement in zones near the specimen's surface;

- The size of the plastic zone is slightly larger for thinner models while the differences in plastic strain values are practically negligible. The plastically deformed zones are relatively larger at half-thickness, along with higher values of plastic strain achieved throughout that zone;

- Plane stress state models presented total crack closure that may have been induced by a greater plastic deformation. On the other hand, there was no crack closure under plane strain state;

- In tridimensional models, the crack is completely closed at the surface and at half-thickness has a small opening, more visible in the initial and final propagation zones;

- After analysing two models with the same crack propagation rate but with 8 and 16 micron element size meshes, it can be concluded that there is higher sensitivity to the finite element mesh as we progress towards the interior of the specimen, both on the CTOD and P_{open} curves;

- The position of the CTOD measurement point greatly influences the results obtained at the P_{open} level.

With respect to Case Study 2, the subsequent conclusions can be taken:

- For eight load cycles per crack propagation there was a large discrepancy between the experimental and numerical plastic ΔCTOD curves that might be caused by the consideration of a constant propagation rate numerically;

- The reduction of the number of load cycles (from eight to two) resulted in a significant increase in the plastic ΔCTOD values for all numerical curves, resulting in an approximation of the numerical curves to the experimental one. In this case, the curve related to the 1 mm numerical model was the closest to the experimental as expected, since both have the same thickness;

- Regarding the CTOD vs force curves, for eight load cycles per crack increment the numerical curves deviate significantly from the experimental and are mostly below them. For two load cycles there is an increase of the CTOD values numerically. At the closest node to the crack tip, the numerical curves still deviate from the experimental but for the farthest analysis point the numerical curves approach the experimental ones, and the CTOD values reached are very similar.

For future works, it is proposed:

- Analyse the fatigue crack growth for the same conditions as case study 1, but with the use of a more realistic crack growth criterion, based on the accumulated plastic strain, $\Delta\varepsilon_p$;
- Create numerical models with different crack configurations, such as cracks with different curvatures along the crack's front;
- Study the influence of the crack's shape on the size of the superficial plastic zone and its relationship with the crack's length;
- Conduct an experimental procedure using physical specimens with different geometries and materials simultaneously with a similar numerical study for subsequent comparison of FCG.

Intentionally blank page.

Appendix A

Plastic zones

Figure A.1 represents the plastically deformed zones for models that are constituted by 16 µm elements on the crack growth zone, corresponding to 24 crack increments, i.e., a propagation of Δa=384 µm. Figure A.1 (a) and (b) correspond to the plane stress state and plane strain state, respectively. Figure A.1 (c) and (d) correspond to the 3D numerical model with a thickness of 1 mm, at the surface and half-thickness of the specimen, respectively. Figures A.1 (e) and (f) represent the model with 3 mm thickness at the surface and half-thickness, respectively. Finally, Figure A.1 (g) and (h) correspond to the plastically deformed zones at the crack front for the 1 mm and 3 mm thick specimens, respectively.

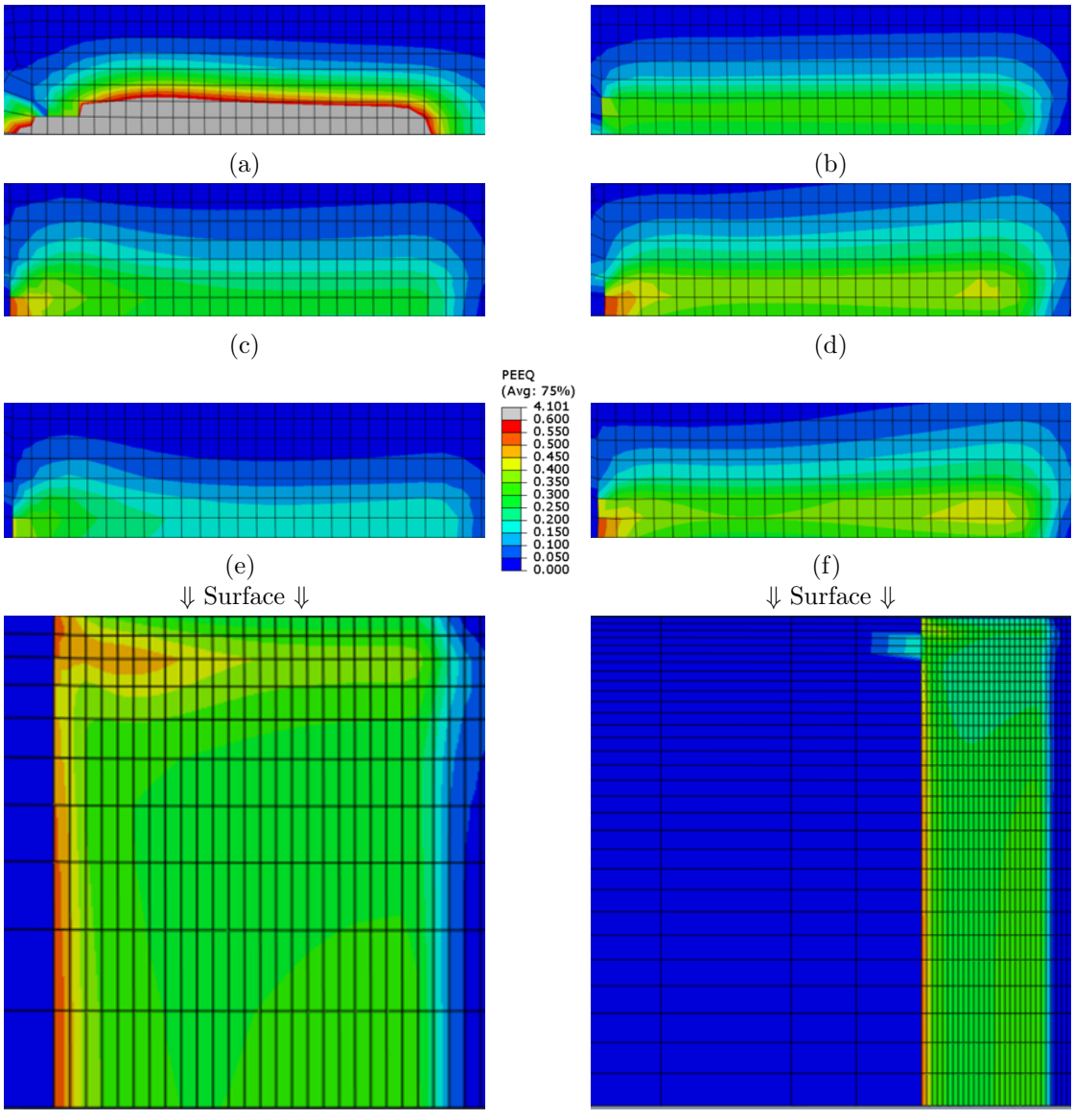

Figure A.1: Plastic zones at minimum load for: (a) Plane stress state; (b) Plane strain state; (c) 1 mm model at the surface; (d) 1 mm model at mid-thickness; (e) 3 mm model at the surface; (f) 3 mm model at mid-thickness; (g) 1 mm model along the crack front; (h) 3 mm model along the crack front.

Appendix B

Python scripts

In this section some of the python scripts used to automatize the model's creation on Abaqus are presented. There are a few notes initialized by "#" to explain parts of the code. Since each different model needed a code adaptation, below are only 3 different scripts that serve as examples. The first was created for 2D models and the refined zone contains 8-micron elements. The second was used in a 3D model with a thickness of 1 mm (total), for the same type of mesh. Finally, the code for a 1 mm model with 16-micron elements is presented.

2D – 8 µm

```
from abaqus import *
from abaqusConstants import *
import __main__
import section
import regionToolset
import displayGroupMdbToolset as dgm
import part
import material
import assembly
import step
import interaction
import load
import mesh
import optimization
import job
import sketch
import visualization
import xyPlot
import displayGroupOdbToolset as dgo
import connectorBehavior

#initial coordinates of the first node to be freed

xc = 36.5
```

```
yc = -15
zz = 0.0

#creation of steps

for i in range(1, 641):

#in the first step, a concentrated force "Load-1" of value cf2 will
be applied to the reference point located in the center of the hole;

    if i==1:
        step = "Step-" + str(i)
        mdb.models['Model-1'].StaticStep(name=step, previous='Initial',
        maxNumInc=10000, initialInc=0.01, minInc=0.01,
        maxInc=1.0, nlgeom=ON)
        a = mdb.models['Model-1'].rootAssembly
        r1 = a.referencePoints
        refPoints1=(r1[4], )
        region = a.Set(referencePoints=refPoints1, name='Set-3')
        mdb.models['Model-1'].ConcentratedForce(name='Load-1', createStepName=step,
        region=region, cf2=41.67, distributionType=UNIFORM,
        field='', localCsys=None)

#if the step is even, the loading will be subject to an amplitude,
in this case linearly decreasing (discharge);

    elif (i%2) == 0:
step = "Step-" + str(i)
p_step = "Step-" + str(i-1)
mdb.models['Model-1'].StaticStep(name=step, previous=p_step,
maxNumInc=10000, initialInc=0.01, minInc=0.01, maxInc=1.0, nlgeom=ON)
mdb.models['Model-1'].loads['Load-1'].setValuesInStep(stepName=step,
amplitude='Amp-3')

#if the step is even, and a multiple of 4, that is, every 4 steps a new set
will be created with 1 less node from the previous one,
where a new symmetry BC will be applied (freed node)
#and the anterior BC is deactivated;
#the selection of the intended nodes is done through a BoundingBox in
which the initial and final coordinates are selected and all the
nodes inside the box will be selected;
#then the starting point (xc) will progress by 0.008 which
corresponds to the size of an element in that zone;

if (i%4) == 0:

nsymm = "nSymm-" + str(i+1)
```

```
bcSymm = "bSymm" + str(i+1)
p_bcSymm = "bSymm" + str(i-3)
a = mdb.models['Model-1'].rootAssembly
n1 = a.instances['CT_2D-1'].nodes
nodes1 = n1.getByBoundingBox(((xc+0.008)-0.001),(yc),zz, (62.5 + 0.001),
(yc + 0.001), zz)
region = a.Set(nodes=nodes1, name = nsymm)
mdb.models['Model-1'].YsymmBC(name=bcSymm, createStepName=step, region = region,
localCsys = None)
xc = (xc + 0.008)
mdb.models['Model-1'].boundaryConditions[p_bcSymm].deactivate(step)

else:
continue

#if the step is odd, the loading will be subject to a linearly
increasing amplitude (load);

    else:
step = "Step-" + str(i)
p_step = "Step-" + str(i-1)
mdb.models['Model-1'].StaticStep(name=step, previous=p_step,
maxNumInc=10000, initialInc=0.01, minInc=0.01, maxInc=1.0, nlgeom=ON)

mdb.models['Model-1'].loads['Load-1'].setValuesInStep(stepName=step,
amplitude='Amp-2')
```

3D – 1 mm specimen – 8 µm

```
from abaqus import *
from abaqusConstants import *
import __main__
import section
import regionToolset
import displayGroupMdbToolset as dgm
import part
import material
import assembly
import step
import interaction
import load
import mesh
import optimization
import job
import sketch
import visualization
```

```
import xyPlot
import displayGroupOdbToolset as dgo
import connectorBehavior

#initial coordinates of the first node to be freed;
#for 3D models there will be a Z component aswell;

xc = 32.75
yc = 0
zz = 0.5

#creation of steps

for i in range(1, 201):

#same procedure as the 2D models, but different thicknesses require
different force values, cf2;

    if i==1:
        step = "Step-" + str(i)
        mdb.models['Model-1'].StaticStep(name=step, previous='Initial',
        maxNumInc=10000, initialInc=0.01, minInc=0.01,
        maxInc=1.0, nlgeom=ON)
        a = mdb.models['Model-1'].rootAssembly
        r1 = a.referencePoints
        refPoints1=(r1[8], )
        region = a.Set(referencePoints=refPoints1, name='m_Set-4')
        mdb.models['Model-1'].ConcentratedForce(name='Load-1', createStepName=step,
        region=region, cf2=208.35, distributionType=UNIFORM,
        field='', localCsys=None)


    elif (i%2) == 0:
step = "Step-" + str(i)
p_step = "Step-" + str(i-1)
mdb.models['Model-1'].StaticStep(name=step, previous=p_step,
maxNumInc=10000, initialInc=0.01, minInc=0.01, maxInc=1.0, nlgeom=ON)
mdb.models['Model-1'].loads['Load-1'].setValuesInStep(stepName=step,
amplitude='Amp-3')

#in these type of models, the BoundingBox will have a Z component to
catch the nodes along the thickness to apply the new BC;

if (i%4) == 0:
nsymm = "nSymm-" + str(i+1)
bcSymm = "bSymm" + str(i+1)
p_bcSymm = "bSymm" + str(i-3)
```

```
a = mdb.models['Model-1'].rootAssembly
n1 = a.instances['CT_3D-1'].nodes
nodes1 = n1.getByBoundingBox(((xc+0.008)-0.001),(yc),0, (58.75 + 0.001),
(yc + 0.001), (zz+0.001))
region = a.Set(nodes=nodes1, name = nsymm)
mdb.models['Model-1'].YsymmBC(name=bcSymm, createStepName=step, region = region,
localCsys = None)
xc = (xc + 0.008)
mdb.models['Model-1'].boundaryConditions[p_bcSymm].deactivate(step)

else:
continue

    else:
step = "Step-" + str(i)
p_step = "Step-" + str(i-1)
mdb.models['Model-1'].StaticStep(name=step, previous=p_step,
maxNumInc=10000, initialInc=0.01, minInc=0.01, maxInc=1.0, nlgeom=ON)
mdb.models['Model-1'].loads['Load-1'].setValuesInStep(stepName=step,
        amplitude='Amp-2')
```

3D – 1 mm specimen – 16 µm

```
from abaqus import *
from abaqusConstants import *
import __main__
import section
import regionToolset
import displayGroupMdbToolset as dgm
import part
import material
import assembly
import step
import interaction
import load
import mesh
import optimization
import job
import sketch
import visualization
import xyPlot
import displayGroupOdbToolset as dgo
import connectorBehavior


xc = 32.75
```

```
yc = 0
zz = 0.5


for i in range(1, 201):
    if i==1:
        step = "Step-" + str(i)
        mdb.models['Model-1'].StaticStep(name=step, previous='Initial',
        maxNumInc=10000, initialInc=0.01, minInc=0.01,
        maxInc=1.0, nlgeom=ON)
        a = mdb.models['Model-1'].rootAssembly
        r1 = a.referencePoints
        refPoints1=(r1[8], )
        region = a.Set(referencePoints=refPoints1, name='m_Set-4')
        mdb.models['Model-1'].ConcentratedForce(name='Load-1', createStepName=step,
        region=region, cf2=208.35, distributionType=UNIFORM,
        field='', localCsys=None)


    elif (i%2) == 0:
step = "Step-" + str(i)
p_step = "Step-" + str(i-1)
mdb.models['Model-1'].StaticStep(name=step, previous=p_step,
maxNumInc=10000, initialInc=0.01, minInc=0.01, maxInc=1.0, nlgeom=ON)
mdb.models['Model-1'].loads['Load-1'].setValuesInStep(stepName=step,
amplitude='Amp-3')

#for a mesh with 16 mícron elements, the only difference is the xc increment
for each new BC, which has to be 0.016 instead of 0.008

if (i%4) == 0:
nsymm = "nSymm-" + str(i+1)
bcSymm = "bSymm" + str(i+1)
p_bcSymm = "bSymm" + str(i-3)
a = mdb.models['Model-1'].rootAssembly
n1 = a.instances['CT_3D-1'].nodes
nodes1 = n1.getByBoundingBox(((xc+0.016)-0.001),(yc),0, (58.75 + 0.001),
(yc + 0.001), (zz+0.001))
region = a.Set(nodes=nodes1, name = nsymm)
mdb.models['Model-1'].YsymmBC(name=bcSymm, createStepName=step, region = region,
localCsys = None)
xc = (xc + 0.016)
mdb.models['Model-1'].boundaryConditions[p_bcSymm].deactivate(step)

else:
continue
```

```
    else:
step = "Step-" + str(i)
p_step = "Step-" + str(i-1)
mdb.models['Model-1'].StaticStep(name=step, previous=p_step,
maxNumInc=10000, initialInc=0.01, minInc=0.01, maxInc=1.0, nlgeom=ON)
mdb.models['Model-1'].loads['Load-1'].setValuesInStep(stepName=step,
        amplitude='Amp-2')
```

Intentionally blank page.

Appendix C

CTOD vs force (case study 2)

Figures C.1- C.8. illustrate all CTOD vs force curve for the case study 2 for each CTOD measurement point on the specimen's plane.

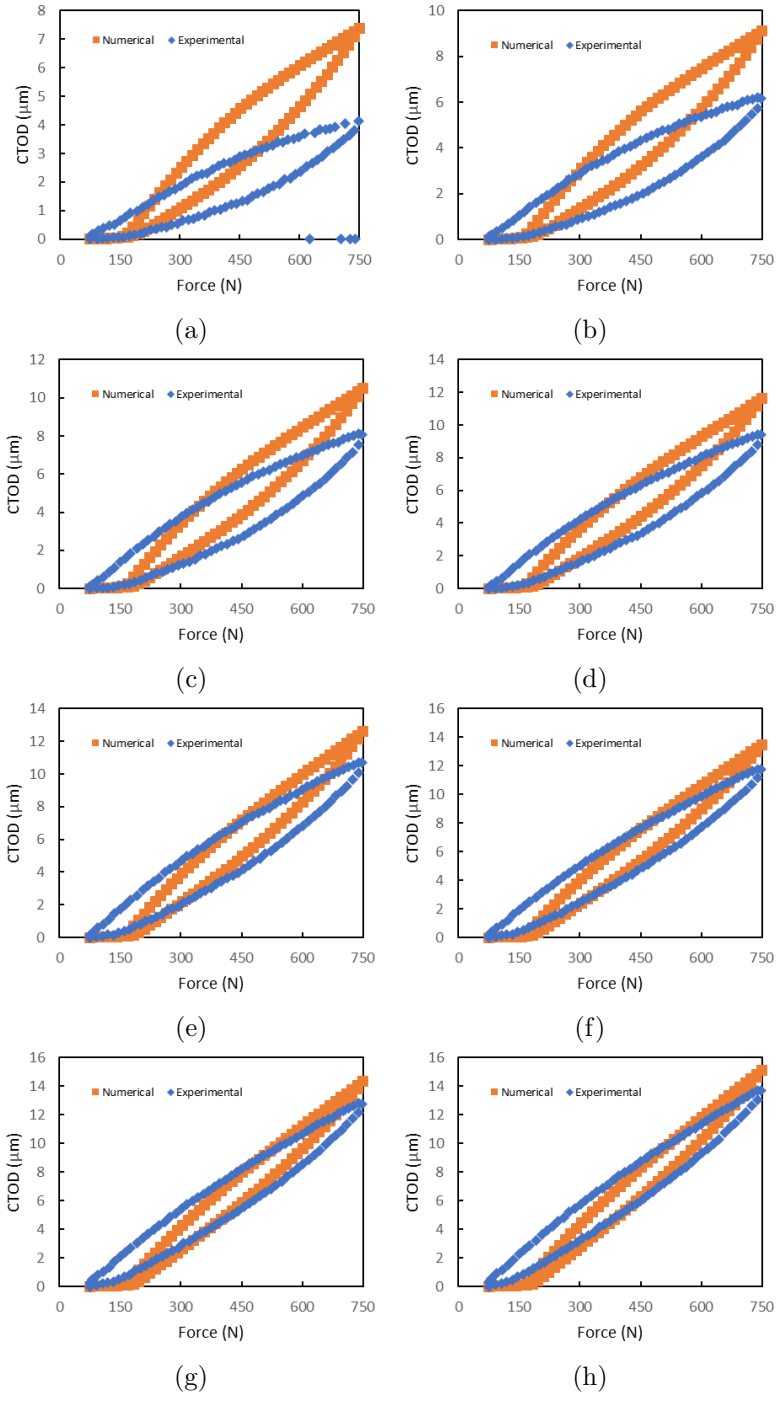

Figure C.1: CTOD vs force for two load/unload cycles per propagation for 1 mm model: (a) 0.024 mm behind the CTL; (b) 0.048 mm behind the CTL; (c) 0.072 mm behind the CTL; (d) 0.096 mm behind the CTL; (e) 0.120 mm behind the CTL; (f) 0.144 mm behind the CTL; (g) 0.168 mm behind the CTL; (h) 0.192 mm behind the CTL.

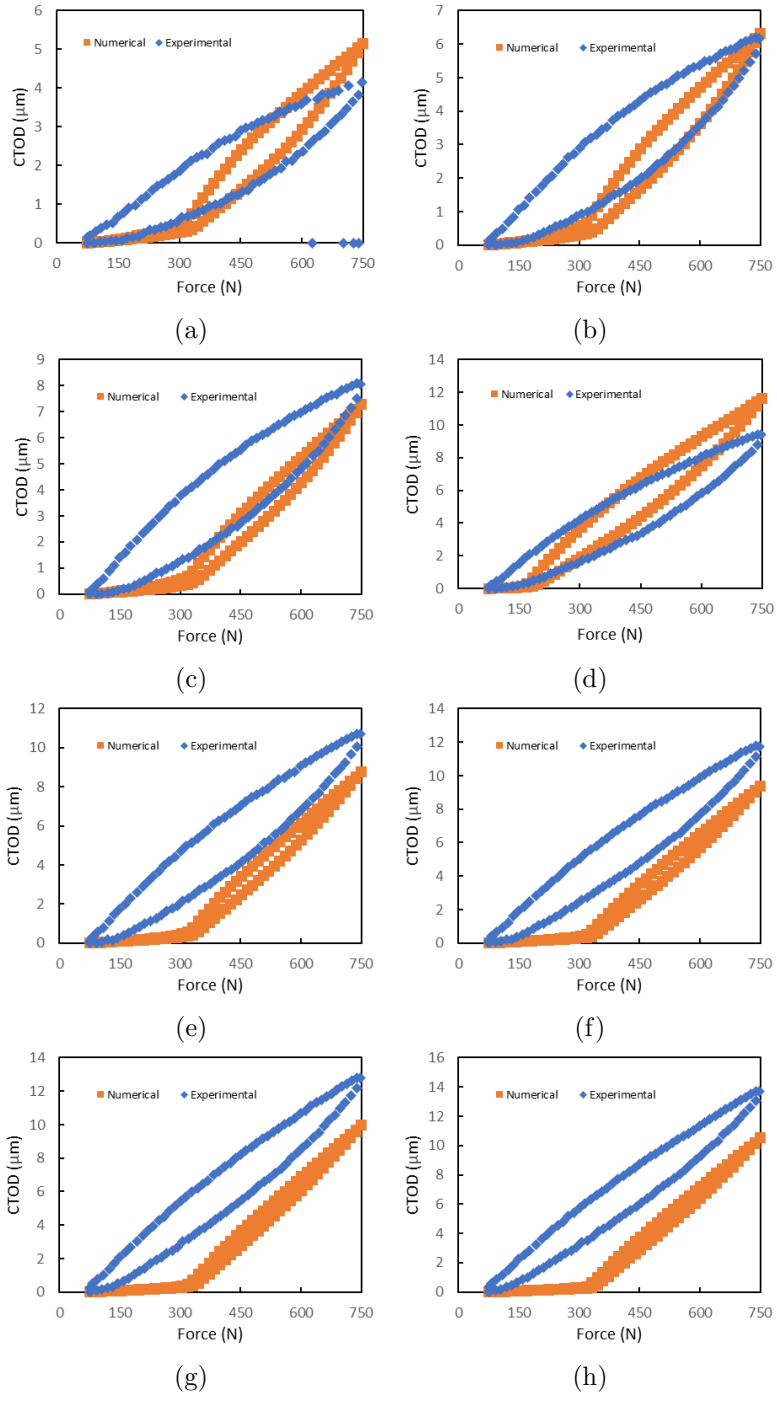

Figure C.2: CTOD vs force for eight load/unload cycles per propagation for 1 mm model: (a) 0.024 mm behind the CTL; (b) 0.048 mm behind the CTL; (c) 0.072 mm behind the CTL; (d) 0.096 mm behind the CTL; (e) 0.120 mm behind the CTL; (f) 0.144 mm behind the CTL; (g) 0.168 mm behind the CTL; (h) 0.192 mm behind the CTL.

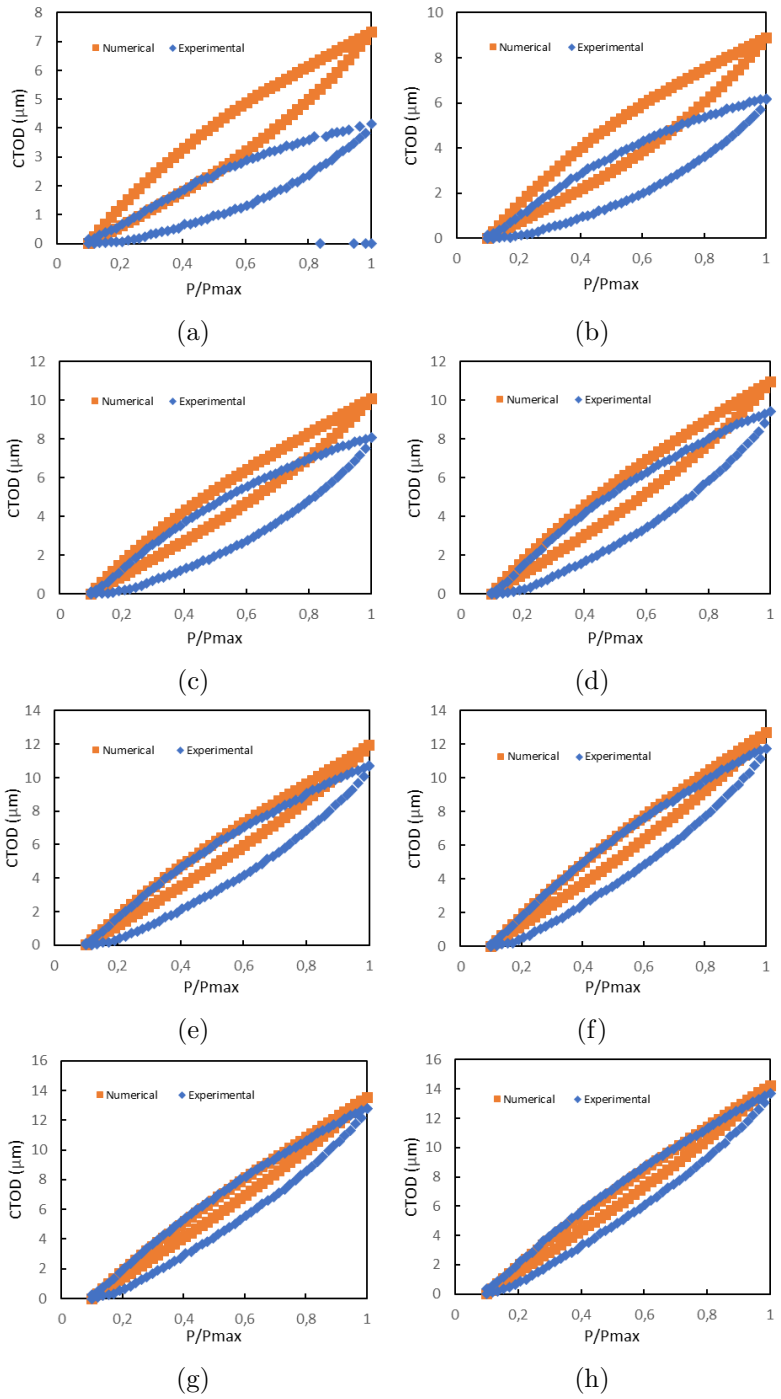

Figure C.3: CTOD vs force for two load/unload cycles per propagation for 2D plane strain model: (a) 0.024 mm behind the CTL; (b) 0.048 mm behind the CTL; (c) 0.072 mm behind the CTL; (d) 0.096 mm behind the CTL; (e) 0.120 mm behind the CTL; (f) 0.144 mm behind the CTL; (g) 0.168 mm behind the CTL; (h) 0.192 mm behind the CTL.

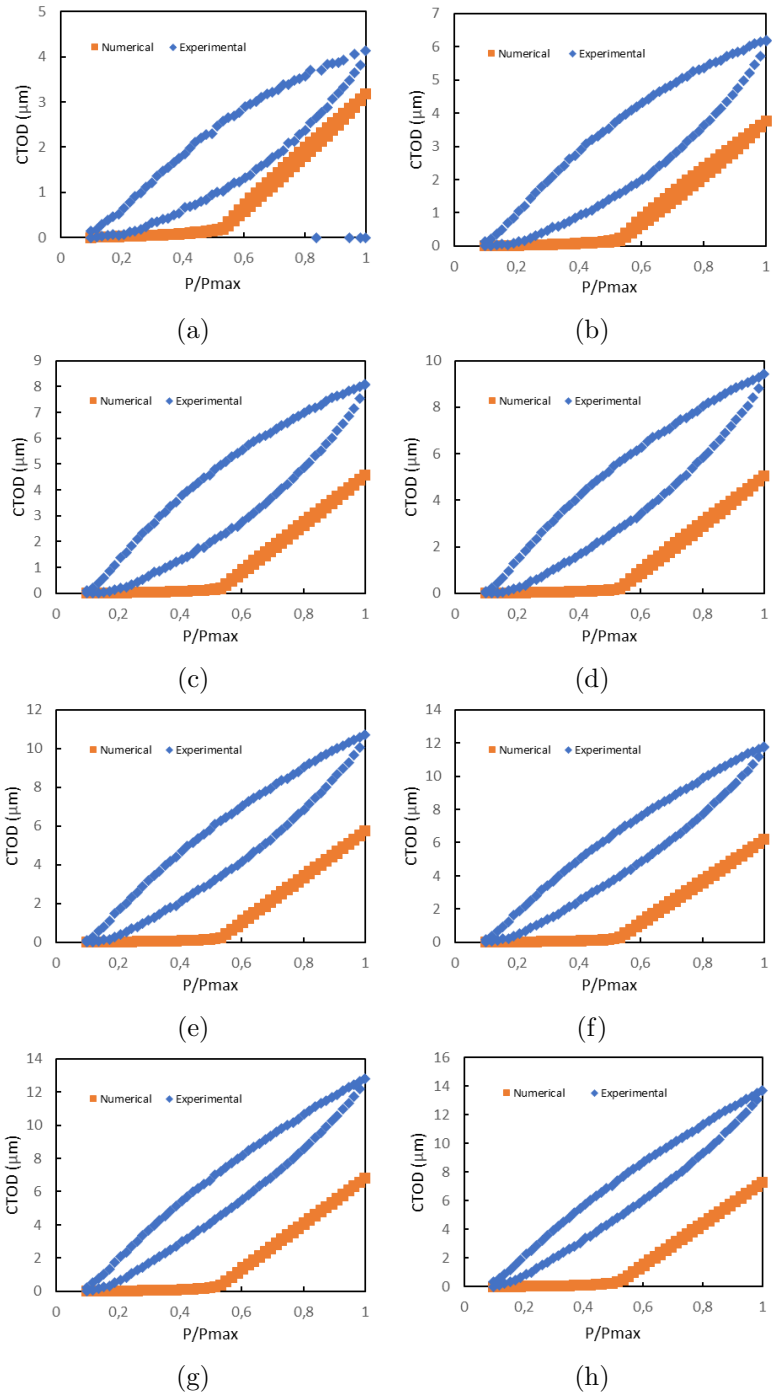

Figure C.4: CTOD vs force for eight load/unload cycles per propagation for 2D plane strain model: (a) 0.024 mm behind the CTL; (b) 0.048 mm behind the CTL; (c) 0.072 mm behind the CTL; (d) 0.096 mm behind the CTL; (e) 0.120 mm behind the CTL; (f) 0.144 mm behind the CTL; (g) 0.168 mm behind the CTL; (h) 0.192 mm behind the CTL.

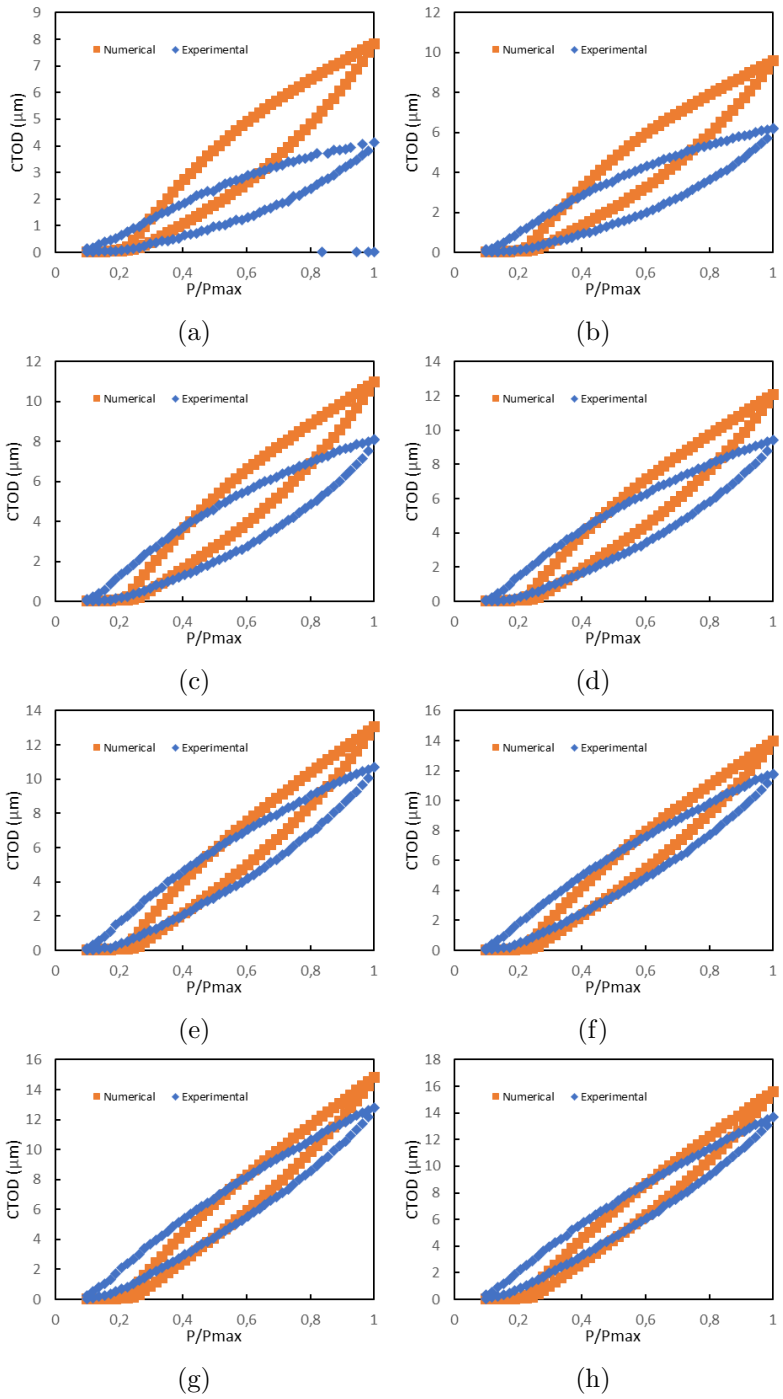

Figure C.5: CTOD vs force for two load/unload cycles per propagation for 0.6 mm model: (a) 0.024 mm behind the CTL; (b) 0.048 mm behind the CTL; (c) 0.072 mm behind the CTL; (d) 0.096 mm behind the CTL; (e) 0.120 mm behind the CTL; (f) 0.144 mm behind the CTL; (g) 0.168 mm behind the CTL; (h) 0.192 mm behind the CTL.

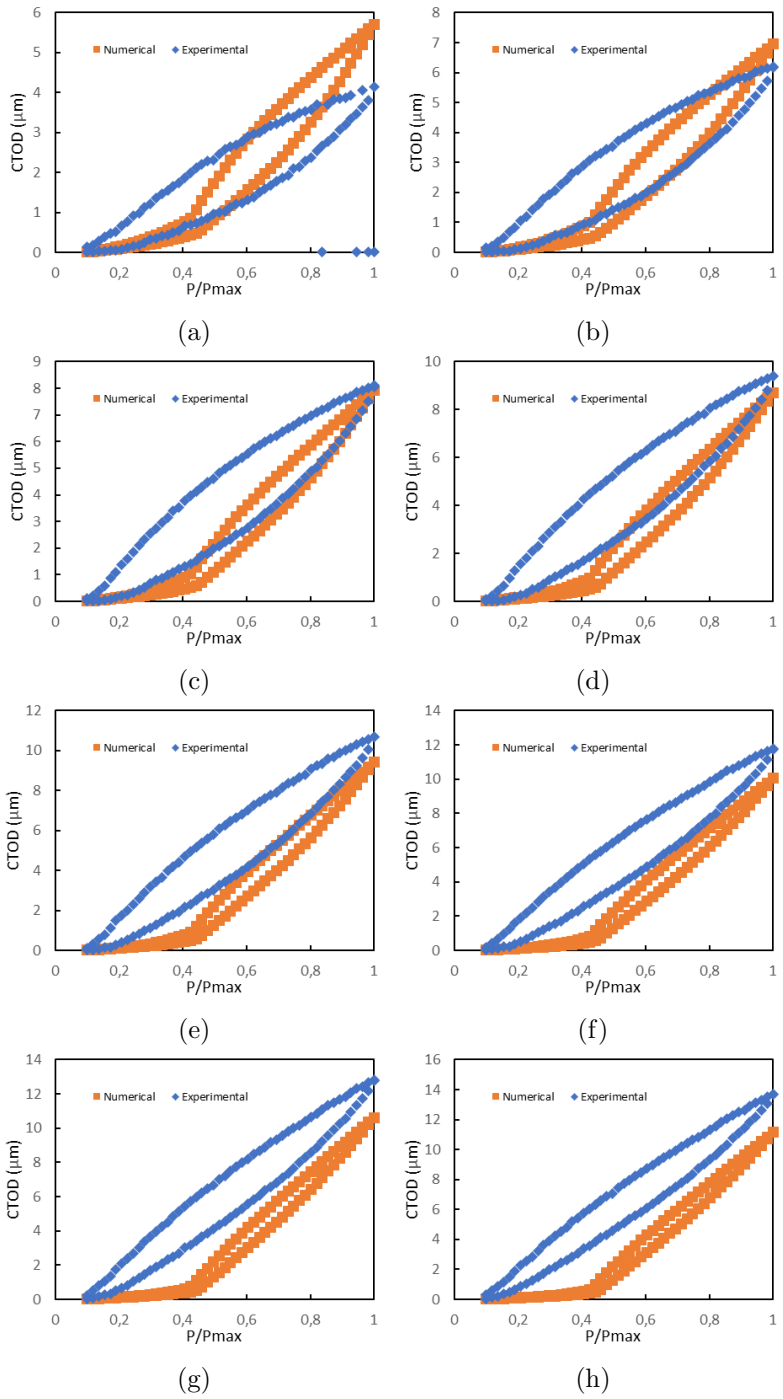

Figure C.6: CTOD vs force for eight load/unload cycles per propagation for 0.6 mm model: (a) 0.024 mm behind the CTL; (b) 0.048 mm behind the CTL; (c) 0.072 mm behind the CTL; (d) 0.096 mm behind the CTL; (e) 0.120 mm behind the CTL; (f) 0.144 mm behind the CTL; (g) 0.168 mm behind the CTL; (h) 0.192 mm behind the CTL.

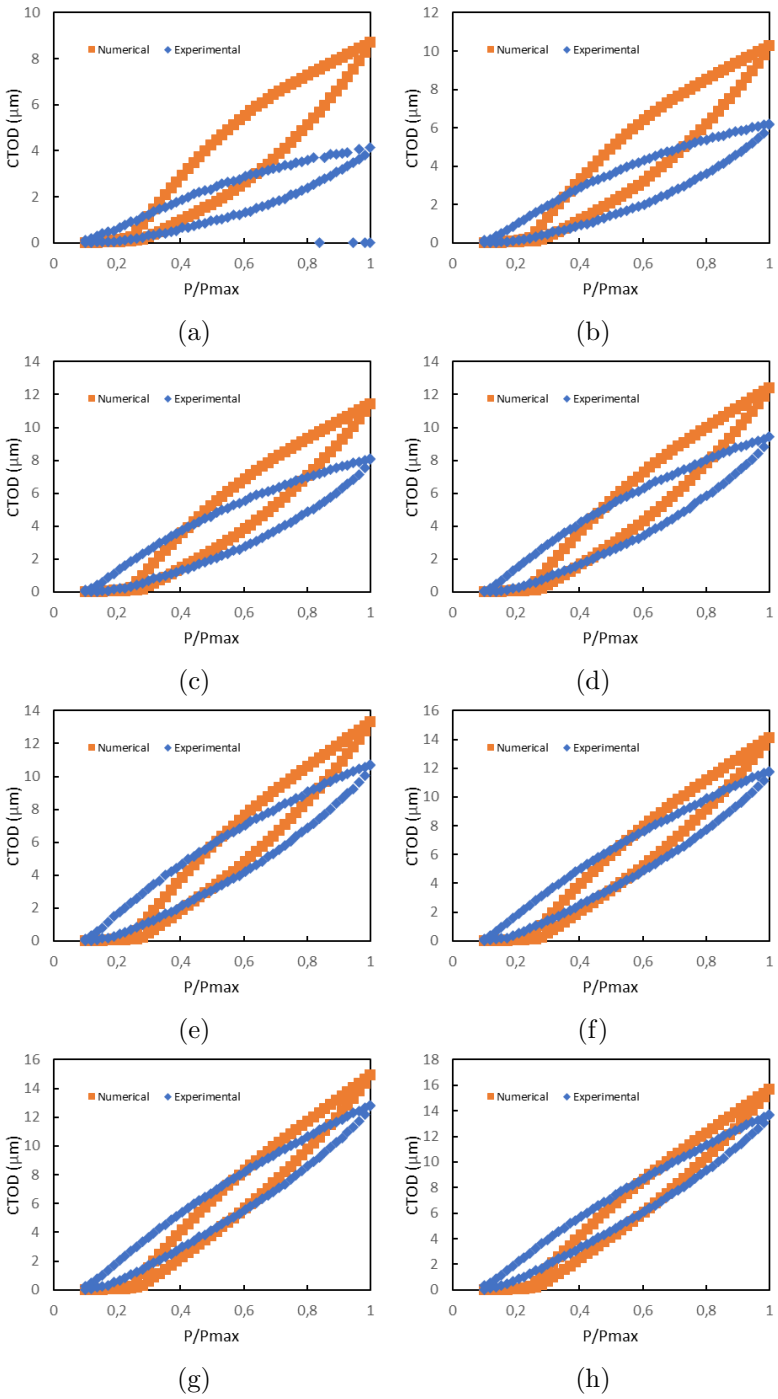

Figure C.7: CTOD vs force for two load/unload cycles per propagation for 0.2 mm model: (a) 0.024 mm behind the CTL; (b) 0.048 mm behind the CTL; (c) 0.072 mm behind the CTL; (d) 0.096 mm behind the CTL; (e) 0.120 mm behind the CTL; (f) 0.144 mm behind the CTL; (g) 0.168 mm behind the CTL; (h) 0.192 mm behind the CTL.

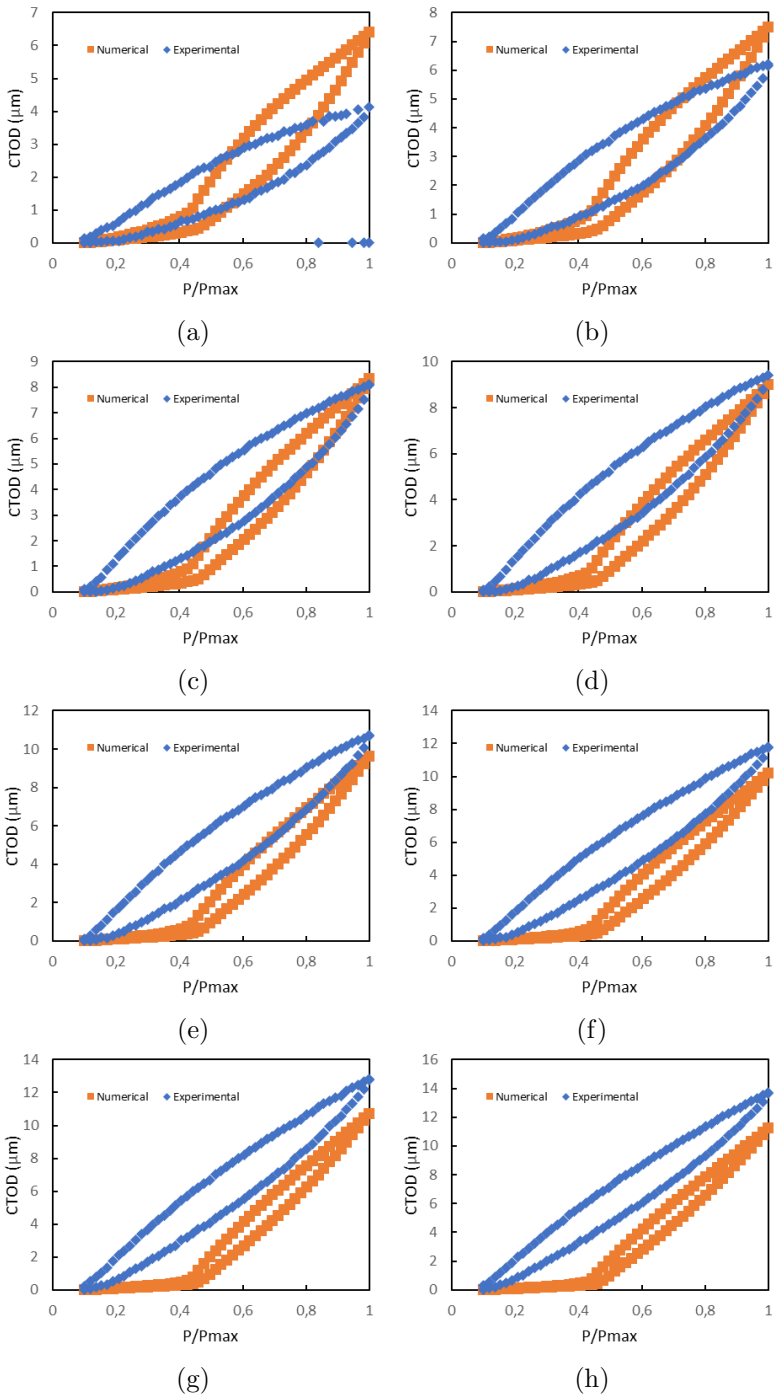

Figure C.8: CTOD vs force for eight load/unload cycles per propagation for 0.2 mm model: (a) 0.024 mm behind the CTL; (b) 0.048 mm behind the CTL; (c) 0.072 mm behind the CTL; (d) 0.096 mm behind the CTL; (e) 0.120 mm behind the CTL; (f) 0.144 mm behind the CTL; (g) 0.168 mm behind the CTL; (h) 0.192 mm behind the CTL.

Intentionally blank page.

References

[1] C. M. Branco, J. M. Ferreira, J. D. Costa, and A. S. Ribeiro, *Projecto de Órgãos de Máquinas*. 3ª ed. - Lisboa: Fundação Calouste Gulbenkian, 2012.

[2] H. F. Hardrath, "Fatigue and fracture mechanics," *AIAA paper*, no. 70–512, 1970.

[3] ASTM E647-11, "Standard Test Method for Measurement of Fatigue Crack Growth Rates," ASTM International, West Conshohocken, PA, Tech. Rep., 2011.

[4] M. F. Borges, "Effect of elasto-plastic properties on fatigue crack growth," Master's thesis, Universidade de Coimbra, 2019.

[5] L. F. R. Paiva, "Propagação de fendas por fadiga: efeito de subcargas," Master's thesis, Universidade de Coimbra, 2015.

[6] G. R. Irwin, "Elasticity and plasticity," in *Elasticity and Plasticity*. Berlin, Heidelberg: Springer, 1958, vol. 3, no. 6, pp. 551–590.

[7] J. Rice, "Mechanics of crack tip deformation and extension by fatigue," *Mechanics of Crack Tip Deformation and Extension by Fatigue*, vol. 415, pp. 247–309, January 1967.

[8] D. C. Peña, "Numerical study of the three-dimensional behaviour of plasticity induced crack closure phenomenon in bi-dimensional specimens," Ph.D. dissertation, Universidad de Málaga, 2013.

[9] T. Anderson, *FRACTURE MECHANICS - Fundamentals and Applications*. 3rd ed. Boca Raton: CRC-Taylor Francis, 2005.

[10] M. Ferreira, "Análise da propagação de fendas por fadiga baseada no CTOD para o aço inoxidável 304L," Master's thesis, Universidade de Coimbra, 2017.

[11] S. Beden, S. Abdullah, and A. Ariffin, "Review of fatigue crack propagation models for metallic components," *European Journal of Scientific Research*, vol. 28, no. 3, pp. 364–397, 2009.

[12] T. Santos, "Estudo numérico da propagação de fendas de fadiga num aço de alta resistência," Master's thesis, Instituto Superior Técnico de Lisboa, 2017.

[13] F. Antunes, S. Serrano, R. Branco, and P. Prates, "Fatigue crack growth in the 2050-T8 aluminium alloy," *International journal of fatigue*, vol. 115, pp. 79–88, 2018.

[14] S. Hajli, "Propagação de fendas por fadiga em bimateriais," Master's thesis, Universidade de Coimbra, 2022.

[15] W. Elber, "Fatigue crack closure under cyclic tension," *Engineering Fracture Mechanics*, vol. 2, no. 1, pp. 37–45, 1970.

[16] L. Correia, "Previsão da vida de propagação à fadiga," Ph.D. dissertation, Universidade de Coimbra, 2018.

[17] S. Suresh and R. Ritchie, "Propagation of short fatigue cracks," *International Metallurgical Reviews*, vol. 29, no. 1, pp. 445–476, 1984.

[18] B. Budiansky and J. Hutchinson, "Analysis of closure in fatigue crack growth," *Journal of Applied Mechanics*, vol. 45, pp. 267–276, 1978.

[19] L. Zhao, J. Tong, and J. Byrne, "The evolution of the stress–strain fields near a fatigue crack tip and plasticity-induced crack closure revisited," *Fatigue & Fracture of Engineering Materials & Structures*, vol. 27, no. 1, pp. 19–29, 2004.

[20] M. Lugo and S. Daniewicz, "The influence of T-stress on plasticity induced crack closure under plane strain conditions," *International journal of fatigue*, vol. 33, no. 2, pp. 176–185, 2011.

[21] S. K. Paul and S. Tarafder, "Cyclic plastic deformation response at fatigue crack tips," *International Journal of Pressure Vessels and Piping*, vol. 101, pp. 81–90, 2013.

[22] T. Sousa, "Propagação de fendas por fadiga: Influência do contacto nos parâmetros de extremidade de fenda," Master's thesis, Universidade de Coimbra, 2014.

[23] A. Wells, "Unstable crack propagation in metals: cleavage and fast fracture," in *Proceedings of the crack propagation symposium*, vol. 1, no. 84, 1961, p. 210–230.

[24] J. R. Rice, "A path independent integral and the approximate analysis of strain concentration by notches and cracks," *Journal of Applied Mechanics*, vol. 35, p. 379–386, 1968.

[25] M. A. Sutton, S. R. McNeill, J. D. Helm, and M. L. Boone, "Measurement of crack tip opening displacement and full-field deformations during fracture of aerospace materials using 2d and 3d image correlation methods," in *IUTAM Symposium on Advanced Optical Methods and Applications in Solid Mechanics*. Springer, 2002, pp. 571–580.

[26] D. Nowell and P. De Matos, "Application of digital image correlation to the investigation of crack closure following overloads," *Procedia Engineering*, vol. 2, no. 1, pp. 1035–1043, 2010.

[27] F. Yusof, P. Lopez-Crespo, and P. Withers, "Effect of overload on crack closure in thick and thin specimens via digital image correlation," *International Journal of Fatigue*, vol. 56, pp. 17–24, 2013.

[28] P. Lopez-Crespo, A. Shterenlikht, J. Yates, E. Patterson, and P. Withers, "Some experimental observations on crack closure and crack-tip plasticity," *Fatigue & Fracture of Engineering Materials & Structures*, vol. 32, no. 5, pp. 418–429, 2009.

[29] A. Shterenlikht, F. Diaz Garrido, P. Lopez-Crespo, P. J. Withers, and E. Patterson, "Mixed mode (KI+ KII) stress intensity factor measurement by electronic speckle pattern interferometry and image correlation," *Applied Mechanics and Materials*, vol. 1, pp. 107–112, 2004.

[30] P. Lopez-Crespo, A. Shterenlikht, E. Patterson, J. Yates, and P. Withers, "The stress intensity of mixed mode cracks determined by digital image correlation," *The Journal of Strain Analysis for Engineering Design*, vol. 43, no. 8, pp. 769–780, 2008.

[31] P. Lopez-Crespo, R. Burguete, E. Patterson, A. Shterenlikht, P. Withers, and J. Yates, "Study of a crack at a fastener hole by digital image correlation," *Experimental Mechanics*, vol. 49, pp. 551–559, 2009.

[32] M. D. Cruz, "Efeito das propriedades elasto-plásticas na propagação de fendas por fadiga," Master's thesis, Universidade de Coimbra, 2018.

[33] S. Serrano, "Análise da propagação de fendas por fadiga baseada no CTOD para a liga 2050-T8 AA," Master's thesis, Universidade de Coimbra, 2017.

[34] S. Rodrigues, "Propagação de fendas por fadiga: Estudo numérico de CTOD," Master's thesis, Universidade de Coimbra, 2016.

[35] R. Simões, "Análise da propagação de fendas por fadiga com base no CTOD: efeito dos parâmetros numéricos," Master's thesis, Universidade de Coimbra, 2017.

[36] M. F. Borges, P. Lopez-Crespo, F. V. Antunes, B. Moreno, P. Prates, D. Camas, and D. M. Neto, "Fatigue crack propagation analysis in 2024-T351 aluminium alloy using nonlinear parameters," *International Journal of Fatigue*, 2021.

[37] T. Oplt, T. Vojtek, R. Kubíček, P. Pokornỳ, and P. Hutař, "Numerical modelling of fatigue crack closure and its implication on crack front curvature using ΔCTODp," *International Journal of Fatigue*, 2023.

[38] M. Escalero, M. Muniz-Calvente, H. Zabala, and I. Urresti, "Crack shapes and crack driving force distributions for naturally growing fatigue cracks," *Engineering Fracture Mechanics*, 2023.

[39] M. Escalero, M. Muniz-Calvente, H. Zabala, I. Urresti, R. Branco, and F. Antunes, "A methodology for simulating plasticity induced crack closure and crack shape evolution based on elastic–plastic fracture parameters," *Engineering Fracture Mechanics*, 2021.

[40] F. Antunes, S. Rodrigues, R. Branco, and D. Camas, "A numerical analysis of CTOD in constant amplitude fatigue crack growth," *Theoretical and Applied Fracture Mechanics*, vol. 85, pp. 45–55, 2016.

[41] R. Branco, D. Rodrigues, and F. Antunes, "Influence of through-thickness crack shape on plasticity induced crack closure," *Fatigue & Fracture of Engineering Materials & Structures*, vol. 31, no. 2, pp. 209–220, 2008.

[42] D. Camas, J. Garcia-Manrique, B. Moreno, and A. Gonzalez-Herrera, "Numerical modelling of three-dimensional fatigue crack closure: mesh refinement," *International Journal of Fatigue*, vol. 113, pp. 193–203, 2018.

[43] C. Gardin, S. Fiordalisi, C. Sarrazin-Baudoux, and J. Petit, "Numerical simulation of fatigue plasticity-induced crack closure for through cracks with curved fronts," *Engineering Fracture Mechanics*, vol. 160, pp. 213–225, 2016.

[44] C. Gardin, S. Fiordalisi, C. Sarrazin-Baudoux, M. Gueguen, and J. Petit, "Numerical prediction of crack front shape during fatigue propagation considering plasticity-induced crack closure," *International Journal of Fatigue*, vol. 88, pp. 68–77, 2016.

[45] C.-Y. Hou, "Plasticity-induced crack closure from surface to deep interior locations–a three-dimensional finite element study," *Engineering Fracture Mechanics*, vol. 195, pp. 186–199, 2018.

[46] F. F. Ferreira, D. M. Neto, J. S. Jesus, P. A. Prates, and F. V. Antunes, "Numerical prediction of the fatigue crack growth rate in SLM Ti-6Al-4V based on crack tip plastic strain," *Metals*, vol. 10, 2020.

[47] M. Borges, D. Neto, and F. Antunes, "Numerical simulation of fatigue crack growth based on accumulated plastic strain," *Theoretical and Applied Fracture Mechanics*, vol. 108, 2020.

[48] K. K. Gupta and J. Meek, *Finite element multidisciplinary analysis*. AIAA Education Series, 2003.

[49] R. Cláudio, R. Baptista, V. Infante, and C. Branco, "Life prediction using finite elements in complex geometries," in *Eighth Portuguese Conference on Fracture*. Citeseer, 2002.

[50] F. Teixeira-Dias, J. P. da Cruz, R. Valente, and R. Alves de Sousa, *Método dos Elementos Finitos: Técnicas de Simulação Numérica em Engenharia*. ETEP - Technical and Professional Editions, 2010.

[51] Á. F. Azevedo, "Método dos elementos finitos," *Faculdade de Engenharia da Universidade do Porto*, vol. 1, no. 7, 2003.

[52] SIMULIA. (2014) Abaqus theory guide. [Online]. Available: http://130.149.89.49:2080/v6.14/books/stm/default.htm?startat=ch03s02ath63.html

[53] "Abaqus/standard user's manual, version 6.5," *Hibbitt, Karlsson & Sorensen, Inc*, 2001.

[54] J. Silva, "Análise da Propagação de Fendas por Fadiga-Fluência na Superliga de Níquel RR1000," Ph.D. dissertation, Instituto Superior Técnico – Universidade Técnica de Lisboa, 2007.

[55] C. Monteiro, "Determinação do factor de intensidade de tensões em fendas na vizinhança de entalhes," Master's thesis, Instituto Superior Técnico – Universidade Técnica de Lisboa, 2007.

[56] A. KumarH. (2022) What is strain hardening and plasticity? [Online]. Available: https://skill-lync.com/blogs/technical-blogs/mechanical-what-is-strain-hardening-and-plasticity

[57] T. Grilo, "Estudo de modelos constitutivos anisotrópicos para chapas metálicas," Master's thesis, Universidade de Aveiro, 2011.

[58] J. Chakrabarty, *Applied plasticity.* 2nd ed., 2010.

[59] P. Prates, "Inverse methodologies for identifying constitutive parameters of metal sheets," Ph.D. dissertation, Universidade de Coimbra, 2014.

[60] F. K. G. Odquist, "Math. mech," vol. 13, p. 360, 1933.

[61] R. Hill, *The Mathematical Theory of Plasticity.* Oxford university press, 1950.

[62] E. Voce, "The relationship between stress and strain for homogeneous deformation," *Journal of the Institute of Metals*, vol. 74, pp. 537–562, 1948.

[63] H. Swift, "Plastic instability under plane stress," *Journal of the Mechanics and Physics of Solids*, vol. 1, no. 1, pp. 1–18, 1952.

[64] T. Neves, "Simulação numérica do retorno elástico de um componente automóvel," Master's thesis, Universidade de Coimbra, 2016.

[65] C. O. Frederick and P. Armstrong, "A mathematical representation of the multiaxial bauschinger effect," *Materials at High Temperatures*, vol. 24, no. 1, pp. 1–26, 2007.

[66] G. International. (2016) 2024 aluminum: Get to know its properties and uses. [Online]. Available: https://www.gabrian.com/2024-aluminum-properties/

[67] C. Materials. (2023) Titanium grade 2. [Online]. Available: https://corrosionmaterials.com/alloys/titanium-grade-2/

[68] T. Gateway. (2022) What is titanium grade 2? [Online]. Available: https://titanium-gateway.com/vanliga-fragor/fraga-2/

[69] A. W. METALS. (2000) Product data sheet – titanium alloys. [Online]. Available: https://www.australwright.com.au/technical-data/alloys/high-performance-alloys/titanium-alloy-grade-2/

[70] L. S. Lasdon, A. D. Waren, A. Jain, and M. W. Ratner, "Design and testing of a generalized reduced gradient code for nonlinear optimization," *Case Western Reserve University, National Technical Information Service US Department of Commerce (NTIS)*, 1975.

[71] G. G. Gonzáles, F. Antunes, E. Sérgio, J. Vasco-Olmo, F. Díaz, and D. Neto, "A comparison between FEM predictions and DIC results of crack tip displacement field in CT specimens made of titanium," *Theoretical and Applied Fracture Mechanics*, vol. 127, p. 104055, 2023.

[72] B. Marques, D. Neto, F. Antunes, J. Vasco-Olmo, and F. Diaz, "Numerical tool for the analysis of CTOD curves obtained by DIC or FEM," *Fatigue & Fracture of Engineering Materials & Structures*, vol. 43, no. 12, pp. 2984–2997, 2020.